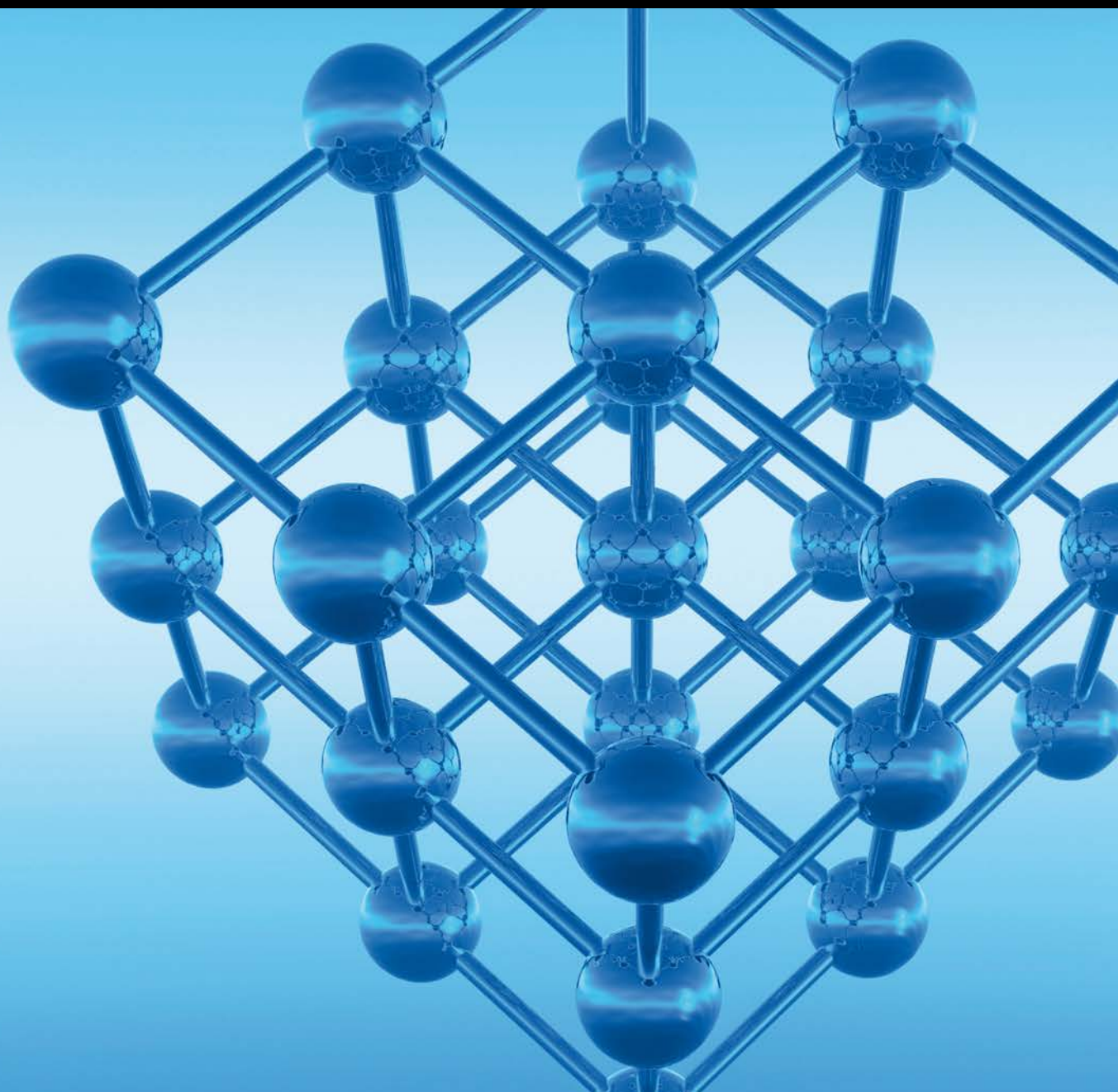


Advances in Condensed Matter Physics

Two-Dimensional Materials Based Optoelectronics

Lead Guest Editor: Yu Chen

Guest Editors: Jun Liu, Jizhou Jiang, Xiaofeng Zhou, Shuqing Chen,
and Yan Luo





Two-Dimensional Materials Based Optoelectronics

Advances in Condensed Matter Physics

Two-Dimensional Materials Based Optoelectronics

Lead Guest Editor: Yu Chen

Guest Editors: Jun Liu, Jizhou Jiang, Xiaofeng Zhou,
Shuqing Chen, and Yan Luo



Copyright © 2017 Hindawi. All rights reserved.

This is a special issue published in “Advances in Condensed Matter Physics.” All articles are open access articles distributed under the Creative Commons Attribution License, which permits unrestricted use, distribution, and reproduction in any medium, provided the original work is properly cited.

Editorial Board

Bohdan Andraka, USA
Ward Beyermann, USA
Golam M. Bhuiyan, Bangladesh
Luis L. Bonilla, Spain
Ashok Chatterjee, India
Ram N. P. Choudhary, India
Oleg Derzhko, Ukraine
Gayanath Fernando, USA

Jörg Fink, Germany
Yuri Galperin, Norway
Prasenjit Guptasarma, USA
Da-Ren Hang, Taiwan
Jan A. Jung, Canada
Joseph S. Poon, USA
Leonid Pryadko, USA
Charles Rosenblatt, USA

Mohindar S. Seehra, USA
Sergei Sergeenkov, Brazil
Sergio E. Ulloa, USA
Markus R. Wagner, Germany
Gary Wysin, USA
Kiyokazu Yasuda, Japan
Fajun Zhang, Germany
Jiandi Zhang, USA

Contents

Two-Dimensional Materials Based Optoelectronics

Yu Chen, Jun Liu, Jizhou Jiang, Xiaofeng Zhou, Shuqing Chen, and Yan Luo
Volume 2017, Article ID 5789823, 2 pages

Enhanced Group Delay of the Pulse Reflection with Graphene Surface Plasmon via Modified Otto Configuration

Guimei Li, Qiwei Liu, Yue Liu, Yueying Wei, Rui Weng,
Yuxiang Zhou, and Leyong Jiang
Volume 2017, Article ID 1569621, 8 pages

Tunable Optical Bistability in One-Dimensional Photonic Crystal with a Nonlinear Defect Coupled by Graphene Sheets

Zhiwei Zheng, Leyong Jiang, Jun Guo, Xiaoyu Dai, and Yuanjiang Xiang
Volume 2017, Article ID 6590424, 6 pages

Effective Generation of Milliwatt-Level Sub-Terahertz Wave for Nonlinear Response Measurement of Two-Dimensional Material by Optical Heterodyne Technique

Shuqing Chen, Zhiqiang Xie, Junmin Liu, Yanliang He, Yao Cai, Xiaoke Zhang, Jiangnan Xiao, Ying Li, and Dianyuan Fan
Volume 2017, Article ID 1704374, 9 pages

Over 19 W Single-Mode 1545 nm Er,Yb Codoped All-Fiber Laser

Jiadong Wu, Chunxiang Zhang, Jun Liu, Ting Zhao, Weichao Yao, Pinghua Tang, Le Zhang, and Hao Chen
Volume 2017, Article ID 7408565, 5 pages

Submicrosecond Q-Switching Er-Doped All-Fiber Ring Laser Based on Black Phosphorus

Yao Cai, Yanliang He, Xiaoke Zhang, Rui Jiang, Chenliang Su, and Ying Li
Volume 2017, Article ID 1703596, 4 pages

Self-Reconstruction Property of a Special Speckle Pattern after Obstructing by an Opaque Obstruction

Yanyu Chen, Huang Tan, and Gaofeng Wu
Volume 2017, Article ID 9625206, 8 pages

Dynamics of Dispersive Wave Generation in Gas-Filled Photonic Crystal Fiber with the Normal Dispersion

Zhixiang Deng and Meng Zhang
Volume 2017, Article ID 1268230, 9 pages

Optical Orbital Angular Momentum Demultiplexing and Channel Equalization by Using Equalizing Dammann Vortex Grating

Mingyang Su, Junmin Liu, Yanliang He, Shuqing Chen, and Ying Li
Volume 2017, Article ID 6293910, 9 pages

Editorial

Two-Dimensional Materials Based Optoelectronics

Yu Chen,¹ Jun Liu,² Jizhou Jiang,³ Xiaofeng Zhou,⁴ Shuqing Chen,¹ and Yan Luo⁵

¹*International Collaborative Laboratory of 2D Materials for Optoelectronics Science and Technology, Key Laboratory of Optoelectronic Devices and Systems of Ministry of Education and Guangdong Province, College of Optoelectronic Engineering, Shenzhen University, Shenzhen 518060, China*

²*Aston Institute of Photonic Technologies, School of Engineering and Applied Science, Aston University, Birmingham B4 7ET, UK*

³*Department of Physics, National University of Singapore, 2 Science Drive 3, Singapore 117542*

⁴*Physical Sciences and Engineering Division, King Abdullah University of Science and Technology, Thuwal 23955-6900, Saudi Arabia*

⁵*Department of Chemical Engineering, West Virginia University, 313 Engineering Research Building, Evansdale Drive, Morgantown, WV 26506, USA*

Correspondence should be addressed to Yu Chen; yuchen@szu.edu.cn

Received 24 September 2017; Accepted 25 September 2017; Published 28 November 2017

Copyright © 2017 Yu Chen et al. This is an open access article distributed under the Creative Commons Attribution License, which permits unrestricted use, distribution, and reproduction in any medium, provided the original work is properly cited.

Recently, originating from the emerging and intensive research of graphene, there have been tremendous improvements in the area of two-dimensional (2D) materials (e.g., graphene, topological insulators, and black phosphorus) based optoelectronics. Their unique and novel characteristics strongly promoted the developments of condensed-matter physics, device physics, photonics, electronics, optoelectronics, and so on. The purpose of this feature issue is to present the state of recent progresses in the field, from fundamental physics (condensed-matter physics, device physics, and so on) to various applications of the emerging 2D materials. The feature issue covers various aspects of theoretical and experimental researches related to 2D materials based optoelectronics. Among plenty of submissions, we selected 8 papers for publication in the special issue.

The paper posted by S. Chen et al. demonstrates a home-made nonlinear response measurement system of 2D materials in sub-terahertz waveband. Using mutual frequency beating technology, they achieve the radiation of 0.1 THz wave with power up to 4 mW. Based on this sub-terahertz source, they measure the nonlinear response of topological insulator. The paper by G. Li et al. studies the optical group delay in a modified Otto configuration with graphene surface plasmon. The optical group delay can be tuned obviously, even from negative to positive, with variety of means (Fermi energy, relaxation time of graphene, distance between the coupling prism, and graphene). The paper by Z. Zeng et al. investigates

the bistability in one-dimensional photonic crystal (1DPC) covered by graphene. By tuning the Fermi energy and the number of graphene monolayers, the hysteresis and nonlinear lateral shift in 1DPCs can be controlled effectively.

The paper by Y. Cai proposes a submicrosecond passively Q-switching Er-doped fiber laser with black phosphorus (BP) as saturable absorber (SA). By taking full advantage of the ultra-fast relaxation time of BP SA and careful design of compact ring cavity, they obtain stable Q-switching pulses output with record duration of 742 ns experimentally. It indicates that BP-SA can be an effective SA for nanosecond Q-switching pulse generation. The paper by J. Wu et al. reports a high-power cladding-pumped Er,Yb codoped all-fiber laser with truly single transverse mode output. By using a pair of fiber Bragg gratings (FBGs), two pieces of standard single-mode fibers, and other careful cavity designs, they obtain a record high of output power with single-mode in an all-fiber single-mode Er,Yb codoped laser. The work by Z. Deng et al. investigates the generation of dispersive wave (DW) in normal group-velocity dispersion (GVD) region with photonic crystal fiber (PCF). Through controlling DW generation in gas-filled PCF with combined effects of self-steepening (SS) and chirp, one can achieve any wavelength artificially with controllable energy.

The paper by M. Su et al. proposes a novel equalizing Dammann vortex grating (EDVG) to realize orbital angular momentum (OAM) signal demultiplexing and channel

equalization. By suppressing odd diffraction orders and adjusting grating structure, the total diffraction efficiency of EDVG can be highly improved. Therefore, the bit error rate (BER) of each OAM channel can be decreased sharply.

The paper by Y. Chen et al. demonstrates random optical field with special autocorrelation which is different from the general autocorrelation with a Gaussian function. The speckle with special autocorrelation has self-healing effect. The self-healing process is affected by the size of obstruction and the coherence of the speckle but is almost not affected by the shape of obstruction.

Yu Chen
Jun Liu
Jizhou Jiang
Xiaofeng Zhou
Shuqing Chen
Yan Luo

Research Article

Enhanced Group Delay of the Pulse Reflection with Graphene Surface Plasmon via Modified Otto Configuration

Guimei Li,¹ Qiwei Liu,² Yue Liu,² Yueying Wei,² Rui Weng,²
Yuxiang Zhou,² and Leyong Jiang²

¹*School of Computer and Information Engineering, Hunan University of Commerce, Changsha 410205, China*

²*College of Physics and Information Science, Hunan Normal University, Changsha 410081, China*

Correspondence should be addressed to Leyong Jiang; jiangly28@hunnu.edu.cn

Received 28 June 2017; Accepted 30 August 2017; Published 1 November 2017

Academic Editor: Yan Luo

Copyright © 2017 Guimei Li et al. This is an open access article distributed under the Creative Commons Attribution License, which permits unrestricted use, distribution, and reproduction in any medium, provided the original work is properly cited.

In this paper, the group delay of the transverse magnetic (TM) polarized wave reflected from a modified Otto configuration with graphene surface plasmon is investigated theoretically. The findings show that the optical group delay in this structure can be enhanced negatively and can be switched from negative to positive due to the excitation of surface plasmon by graphene. It is clear that the negative group delay can be actively tuned through the Fermi energy of the graphene. Furthermore, the delay properties can also be manipulated by changing either the relaxation time of graphene or the distance between the coupling prism and the graphene. These tunable delay characteristics are promising for fabricating graphene-based optical delay devices and other applications in the terahertz regime.

1. Introduction

The group delay properties of optical pulse traversing through a system together with delay control techniques have received extensive research interests due to their importance in optical communication [1, 2]. The pulse delay control techniques enable unique micro/nanodevices with novel functionalities. The potential applications of the above group delay properties include controllable all-optical delays [3], arbitrary-angle beamforming [4], and all-optical buffers [5]. Various techniques and approaches have been explored to accomplish the tunable and large group delay in order to achieve the extraordinary phenomena described as “subluminal effect” and “superluminal effect” in various frequency ranges, like electromagnetically induced transparency (EIT) systems [6], weakly absorbing dielectric [7], Fabry-Perot cavity configuration [8], metamaterial slab [9], and so on. Compared with the subluminality, the superluminality characterized by negative group delay continues to attract much attention due to the counterintuitive phenomenon and the possible applications. For example, Manipatruni et al. realized superluminal propagation on a silicon microchip by using

coherent interaction between the microcavities [10]; Choi et al. reported an enhancement of feedforward amplifiers by adopting superluminal delay circuit [11]. More recently, Yao et al. experimentally demonstrated a negative group delay approach in a circular waveguide system with an asymmetric cross-shaped slotted configuration [12]. However, the demands to develop optical delay approach with large delay time, high tunability, and easy integration for optical communication are ever increasing.

In recent years, graphene, a two-dimensional atomic crystal material, has received a wide range of attention in the field of optoelectronics due to its excellent optical and electrical properties, such as zero-gap characteristic [13], electrical tunability [14, 15], low losses [16, 17], and strong nonlinear response [18], among others. It is worth mentioning that graphene can support the existence of TM polarized and transverse electric (TE) polarized surface plasmon polaritons (SPPs) propagating along graphene, depending on the sign of the imaginary part of graphene conductivity [19]. This feature can significantly enhance the light-matter interaction [20] and further enriches its application in the terahertz (THz) and infrared spectrum [21–23]. It is known that the large

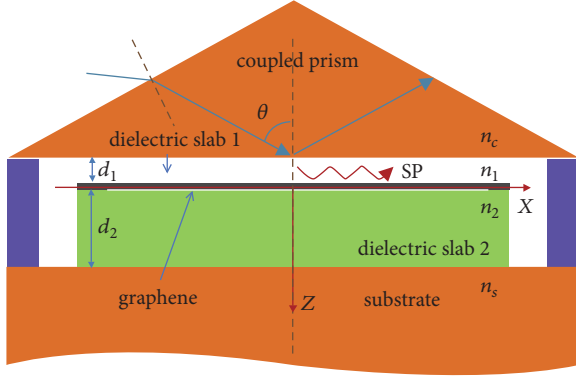


FIGURE 1: Schematic diagram of a modified Otto configuration with the insertion of monolayer graphene. An incident light with an angle θ to the surface normal is considered.

group delay is usually found near a resonance of the structure. Hence, the combination of graphene and surface plasmon obviously seems to be an alternative candidate for realizing and manipulating tunable group delay devices.

In this paper, it is proposed and theoretically demonstrated that there is a possibility of realizing and manipulating large reflected group delay of optical pulse from a modified Otto configuration with the graphene surface plasmon in THz regime. This large reflected group delay originates from the local abrupt phase change at the interface of two dielectrics with monolayer graphene owing to the excitation of the surface plasmon. In particular, since the optical conductivity of graphene can be dynamically manipulated by varying the Fermi energy, the corresponding subluminal and superluminal effects can be continuously tuned in a frequency regime. The pathway proposed in this paper is designed to manipulate the reflected group delay of THz pulses, which would inspire the potential for a variety of applications [24–26], particularly for sensing technologies and THz delay devices.

2. Theoretical Model and Method

In this section, an attenuated total reflection scheme for exciting SPPs is under consideration using modified Otto configuration [27], in which a dielectric layer refractive index with thickness d_2 is placed on a substrate. Dielectric slab 2 is covered by monolayer graphene. Between dielectric slab 2 and the coupled prism there is the dielectric slab 1 with a thickness of d_1 as shown in Figure 1, where z direction is the incidence direction, while x direction is parallel to the plane of the monolayer graphene. n_1 and n_2 are the refractive index of dielectric slab 1 and the refractive index of dielectric slab 2, respectively. n_c and n_s are the refractive index of coupled prism and the refractive index of substrate. Here, to facilitate the excitation of SPPs, dielectric slab 1 is assumed to be an air layer with low refractive index and small thickness. In the following calculations, the center frequency is 5 THz, temperature $T = 300$ K, and relaxation time $\tau = 1$ ps. Besides, in order to inhibit the absorption of incident electromagnetic waves caused by the excitation of SPPs, the thicknesses of

dielectric slab 1 and dielectric slab 2 in the configuration are set as $2 \mu\text{m}$ and $8 \mu\text{m}$, respectively. Meanwhile, to facilitate the excitation of SPPs, dielectric slabs 1 and 2 are assumed to be low refractive air and polymethylpentene material, whose respective indexes are $n_1 = 1$ and $n_2 = 1.46$, respectively. In addition, high refractive materials in THz spectrum are used for the coupling prism and substrate. More specifically, germanium materials (refractive index $n_c = n_s = 3.84$) are selected for the prism and substrate in this research. For the sake of simplicity, the dielectric loss is not taken into consideration, which means the imaginary part of refractive index is assumed to be zero. The optical properties of the monolayer graphene can be represented by optical conductivity. Under random phase approximation, the surface conductivity of graphene can be regarded as the sum of interconductivity and intraconductivity [28]. However, the surface conductivity of graphene in the terahertz frequencies is dominated by the intraconductivity. At this moment, the graphene conductivity can be approximately expressed as

$$\sigma = \frac{ie^2k_B T}{\pi\hbar^2(\omega + i/\tau)} \left(\frac{E_F}{k_B T} + 2 \ln(e^{-E_F/k_B T} + 1) \right), \quad (1)$$

where e , k_B , T , and \hbar represent the electron charge, Boltzmann constant, temperature, and reduced Planck's constant, respectively; ω represents the angular frequency of incident electromagnetic wave; τ and E_F represent the electron-phonon relaxation time and the Fermi energy of graphene, respectively. The above equation shows that the conductivity properties of graphene are closely related to Fermi energy, and the value of Fermi energy can be tuned by external voltage, which provides a means to flexibly tune the optical conductivity of graphene and further tune the optical properties of the whole configuration.

In order to calculate the reflected group delay properties of the configuration, the transmission and reflection properties of the whole configuration are also required. Based on the monoatomic layer characteristic of the graphene, the modified transfer matrix method is adopted in this paper to calculate the transmittance and reflectance of the configuration [29]. In this paper, as graphene is just of monoatomic thickness, its conductivity properties can be reflected in boundary conditions. For this reason, the transmission matrix between the TM polarized dielectric slab 1 and dielectric slab 2 can be expressed as

$$D_{12} = \frac{1}{2} \begin{bmatrix} 1 + \eta_{\text{TM}} + \xi_{\text{TM}} & 1 - \eta_{\text{TM}} - \xi_{\text{TM}} \\ 1 - \eta_{\text{TM}} + \xi_{\text{TM}} & 1 + \eta_{\text{TM}} - \xi_{\text{TM}} \end{bmatrix}. \quad (2)$$

In this equation, $\eta_{\text{TM}} = \varepsilon_1 k_{2z} / \varepsilon_2 k_{1z}$, $\xi_{\text{TM}} = \sigma k_{2z} / \varepsilon_0 \varepsilon_2 \omega$, where k_{1z} and k_{2z} represent the components of wave vectors k_1 and k_2 in the transmission direction of electromagnetic wave; ε_0 , ε_1 , and ε_2 are the vacuum permittivity, dielectric constants of dielectric slab 1, and dielectric constants of dielectric slab 2, respectively. Similarly, the TE polarized transmission matrix is also presented in [29]. However, it is noteworthy that graphene can excite both TE polarized and TM polarized SPPs, which is quite different from metal as the latter can only excite TM polarized SPPs. But the two polarized

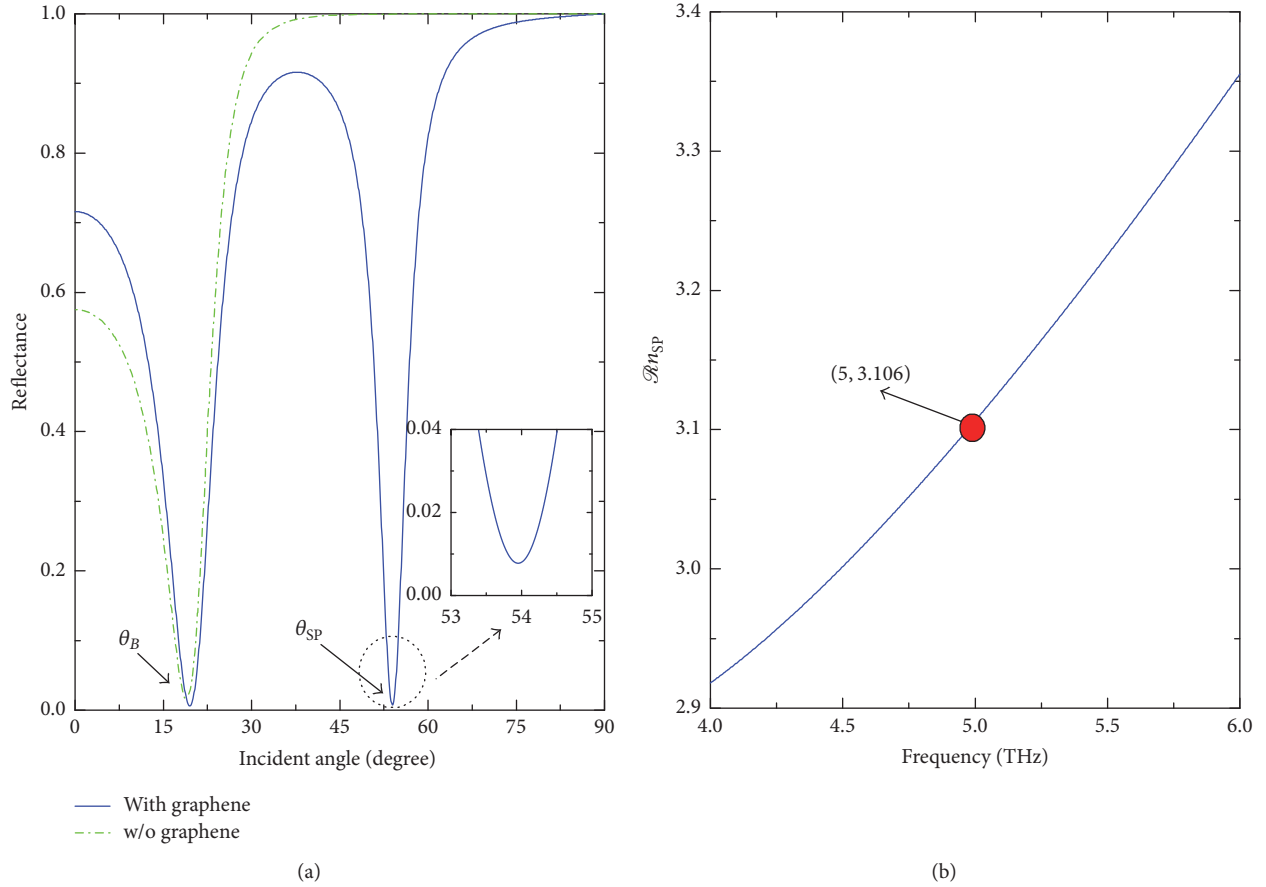


FIGURE 2: (a) Reflectance of the configuration as a function of incident angle θ (solid line). For comparison, the reflectance without monolayer graphene is also shown (dash dot line). (b) SPPs dispersion characteristics on monolayer graphene as a function of frequency.

exciting spectrums should not be in the same spectrum [19], and this research only considers the TM polarized pulse reflected group delay. Based on the transmission matrix and the propagation matrix transmitted in the dielectric layer, the transmission coefficient and reflection coefficient of the whole configuration can be obtained. If the incident pulse is assumed to be Gaussian pulse, the reflected group delay of the whole configuration can be expressed as

$$\tau_r = \left[\frac{\partial \phi_r}{\partial \omega} \right]_{\omega=\omega_c}. \quad (3)$$

Here, ω_c is the carrier frequency, ϕ_r is the phase of the reflection coefficient $r(\omega)$, and $r(\omega) = |r(\omega)| \exp(i\phi_r(\omega))$.

3. Results and Discussions

3.1. Reflectance and Dispersion Relation. In this section, the characteristics of reflected group delay in the configuration will be discussed. In respect to the lossless configuration and dielectric, the zero reflection at the resonances ($\text{Re}(kd) = m\pi (m = 1, 2, 3, \dots)$) would make the reflected delay at the resonances physically meaningless. However, when monolayer graphene is embedded into the contact surface of the dielectric layer with excited SPPs, the reflectance will become

very small but not turn to zero, and the slope of the reflected phase will be changed as well. Consequently, the conditions for realizing large reflected group delay are created. Besides, the tunable optical characteristics give graphene considerable advantages in terms of controllable enhanced pulse delay. In the following calculation, it is assumed that the Fermi energy satisfies $E_F = 1$ eV. First, the reflection characteristics of the whole configuration are illustrated in Figure 2(a). When monolayer graphene is missing, it is impossible to excite SPPs in the configuration. As a result, there is only one reflectance dip at the Brewster angle (θ_B) among the reflectance that changes with the angle. But when the incident angle is larger than Brewster angle, the reflectance of the whole configuration is almost 100% due to total reflection. Meanwhile, as the dielectric losses are neglected, the transmittance is almost zero (not shown in the figure). However, when the graphene is embedded into the configuration and excites SPPs through proper wave vector matching, a second reflectance dip occurs near the 54° larger than the Brewster angle. As shown in Figure 2(a), the dip is narrow and the reflectance approximates to zero. To describe the generation mechanism of the dip, an SPPs dispersion characteristics curve of the configuration is drawn based on boundary conditions, as shown in Figure 2(b). According to this curve, in the configuration proposed in this paper, the effective

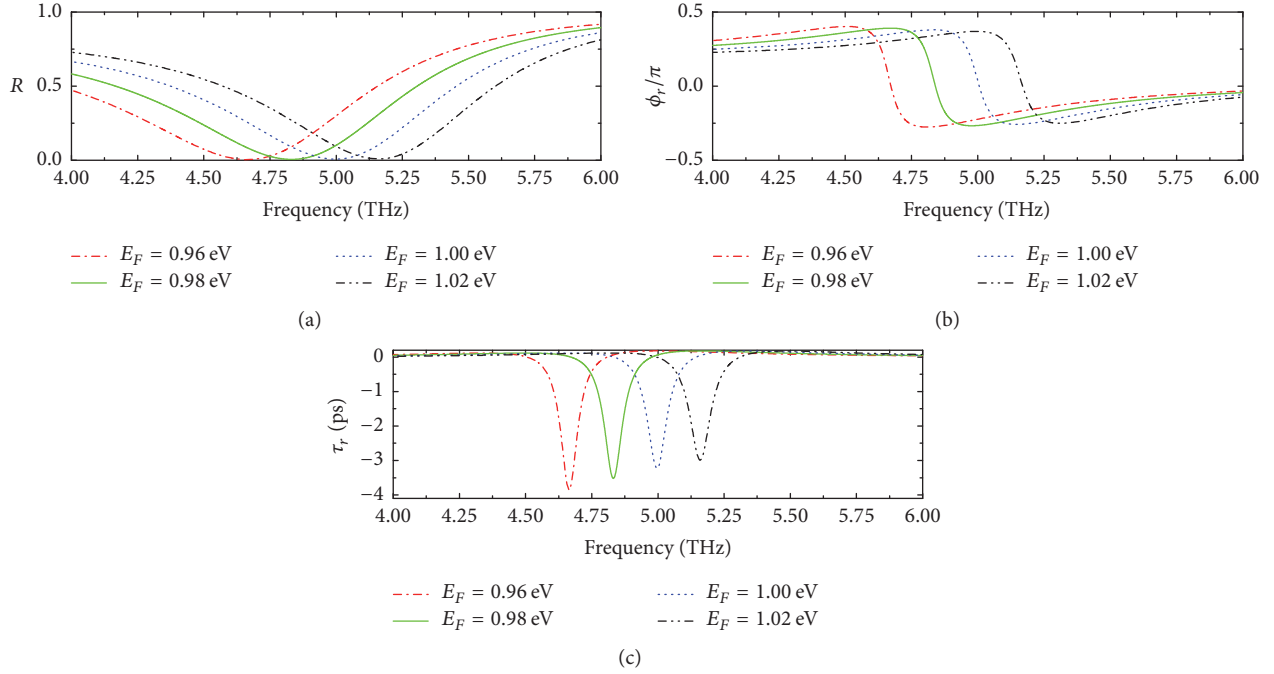


FIGURE 3: (a) Reflectance R , (b) reflected phase ϕ_r , and (c) reflected group delay τ_r as functions of frequency at different Fermi energies for TM polarized wave. Other parameters are the same as before.

refractive index supporting the excitation of SPPs is about $n_{\text{SP}} \approx 3.106$ when the incident frequency equals 5 THz. Hence, it can be inferred that the excitation of SPPs is located at $\theta_{\text{SP}} = \sin^{-1}(n_{\text{SP}}/n_c) \approx 54^\circ$, which is consistent with the position of the dip in Figure 2(a).

3.2. Effects of Fermi Energy on Group Delay. The excitation of SPPs in Otto configuration creates conditions for the occurrence of large reflected group delay, which can steepen the reflected phase at the excitation position, thus making it possible to have large reflected group delay. The reflectance, reflected phase, and reflected group delay in the configuration all vary with frequency; the variation relationship is shown in Figure 3. For convenience, the angle of incidence is assumed as 54° . As shown in Figure 3(a), a remarkable dip of the reflectance is found at the excitation spectrum of SPPs due to SPPs' excitation. This dip is resulted from the interaction of the real part and the imaginary part of the reflectance. Near the frequency that excites SPPs, the real part of the reflectance approaches zero, while the imaginary part has a remarkable monotone increase, leading to a steep monotone decrease tendency of the reflectance-based reflected phase near SPPs excitation frequency as shown in Figure 3(b). According to (3), the above phenomenon will result in large negative group delay as shown in Figure 3(c). Therefore, it can be inferred that a reflected group delay above -3 ps can be realized at 5 THz when Fermi energy satisfies $E_F = 1$ eV. Based on the electrical tunable characteristics of graphene's optical conductivity, the group delay characteristics of the configuration can be flexibly manipulated by adjusting the Fermi energy of graphene. When the Fermi energy is reduced,

the dip will have a blueshift. The reflected phase will be steeper, which will further enhance the negative value of the reflected group delay. For example, when Fermi energy $E_F = 0.96$ eV, the reflected group delay can reach about -4 ps. These electrical tunable characteristics of the reflected group delay provide a means of designing flexible controllable delay devices.

3.3. Numerical Verification. In order to prove the correctness of the reflected group delay obtained from Figure 3, numerical simulations of the pulse's reflected group delay in the whole configuration are conducted based on Fourier transform method. Gaussian pulse is set as the incident pulse, whose electric-field expression can be expressed as $E_i(0, t) = A_0 \exp(-t^2/2\tau_0^2) \exp(-i\omega_0 t)$ [30], where τ_0 and ω_0 represent the temporal width and center frequency of the Gaussian pulse, respectively. The corresponding Fourier spectrum of the Gaussian pulse can then be written as $E_i(0, \omega) = (\tau_0 A_0 / 2\sqrt{\pi}) \exp[-\tau_0^2(\omega - \omega_0)^2/2]$. Large temporal width is selected to reduce the pulse distortion in the frequency domain during the reflection in the configuration. In this paper, it is assumed that $\tau_0 = 50$ ps. The value of the reflected group delay of pulse can be obtained quantitatively by calculating the variation relationship between the reflected pulse and the frequency. Figure 4 is an illustration of the numerical results of normalized group delay under different Fermi energies, corresponding to Figure 3. It can be seen that the reflected group delay time obtained by simulation has a close relationship with Fermi energy. The group delay time of -3 ps (Figure 4(a)), -3.24 ps (Figure 4(b)), -3.52 ps (Figure 4(c)), and -3.85 ps (Figure 4(d)) can be obtained in

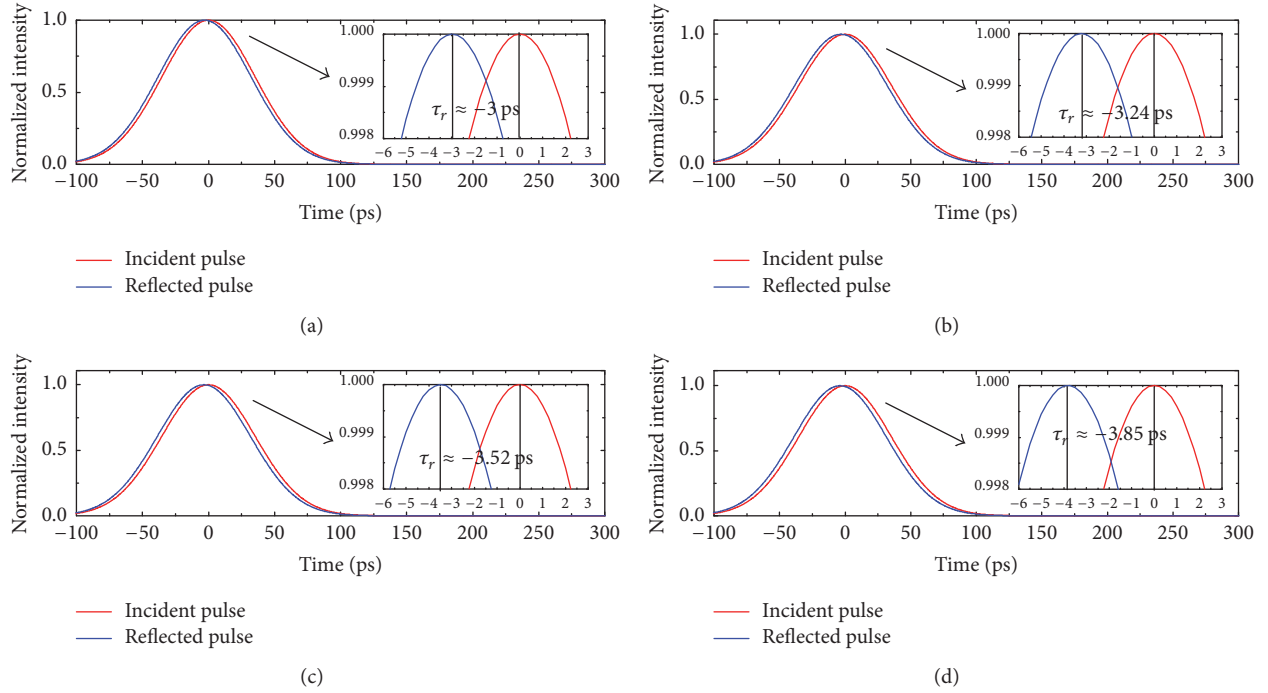


FIGURE 4: Normalized intensity of incident pulse (red line) and corresponding reflected pulse (blue line) for p -polarized wave with (a) $E_F = 1.02$ eV, (b) 1 eV, (c) 0.98 eV, and (d) 0.96 eV. Here, (a) $\omega_0 = 2\pi \times 5.16$ THz, (b) $2\pi \times 5$ THz, (c) $2\pi \times 4.83$ THz, and (d) $2\pi \times 4.66$ THz, respectively.

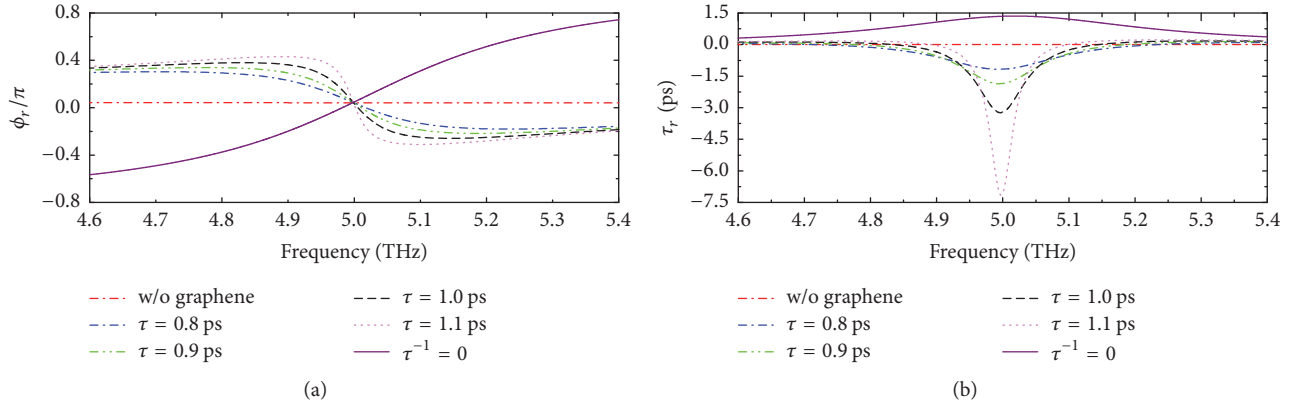


FIGURE 5: The dependence of the reflected phase ϕ_r , (a) and reflected group delay τ_r , (b) on the frequency at different relaxation times τ of the graphene. Other parameters are the same as before.

case of $E_F = 1.02$ eV, $E_F = 1.0$ eV, $E_F = 0.98$ eV, and $E_F = 0.96$ eV. The group delay time is consistent with the results in Figure 3, which further proves the correctness of the delay time of Figure 3.

3.4. Effects of Other Parameters on Group Delay. According to (1), the relaxation time of graphene also has a critical impact on the optical conductivity characteristics of graphene because the actual value of the optical conductivity of graphene is strongly dependent on τ . Besides, the change of optical conductivity will affect the reflection coefficient through the transfer matrix, thus affecting the reflected phase and reflected group delay. Hence, the reflected phase and reflected group delay are also sensitive to the relaxation time

τ . These characteristics provide a new means of regulating the group delay characteristics of reflected pulse. The change rules of the reflected phase and reflected group delay under different relaxation time are presented in Figure 5. Different from the impacts of Fermi energy on reflected phase and reflected group delay, the effect of relaxation time on reflected group delay mainly focuses on the length of the delay time rather than the frequency. Furthermore, it is found that the change of graphene's relaxation time can realize the reversal of the monotony of reflected phase, thus achieving the conversion of the positive and negative values of reflected group delay. As shown in Figure 5(a), when graphene is missing from the configuration, the reflected phase near the resonance frequency is a small value which would hardly

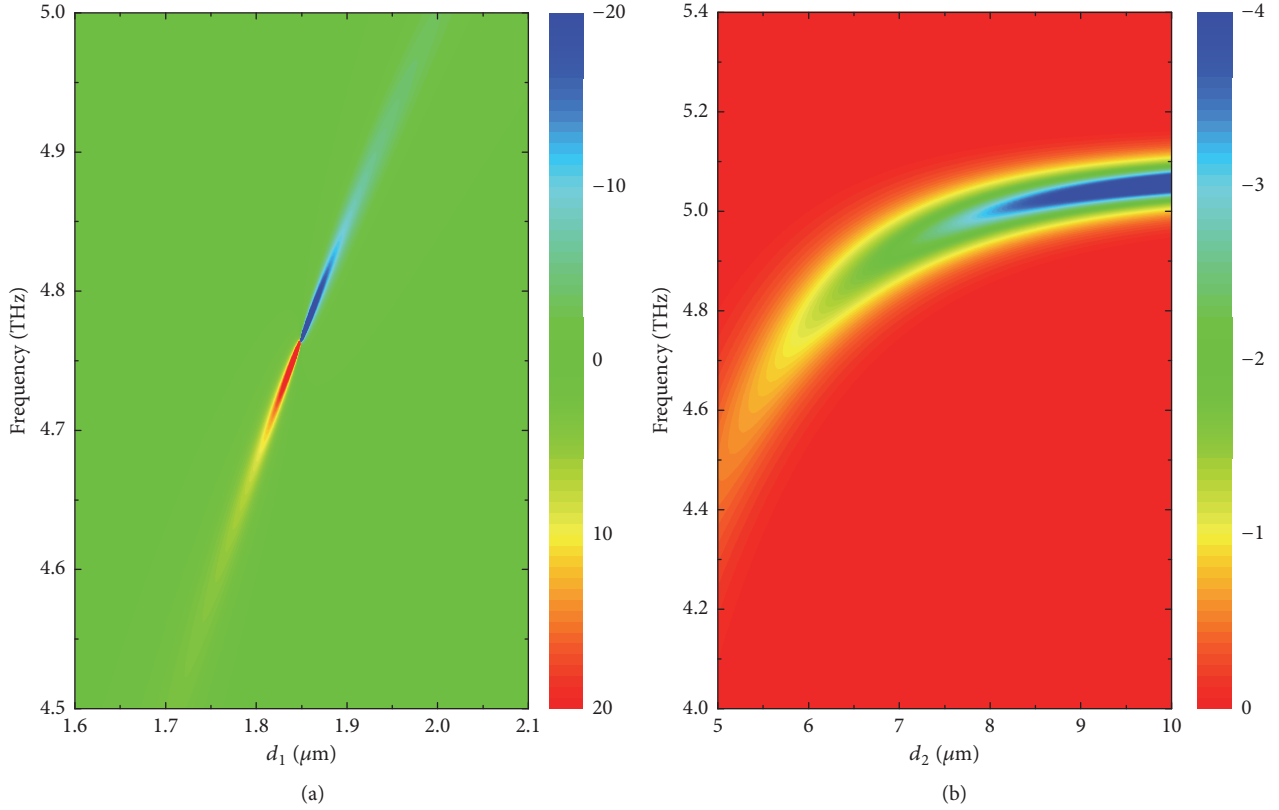


FIGURE 6: (a) Reflected group delay τ_r as a function of frequency and d_1 for the structure with the monolayer graphene. (b) Reflected group delay τ_r as a function of frequency and d_2 for the structure with the monolayer graphene. Other parameters are the same as before.

change. In this case, the group delay time will be very small as well. However, when graphene is included in this configuration, even small relaxation time can make the reflected phase approximate to zero and possess monotone decreasing characteristic near resonance frequency. This property indicates that the configuration has large negative delay time near the resonance point, and this negative delay time would increase remarkably near the resonant frequency with the increase of relaxation time. Particularly, the reflected phase will turn to monotone increasing near resonance frequency due to the pure imaginary characteristic of graphene's conductivity, thus providing conditions for positive reflected group delay. This tunable characteristic is an effective means of converting the delay time symbols. However, it should be noted that it will be very hard to change the relaxation time of the configuration after the preparation of actual group delay devices. Hence, in fixed configuration, the relaxation time has no tuning effect on the group delay characteristics of the whole configuration.

In the following part, the impact of the parameters of Otto configuration on the overall reflected group delay will be discussed. The conclusions can be used for important references in the design of reasonable group delay devices. Figure 6 is the contour plot of reflected group delay of dielectric slabs 1 and 2 thickness under different frequencies. By comparison, it is found that different thicknesses of the dielectric slab have different influences on the reflected group delay, while presenting varied characteristics. Dielectric slab 1 has a direct impact on the excitation of SPPs; hence the

change of its thickness is very sensitive to the characteristics of the reflected group delay. As shown in Figure 6(a), when the thickness is large (e.g., larger than $2 \mu\text{m}$), the condition of exciting SPPs cannot be satisfied and the group delay will approximate to zero. In contrast, the reflected group delay will increase tremendously by reducing the thickness, and it may reach an incredible -20 ps at about $1.85 \mu\text{m}$. Meanwhile, large negative delay will accompany narrow group delay bandwidth. However, a further reduction of thickness may lead to the skipping of the delay time symbol, thus achieving large positive reflected group delay. Different from dielectric slab 1, the change of the thickness of dielectric slab 2 has a relatively simple impact on the reflected group delay. With the thickness of dielectric slab 1 unchanged, a proper increase of d_2 can significantly enhance the negative value of the reflected group delay, with the resonant frequency moving in the high-frequency direction. But when the thickness of d_2 reaches a certain level, the reflected group delay value and resonant frequency will tend to be stable. Hence, it can be concluded that a proper d_2 thickness is a necessary condition to obtain an enhanced reflected delay, which should be taken into consideration in the design of related delay devices.

4. Conclusions

In this paper, the enhanced group delay of pulse reflection is investigated and the surface plasmon is excited in a modified Otto configuration. It is found that the minimum value of

reflected delay time can reach about -4 ps near the resonant angle. Simulation results reveal that the drastic change of phase obtained by the excitation of surface plasmon with graphene is the main factor in the enhancement and tuning of the reflected group delay properties. The enhanced group delay depends on the conductivity characteristic of graphene at the center frequency. The findings reveal that the group delay depends on the distance between the coupling prism and the graphene, and the thickness of substrate, above which the huge delay is observed. These findings could provide an effective method for enhancing the group delay of optical pulse and offer a feasible pathway for manipulating the delay properties. It is believed that the tunable reflected group delay at terahertz bands could contribute to the application of optical delay devices.

Conflicts of Interest

The authors declare that they have no conflicts of interest.

Acknowledgments

This work is partially supported by the Hunan Science and Technology Plan Project: Research on Key Technologies of photovoltaic inverter system (2015GK3035), the National Natural Science Foundation of China (Grant nos. 11647135 and 11704119), the Scientific Research Fund of Hunan Provincial Education Department (Grant no. 17C0945), and University Student Innovation Program of Hunan Normal University (Grant no. 2017090).

References

- [1] M. S. Bigelow, N. N. Lepeshkin, and R. W. Boyd, "Superluminal and slow light propagation in a room-temperature solid," *Science*, vol. 301, no. 5630, pp. 200–202, 2003.
- [2] R. W. Boyd, D. J. Gauthier, and A. L. Gaeta, "Applications of slow-light in telecommunications," *Optics Photonics News*, vol. 17, no. 4, pp. 18–23, 2006.
- [3] Y. Okawachi, M. S. Bigelow, J. E. Sharping et al., "Tunable all-optical delays via Brillouin slow light in an optical fiber," *Physical Review Letters*, vol. 94, no. 15, 2005.
- [4] H. Mirzaei and G. V. Eleftheriades, "Arbitrary-angle squint-free beamforming in series-fed antenna arrays using non-Foster elements synthesized by negative-group-delay networks," *Institute of Electrical and Electronics Engineers Transactions on Antennas and Propagation*, vol. 63, no. 5, pp. 1997–2010, 2015.
- [5] T. F. Krauss, "Why do we need slow light?" *Nature Photonics*, vol. 2, no. 8, pp. 448–450, 2008.
- [6] J. Gu, R. Singh, X. Liu et al., "Active control of electromagnetically induced transparency analogue in terahertz metamaterials," *Nature Communications*, vol. 3, article 1151, 2012.
- [7] L.-G. Wang and S.-Y. Zhu, "Superluminal pulse reflection from a weakly absorbing dielectric slab," *Optics Letters*, vol. 31, no. 14, pp. 2223–2225, 2006.
- [8] L. Jiang, X. Dai, Y. Xiang, and S. Wen, "Tunable group delay of the optical pulse reflection from Fabry-Pérot cavity with the insertion of graphene sheets," *IEEE Photonics Journal*, vol. 6, no. 6, 2014.
- [9] S. Dutta Gupta, R. Arun, and G. S. Agarwal, "Subluminal to superluminal propagation in a left-handed medium," *Physical Review B*, vol. 69, no. 11, 2004.
- [10] S. Manipatrani, P. Dong, Q. Xu, and M. Lipson, "Tunable superluminal propagation on a silicon microchip," *Optics Letters*, vol. 33, no. 24, pp. 2928–2930, 2008.
- [11] H. Choi, Y. Jeong, C. D. Kim, and J. S. Kenney, "Efficiency enhancement of feedforward amplifiers by employing a negative group-delay circuit," *IEEE Transactions on Microwave Theory and Techniques*, vol. 58, no. 5, pp. 1116–1125, 2010.
- [12] H.-Y. Yao, N. C. Chen, T.-H. Chang, and H. G. Winful, "Tunable Negative Group Delay in a Birefringent Fabry-Pérot-Like Cavity with High Fractional Advancement Induced by Cross-Interference Effect," *IEEE Transactions on Microwave Theory and Techniques*, vol. PP, no. 99, 2016.
- [13] F. Bonaccorso, Z. Sun, T. Hasan, and A. C. Ferrari, "Graphene photonics and optoelectronics," *Nature Photonics*, vol. 4, no. 9, pp. 611–622, 2010.
- [14] L. A. Falkovsky and A. A. Varlamov, "Space-time dispersion of graphene conductivity," *The European Physical Journal B*, vol. 56, no. 4, pp. 281–284, 2007.
- [15] Z. Q. Li, E. A. Henriksen, Z. Jiang et al., "Dirac charge dynamics in graphene by infrared spectroscopy," *Nature Physics*, vol. 4, no. 7, pp. 532–535, 2008.
- [16] Q. Bao, K. P. Loh, G. Eda, and M. Chhowalla, "Graphene photonics, plasmonics, and broadband optoelectronic devices," *ACS Nano*, vol. 6, pp. 3677–3694, 2012.
- [17] A. H. Castro Neto, F. Guinea, N. M. R. Peres, K. S. Novoselov, and A. K. Geim, "The electronic properties of graphene," *Reviews of Modern Physics*, vol. 81, no. 1, pp. 109–162, 2009.
- [18] N. M. R. Peres, Y. V. Bludov, J. E. Santos, A.-P. Jauho, and M. I. Vasilevskiy, "Optical bistability of graphene in the terahertz range," *Physical Review B - Condensed Matter and Materials Physics*, vol. 90, no. 12, Article ID 125425, 2014.
- [19] S. A. Mikhailov and K. Ziegler, "New electromagnetic mode in graphene," *Physical Review Letters*, vol. 99, no. 1, Article ID 016803, 2007.
- [20] F. H. L. Koppens, D. E. Chang, and F. J. García de Abajo, "Graphene plasmonics: a platform for strong light-matter interactions," *Nano Letters*, vol. 11, no. 8, pp. 3370–3377, 2011.
- [21] Y. V. Bludov, M. I. Vasilevskiy, and N. M. R. Peres, "Tunable graphene-based polarizer," *Journal of Applied Physics*, vol. 112, no. 8, Article ID 084320, 2012.
- [22] X. Dai, L. Jiang, and Y. Xiang, "Tunable THz angular/frequency filters in the modified kretschmann-raether configuration with the insertion of single layer graphene," *IEEE Photonics Journal*, vol. 7, no. 2, 2015.
- [23] H. Wang, J. Wu, J. Guo, L. Jiang, Y. Xiang, and S. Wen, "Low-threshold optical bistability with multilayer graphene-covering Otto configuration," *Journal of Physics D: Applied Physics*, vol. 49, no. 25, Article ID 255306, 2016.
- [24] Y. Luo, V. K. Guda, E. B. Hassan, P. H. Steele, B. Mitchell, and F. Yu, "Hydrodeoxygenation of oxidized distilled bio-oil for the production of gasoline fuel type," *Energy Conversion and Management*, vol. 112, pp. 319–327, 2016.
- [25] B. Ding, Y. Cheng, J. Wu et al., "A unique multifunctional cluster-based nano-porous Terbium organic material: Real-time detection of benzaldehyde, visually luminescent sensor for nitrite and selective high capacity capture of Congo Red," *Dyes and Pigments*, vol. 146, pp. 455–466, 2017.

- [26] Q. Xu, H. Xu, J. Chen, Y. Lv, C. Dong, and T. S. Sreeprasad, "Graphene and graphene oxide: Advanced membranes for gas separation and water purification," *Inorganic Chemistry Frontiers*, vol. 2, no. 5, pp. 417–424, 2015.
- [27] L. Jiang, J. Guo, Q. Wang, X. Dai, and Y. Xiang, "Perfect Terahertz Absorption with Graphene Surface Plasmons in the Modified Otto Configuration," *Plasmonics*, pp. 1–7, 2016.
- [28] Y. Xiang, X. Dai, J. Guo, S. Wen, and D. Tang, "Tunable optical bistability at the graphene-covered nonlinear interface," *Applied Physics Letters*, vol. 104, no. 5, Article ID 051108, 2014.
- [29] T. Zhan, X. Shi, Y. Dai, X. Liu, and J. Zi, "Transfer matrix method for optics in graphene layers," *Journal of Physics Condensed Matter*, vol. 25, no. 21, Article ID 215301, 2013.
- [30] L.-G. Wang, H. Chen, and S.-Y. Zhu, "Superluminal pulse reflection and transmission in a slab system doped with dispersive materials," *Physical Review E - Statistical, Nonlinear, and Soft Matter Physics*, vol. 70, no. 6, Article ID 066602, p. 066602/6, 2004.

Research Article

Tunable Optical Bistability in One-Dimensional Photonic Crystal with a Nonlinear Defect Coupled by Graphene Sheets

Zhiwei Zheng,^{1,2} Leyong Jiang,² Jun Guo,¹ Xiaoyu Dai,¹ and Yuanjiang Xiang¹

¹*SZU-NUS Collaborative Innovation Center for Optoelectronic Science and Technology, Key Laboratory of Optoelectronic Devices and Systems of Ministry of Education and Guangdong Province, College of Optoelectronic Engineering, Shenzhen University, Shenzhen 518060, China*

²*College of Physics and Information Science, Hunan Normal University, Changsha 410081, China*

Correspondence should be addressed to Jun Guo; guojun@szu.edu.cn and Xiaoyu Dai; xiaoyudai@126.com

Received 26 June 2017; Accepted 29 August 2017; Published 1 November 2017

Academic Editor: Yan Luo

Copyright © 2017 Zhiwei Zheng et al. This is an open access article distributed under the Creative Commons Attribution License, which permits unrestricted use, distribution, and reproduction in any medium, provided the original work is properly cited.

The optical bistability in one-dimensional photonic crystal (1DPC) with a nonlinear defect is investigated. It is demonstrated that, by introducing graphene layers into the nonlinear defect, the optical bistability in 1DPC can be changed significantly. The hysteresis threshold increases with the number of graphene monolayers and can be lowered or enhanced by tuning the Fermi energy of graphene. On the other hand, the hysteresis width and the nonlinear lateral shift can also be controlled by varying the Fermi energy and the number of graphene monolayers. These results may be useful for controlling the optical bistability and nonlinear lateral shift in 1DPCs.

1. Introduction

Optical bistability is a kind of optical phenomenon where one input state can induce two steady transmission states [1]. The input and output intensity in the system can then form a hysteresis loop. One of the simplest examples of bistable systems is a Fabry-Perot cavity filled with a medium which presents saturable absorption or nonlinear dispersion. In recent years, nonlinear photonic crystal formed by introducing Kerr nonlinear material into periodical structure has been proposed to achieve optical bistability [2–5]. Due to the dynamic shifting of the band edge and the strong intensity localized inside the defect mode, the threshold for the onset of optical bistability can be lowered. However, it is hard to control the threshold value in fixed configuration. Hence, the exploration of new optical material with tunable optical properties is important for dynamically tunable optical switches.

Graphene, a single layer of carbon atoms in a hexagonal lattice, has given birth to a new branch of modern optics and new possibilities for manipulating light waves, due to its unique optical and electronic properties [6–9]. Although graphene is atomically thin, it can strongly interact with light over a wide frequency spectrum and has been

demonstrated for various photonic applications from photodetectors, ultrafast mode lockers to modulators [10–13]. The linear optical properties in graphene lead to broadband and tunable optical features from IR to visible spectrum [14–16]. The broadband optical property allows graphene to be used as an intrinsically smart optical material for the building block of light controlling system. Recently, the optical bistability of reflection at the interface between graphene and Kerr-type nonlinear substrates was investigated theoretically, and the influence of graphene sheets on the hysteretic response of the nonlinear interface was discussed [17]. It was found that the bistable behavior of the reflected light can be electrically controlled by suitably varying the applied voltage on the graphene. Moreover, the optical bistability in nonlinear photonic crystals exhibits rich nonlinear dynamic behaviors. Hence, the nonlinear photonic crystal coupled with graphene sheets will provide a new scheme to control the hysteresis response of the transmitted light intensity. Moreover, the phase of the transmitted (or reflected) light also exhibits bistable behaviors, thus leading to the hysteresis response of the lateral shift of the transmitted light. We believe that the controllable graphene optical bistable devices could find potential applications in optical all-optical

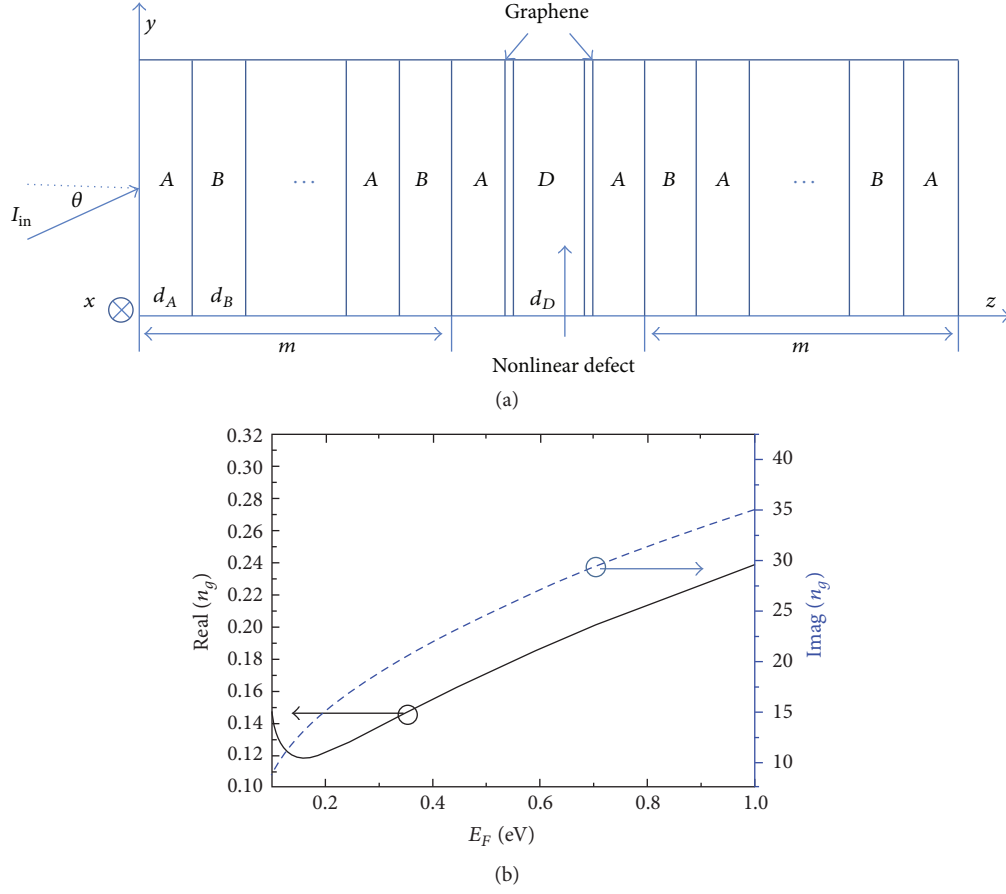


FIGURE 1: (a) The schematic diagram of a 1DPC with a nonlinear defect and graphene layers. m represents the number of periods. (b) Complex effective refractive index of graphene n_g as function of E_F . The solid line and dashed line represent real and imaginary components respectively.

switching [18, 19], optical memory [20], and chemical science [21–23].

2. The Proposed Structure and Simulation Method

This paper is proposed to utilize the tunable features of graphene and to explore the tunable nonlinear transmission features of optical bistability, such as the manipulation of hysteresis threshold, hysteresis width, and nonlinear lateral shift. One-dimensional photonic crystal (1DPC) containing a graphene coupled nonlinear defect is taken as an example.

The structure is shown in Figure 1(a), consisting of two alternate linear layers A and B as 1DPC and a Kerr-type nonlinear layer as defect with effective refraction index $n(I) = n_D + n_2 I$, where n_D is the linear refractive index of the nonlinear defect material, I is the intensity of optical field, and n_2 is the nonlinear refractive. In the following discussion, a normalized unit has been used, which is expressed in units of n_2^{-1} , so that the results will be valid for all Kerr materials with the same n_D and different n_2 [24]. The alternate layers of A, B have high and low linear refractive index n_A, n_B and their thicknesses d_A and d_B satisfy $n_A d_A = n_B d_B = \lambda_{PC}/4$ (the refractive indexes of SiO_2 and TiO_2 are 1.47 and 2.1, resp.). Such a system has a band gap with $2\pi c/\lambda_{PC}$ as the center

frequency for the case of normal incidence. The graphene layers are incorporated into both sides of the nonlinear defect layer as shown in Figure 1(a). Both of their graphene thicknesses are set to be $0.34 \times N$ nm, and N indicates the graphene is multilayered with N monolayer(s). The thickness of a monolayer graphene is chosen to be 0.34 nm [25].

Graphene can be characterized by a complex surface conductivity σ , which is a function of angular frequency $\omega = 2\pi c/\lambda$, Fermi energy E_F , carrier scattering rate Γ , and absolute temperature T of the environment. σ is obtained by intraband and interband $\sigma = \sigma_{\text{intra}} + \sigma_{\text{inter}}$ terms, which can be expressed according to the Kubo formula [26]:

$$\sigma_{\text{intra}} = i \frac{e^2 k_B T}{\pi \hbar^2 (\omega + i\Gamma)} \left[\frac{E_F}{k_B T} + 2 \ln \left(e^{-E_F/k_B T} + 1 \right) \right], \quad (1)$$

$$\sigma_{\text{inter}} = i \frac{e^2}{4\pi \hbar} \ln \left[\frac{2E_F - (\omega + i\Gamma) \hbar}{2E_F + (\omega + i\Gamma) \hbar} \right].$$

In the above formulas, e is the elementary charge, $\hbar = h/2\pi$ is the reduced Planck constant, and k_B is the Boltzmann constant. The Fermi energy of graphene can be manipulated via different approaches, including voltage biasing, exposure to magnetic fields, and chemical doping, which then provide various avenues to control the electronic band property

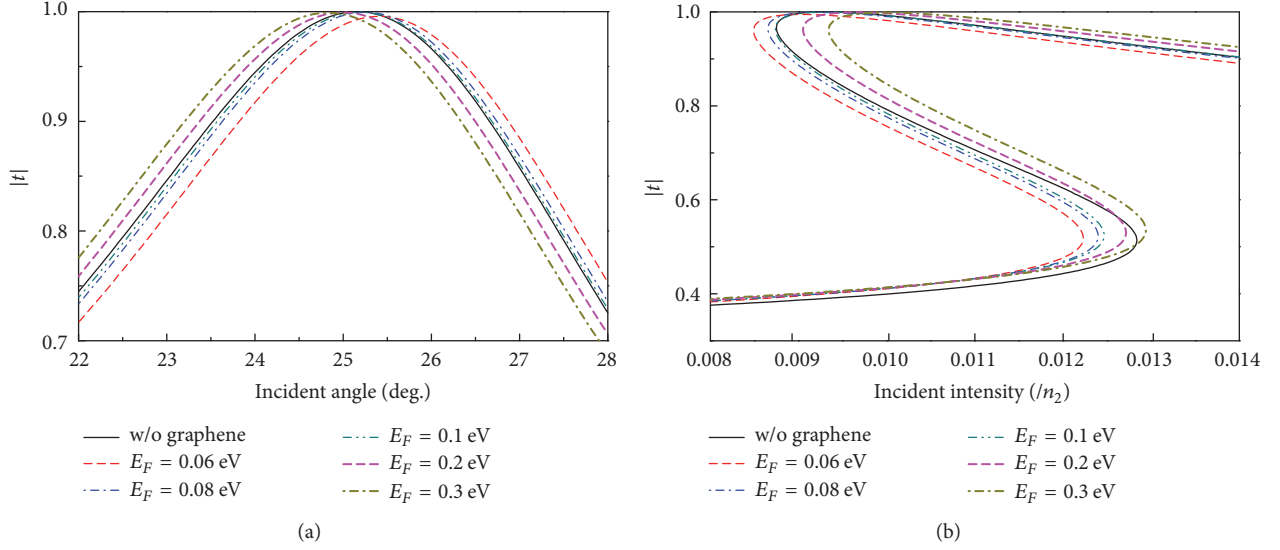


FIGURE 2: (a) $|t|$ versus the angle of incidence for structure without graphene layers (solid curve), with graphene layers of which $E_F = 0.06$ eV (dashed line), $E_F = 0.08$ eV (dash-dotted line), $E_F = 0.1$ eV (dash-dot-dotted line), $E_F = 0.2$ eV (bold dashed line), and $E_F = 0.3$ eV (bold dash-dotted line). (b) $|t|$ versus the incident intensity corresponding to the five situations mentioned in (a).

of graphene [9, 15]. In this research, the graphene carrier scattering rate is assumed to be $\Gamma = 2.4$ THz, the temperature $T = 300$ K, and the incident wavelength $\lambda = 10.6 \mu\text{m}$ (the wavelength of CO_2 lasers). In the simulations, graphene is assumed to be a homogenous medium with small thickness, and then the effective refractive index can be derived by $n_g = \sqrt{1 + i\sigma/(\omega\epsilon_0 d)}$ [15], where $d = 0.34$ nm is the thickness of monolayer graphene. Note that n_g is independent of N , the layer number of a multilayered graphene. Figure 1(b) shows the complex effective refractive index of graphene n_g as function of E_F at the incident wavelength $\lambda = 10.6 \mu\text{m}$. It can be seen that graphene has complex n_g , indicating that the graphene behaves like a very thin metal layer. The solid line implies the real part of n_g , while the dashed line is the imaginary part of n_g . As shown, both of them increase with E_F , and the imaginary part is larger than the real one.

In this paper, we suppose a TE-polarized wave with wavelength λ incident from vacuum upon a finite 1DPC at angle of 27 degrees. In the following discussion, we consider the symmetric multilayer stack consisting of two alternate linear layers A and B as our 1DPC structure. The middle layer is a Kerr-type nonlinear layer. The nonlinear defect layer is sandwiched between two monolayer graphene. The parameters are set as follows: $n_A = 2.1$, $n_B = 1.47$, $n_D = 1.594$, $d_D = 3.5 \mu\text{m}$, $\theta = 27^\circ$, $\lambda = 10.6 \mu\text{m}$, and $m = 3$, where d_D and m are the thickness of nonlinear defect layer and the period number of 1DPC, respectively [27]. By applying the transfer matrix method, the characteristic matrix for the nonlinear layer and the composite medium can be calculated. Then the transmission coefficient t can be given by [28]

$$t(k_y) = \frac{2p_f(k_y)}{[M_{11} + M_{12}p_f(k_y)]p_f(k_y) + [M_{21} + M_{22}p_f(k_y)]}, \quad (2)$$

where $p_f(k_y) = (k^2 - k_y^2)^{1/2}/k$ and $M_{ij}(k_y)$ are the elements of 2×2 matrix $M(k_y)$.

The phase shift of the transmitted beam with respect to the incident beam is defined as [29]

$$\phi(k_y) = \tan^{-1} \left[\frac{\text{Im } t(k_y)}{\text{Re } t(k_y)} \right], \quad (3)$$

where k_y is the y component of the incident wave vector. Then the lateral shift Δ of the transmitted beam through the multilayered structure is

$$\Delta = \left. \frac{-d\phi(k_y)}{dk_y} \right|_{\theta=\theta_0}. \quad (4)$$

3. Results and Discussion

First, the angular dependence of transmission coefficient with and without graphene is considered. n_g can be manipulated by setting different E_F values, and $N = 5$ is chosen for the calculation. Figure 2(a) shows the angular dependence of transmission coefficient for structures with and without graphene. As shown, although the graphene layers are very thin, their effects on the nonlinear optical response of the entire structure turn out to be significant. The numerical results for the relation between the normalized incident intensity and transmission coefficient for the same cases in Figure 2(a) are also demonstrated in Figure 2(b), in which a typical S-shaped curve indicates that such a system operates in an optical bistable regime. Figure 2(b) shows that when $E_F = 0.06$ eV, the bistability threshold decreases compared to the case without graphene layers. But when $E_F = 0.3$ eV, the bistability threshold increases. To understand the mechanism that accounts for this variation, the structure

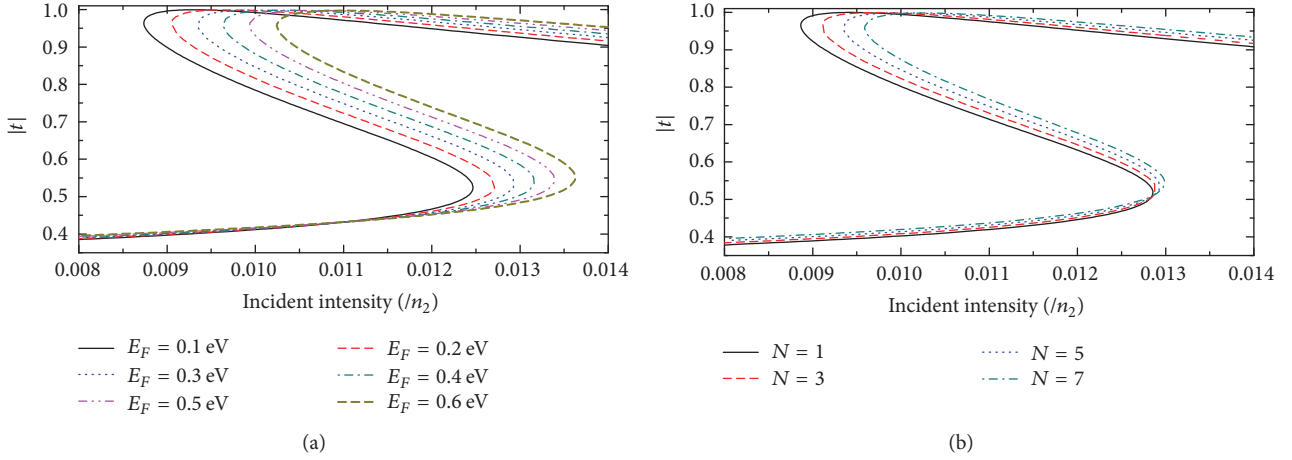


FIGURE 3: $|t|$ versus the incident intensity for graphene with (a) different E_F and $N = 5$ and (b) with different N and $E_F = 0.3$ eV. The incident angle $\theta = 27^\circ$.

in Figure 1(a) can be considered as a resonator filled with nonlinear materials. As shown in Figure 1(b), the effective refractive index of graphene includes the imaginary part and the real part, which indicates that graphene behaves like a thin metal layer. The addition of graphene layers introduces extra positive phase shift and energy loss because of the real part and the imaginary part of n_g . The real part of n_g introduces a positive phase shift, and then the “resonator” length increases. As a result, the intensity dependent nonlinear index change required for switching the system could correspondingly decrease; for example, the intensity required should decrease. The imaginary part of n_g introduces additional energy loss, implying that the input intensity must be higher in order to reach the same “resonator” state. Correspondingly, the intensity required for switching the system should increase. Given that n_g shows both the real part and the imaginary part, each part will impact the nonlinear transmission in an opposite and competitive way, leading to an S shape curve as in Figure 2. As shown in Figure 1(b), both the real part and the imaginary part of n_g increase with E_F , whereas the imaginary part is larger and increases faster than the real part. Therefore, when E_F is smaller, the effect of the real part of n_g is more significant than that of the imaginary part; besides, the intensity required for switching the system decreases compared to the case without graphene. And as E_F becomes larger, the effect of the imaginary part of n_g increases faster than that of the real part. So, with larger E_F , the effect of imaginary part is more significant and the intensity required for switching the system increases. The numerical results shown in Figure 2(b) can prove the above discussion.

Secondly, the effects of graphene layers with different E_F or N on the transmission coefficient are discussed to verify the tunability of graphene layers. Figure 3(a) shows the transmission coefficient dependence on the normalized incident intensity for graphene layers with different E_F . Figure 3(b) is for graphene layers with different N . In Figure 3(a), $N = 5$ while the value of E_F varies. As shown, the hysteresis threshold increases with E_F . It can also be interpreted by the simple resonator analogy mentioned above. When E_F

increases, the effect of the imaginary part of n_g (energy loss) becomes more significant, so that both the switch-up and switch-down thresholds will increase. As the switch-up threshold increases faster than the switch-down threshold, the hysteresis width will increase with E_F . In Figure 3(b), the study sets $E_F = 0.3$ eV and varies N and shows the transmission coefficient versus normalized incident intensity. The results are similar to those in Figure 3(a). However, in this case n_g does not change with different N values. The hysteresis threshold increases as N becomes larger. Although n_g is fixed to be constant, the total thickness of multilayered graphene increases with N , so both the additional positive phase shifts and the energy loss increase. Due to the larger imaginary part of n_g , energy loss would increase faster and the hysteresis threshold will increase subsequently. However, the switch-up and switch-down thresholds will increase at the same speed so the hysteresis width will be kept the same.

Lastly, the effects of graphene layers with different E_F or N values on the lateral shift of the transmitted beam are analyzed. Figure 4(a) shows the lateral shift versus the normalized incident intensity for graphene with different E_F , while Figure 4(b) is for the case with different N . It is clear that the hysteretic effect of lateral shift on the incident intensity occurs. As the incident intensity increases, the lateral shift can be switched to a very large value if the incident intensity is larger than the switch-on threshold intensity, which will then enhance the lateral shift. However, as the incident intensity decreases, the lateral shift can be switched to a very small value when the incident intensity is smaller than the switch-down threshold intensity and hence depress the lateral shift. Moreover, the optical properties of graphene sheets exert an important influence on the hysteretic responses of the lateral shifts. Figure 4(a) sets $N = 5$ and varies the value of E_F . As shown, the variation of Δ with different E_F is similar to the transmission coefficient. Both the hysteresis threshold and the hysteresis width increase with E_F . The maximum value of Δ appears near the switch-down threshold and decreases slightly as E_F increases. Figure 4(b) sets $E_F = 0.3$ eV and varies N . As shown, the hysteresis threshold

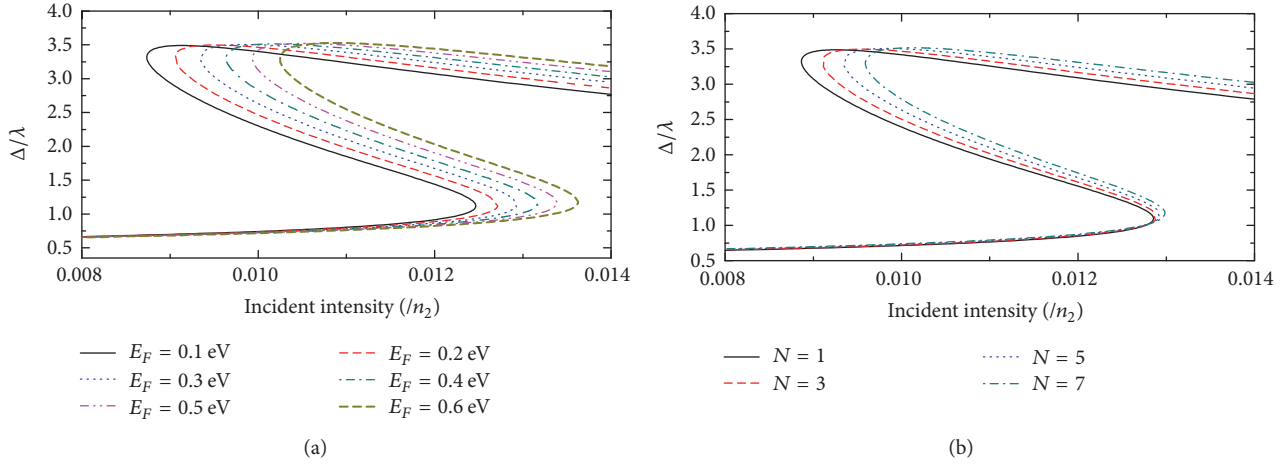


FIGURE 4: The lateral shift versus the normalized incident intensity for graphene with (a) different E_F and $N = 5$ and (b) different N and $E_F = 0.3$ eV. The incident angle $\theta = 27^\circ$.

increases as N becomes larger. Hence, the electrical tunability of optical bistability with graphene could potentially open a new possibility of controlling the lateral shift in a fixed configuration.

4. Conclusions

In summary, this paper mainly explores the effect of multi-layered graphene on a nonlinear 1DPC by attaching graphene layers to both sides of the nonlinear defect. It is found that though the graphene layers are very thin, they can significantly modify the nonlinear transmission response, containing the hysteresis threshold, the hysteresis width, and the nonlinear lateral shift. In addition, the influences of graphene layers with different Fermi energy and different number of monolayers are analyzed, and the hysteresis threshold shifts by analog of a resonator filled with nonlinear materials are discussed. The results show that the hysteresis threshold increases with Fermi energy and the hysteresis width increases at the same time. Besides, the hysteresis threshold also increases with the number of graphene monolayers. These results may be useful for the control of the optical bistability in 1DPCs.

Conflicts of Interest

The authors declare that there are no conflicts of interest regarding the publication of this paper.

Acknowledgments

This work is partially supported by the National Natural Science Foundation of China (Grant nos. 11647135 and 11704119), Hunan Provincial Natural Science Foundation of China (Grant no. 14JJ6007), Scientific Research Fund of Hunan Provincial Education Department (Grant no. 14B119), and the Project Supported for Excellent Talents in Hunan Normal University (Grant no. ET1502).

References

- [1] N. M. Litchinitser, I. R. Gabitov, A. I. Maimistov, and V. M. Shalaev, "Effect of an optical negative index thin film on optical bistability," *Optics Letters*, vol. 32, no. 2, pp. 151–153, 2007.
- [2] M. Soljacic and J. D. Joannopoulos, "Enhancement of nonlinear effects using photonic crystals," *Nature Materials*, vol. 3, no. 4, pp. 211–219, 2004.
- [3] F. Y. Wang, G. X. Li, H. L. Tam, K. W. Cheah, and S. N. Zhu, "Optical bistability and multistability in one-dimensional periodic metal-dielectric photonic crystal," *Applied Physics Letters*, vol. 92, no. 21, Article ID 211109, 2008.
- [4] J. Guo, L. Jiang, Y. Jia, X. Dai, Y. Xiang, and D. Fan, "Low threshold optical bistability in one-dimensional gratings based on graphene plasmonics," *Optics Express*, vol. 25, no. 6, pp. 5972–5981, 2017.
- [5] S. Chen, L. Miao, X. Chen et al., "Few-Layer Topological Insulator for All-Optical Signal Processing Using the Nonlinear Kerr Effect," *Advanced Optical Materials*, vol. 3, no. 12, pp. 1769–1778, 2015.
- [6] A. K. Geim and K. S. Novoselov, "The rise of graphene," *Nature Materials*, vol. 6, no. 3, pp. 183–191, 2007.
- [7] Z. Zheng, C. Zhao, S. Lu et al., "Microwave and optical saturable absorption in graphene," *Optics Express*, vol. 20, no. 21, pp. 23201–23214, 2012.
- [8] F. Bonaccorso, Z. Sun, T. Hasan, and A. C. Ferrari, "Graphene photonics and optoelectronics," *Nature Photonics*, vol. 4, no. 9, pp. 611–622, 2010.
- [9] A. H. Castro Neto, F. Guinea, N. M. R. Peres, K. S. Novoselov, and A. K. Geim, "The electronic properties of graphene," *Reviews of Modern Physics*, vol. 81, no. 1, pp. 109–162, 2009.
- [10] M. Liu, X. Yin, E. Ulin-Avila et al., "A graphene-based broadband optical modulator," *Nature*, vol. 474, no. 7349, pp. 64–67, 2011.
- [11] H. Zhang, D. Tang, R. J. Knize, L. Zhao, Q. Bao, and K. P. Loh, "Graphene mode locked, wavelength-tunable, dissipative soliton fiber laser," *Applied Physics Letters*, vol. 96, no. 11, Article ID 111112, 2010.
- [12] Y. Chen, G. Jiang, S. Chen et al., "Mechanically exfoliated black phosphorus as a new saturable absorber for both Q-switching

- and mode-locking laser operation,” *Optics Express*, vol. 23, no. 10, pp. 12823–12833, 2015.
- [13] G. Gong, H. Zhang, and M. Yao, “Speckle noise reduction algorithm with total variation regularization in optical coherence tomography,” *Optics Express*, vol. 23, no. 19, pp. 24699–24712, 2015.
- [14] E. Simsek, “Improving tuning range and sensitivity of localized SPR sensors with graphene,” *IEEE Photonics Technology Letters*, vol. 25, no. 9, pp. 867–870, 2013.
- [15] W. Zhu, I. D. Rukhlenko, L.-M. Si, and M. Premaratne, “Graphene-enabled tunability of optical fishnet metamaterial,” *Applied Physics Letters*, vol. 102, no. 12, Article ID 121911, 2013.
- [16] S. H. Mousavi, I. Kholmanov, K. B. Alici et al., “Inductive tuning of fano-resonant metasurfaces using plasmonic response of graphene in the mid-infrared,” *Nano Letters*, vol. 13, no. 3, pp. 1111–1117, 2013.
- [17] Y. Xiang, X. Dai, J. Guo, S. Wen, and D. Tang, “Tunable optical bistability at the graphene-covered nonlinear interface,” *Applied Physics Letters*, vol. 104, no. 5, Article ID 051108, 2014.
- [18] D. A. Mazurenko, R. Kerst, J. I. Dijkhuis et al., “Ultrafast optical switching in three-dimensional photonic crystals,” *Physical Review Letters*, vol. 91, no. 21, p. 213903/4, 2003.
- [19] L. Jiang, J. Guo, L. Wu, X. Dai, and Y. Xiang, “Manipulating the optical bistability at terahertz frequency in the Fabry-Perot cavity with graphene,” *Optics Express*, vol. 23, no. 24, pp. 31181–31191, 2015.
- [20] H. Nihei and A. Okamoto, “Switching time of optical memory devices composed of photonic crystals with an impurity three-level atom,” *Japanese Journal of Applied Physics, Part 1: Regular Papers and Short Notes and Review Papers*, vol. 40, no. 12, pp. 6835–6840, 2001.
- [21] J. Liu, L. Yu, Z. Zhao et al., “Potassium-modified molybdenum-containing SBA-15 catalysts for highly efficient production of acetaldehyde and ethylene by the selective oxidation of ethane,” *Journal of Catalysis*, vol. 285, no. 1, pp. 134–144, 2012.
- [22] Y. Luo, V. K. Guda, E. B. Hassan, P. H. Steele, B. Mitchell, and F. Yu, “Hydrodeoxygenation of oxidized distilled bio-oil for the production of gasoline fuel type,” *Energy Conversion and Management*, vol. 112, pp. 319–327, 2016.
- [23] Q. Xu, H. Xu, J. Chen, Y. Lv, C. Dong, and T. S. Sreepasad, “Graphene and graphene oxide: Advanced membranes for gas separation and water purification,” *Inorganic Chemistry Frontiers*, vol. 2, no. 5, pp. 417–424, 2015.
- [24] P. Hou, Y. Chen, X. Chen, J. Shi, and Q. Wang, “Giant bistable shifts for one-dimensional nonlinear photonic crystals,” *Physical Review A - Atomic, Molecular, and Optical Physics*, vol. 75, no. 4, Article ID 045802, 2007.
- [25] K. S. Novoselov, A. K. Geim, S. V. Morozov et al., “Electric field in atomically thin carbon films,” *Science*, vol. 306, no. 5696, pp. 666–669, 2004.
- [26] B. Vasic, M. M. Jakovljević, G. Isić, and R. Gajić, “Tunable metamaterials based on split ring resonators and doped graphene,” *Applied Physics Letters*, vol. 103, no. 1, p. 011102, 2013.
- [27] W. L. Zhang and S. F. Yu, “Bistable switching using an optical Tamm cavity with a Kerr medium,” *Optics Communications*, vol. 283, no. 12, pp. 2622–2626, 2010.
- [28] J. A. Porto, L. Martín-Moreno, and F. J. García-Vidal, “Optical bistability in subwavelength slit apertures containing nonlinear media,” *Physical Review B - Condensed Matter and Materials Physics*, vol. 70, no. 8, pp. 1–81402, 2004.
- [29] L. Jiang, Q. Wang, Y. Xiang, X. Dai, and S. Wen, “Electrically tunable Goos-Hänchen shift of light beam reflected from a graphene-on-dielectric surface,” *IEEE Photonics Journal*, vol. 5, no. 3, 2013.

Research Article

Effective Generation of Milliwatt-Level Sub-Terahertz Wave for Nonlinear Response Measurement of Two-Dimensional Material by Optical Heterodyne Technique

Shuqing Chen,¹ Zhiqiang Xie,¹ Junmin Liu,¹ Yanliang He,¹ Yao Cai,¹
Xiaoke Zhang,¹ Jiangnan Xiao,² Ying Li,¹ and Dianyuan Fan¹

¹International Collaborative Laboratory of 2D Materials for Optoelectronics Science and Technology and Key Laboratory of Optoelectronic Devices and Systems of Ministry of Education and Guangdong Province, Shenzhen University, Shenzhen 518060, China

²Key Laboratory for Information Science of Electromagnetic Waves, Fudan University, Shanghai 200433, China

Correspondence should be addressed to Ying Li; queenly@szu.edu.cn

Received 19 February 2017; Revised 5 May 2017; Accepted 24 August 2017; Published 22 October 2017

Academic Editor: Jan A. Jung

Copyright © 2017 Shuqing Chen et al. This is an open access article distributed under the Creative Commons Attribution License, which permits unrestricted use, distribution, and reproduction in any medium, provided the original work is properly cited.

By using optical heterodyne technique, we demonstrated the stable emission of sub-terahertz wave with the frequency ranging from 88 GHz to 101 GHz, which can operate as microwave source for nonlinear response measurement system. Mutual frequency beating of two well-separated sideband signals at a 0.1 THz photo-detector (PD) allows for the generation of sub-terahertz signal. Based on this approach, we have achieved the radiation of 0.1 THz wave with power up to 4 mW. By transmittance measurement, two-dimensional nanomaterial topological insulator (TI: Bi₂Te₃) shows saturable absorption behaviors with normalized modulation depth of 47% at 0.1 THz. Our results show that optical heterodyne technique could be developed as an effective microwave source generation for nonlinear measurement at sub-terahertz, even terahertz band.

1. Introduction

Sub-terahertz (sub-THz) and/or terahertz (THz) wave, usually defined in the range of 0.1–10 THz, has been extensively researched owing to its importance for high-frequency wireless communications, radar systems, high resolution imaging applications, and nonlinear measurement systems [1–7]. Especially for areas of measurement domain, the nonlinear characteristic of materials at sub-terahertz band is an influential perspective but was neglected for a long time. As the discovery of graphene, the first two-dimensional Dirac material, its unique band structure gives it ultra-broadband nonlinear response, which shows great prospect in various microwave and optical devices [8, 9]. To fully explore the nonlinear characteristic of these graphene-like materials and the effects of band structure, the sub-terahertz band which overlapped the microwave and terahertz has stimulated more and more researchers. However, how to investigate the nonlinear response at such high frequency, the high

quality and effective microwave source is a real challenge. And for nonlinear excitations, the higher microwave power is particularly important.

It is always highly encouraged to search for a robust method to generate sub-THz/THz wave with advantages of low phase noise, high power, and cost-effective. However, electrical signal generation of high-frequency microwave signals beyond 60 GHz is difficult to be obtained owing to the bandwidth limitations of electronic devices [10, 11]. To fulfill this expectation, photonic generation is considered as a promising technique [12–18]. As an alternative, optical generation, such as optical mode locking [19, 20], optical injection locking [21, 22], and external modulation [23–26], has been widely employed to generate THz wave. In particular, external modulation can provide excellent performance of stability and reliability. But, all those methods involve with very complicated structures and required extra photoelectric devices. By comparison, optical heterodyne technique is regarded as one of the most promising methods for photonics

generation of sub-THz/THz wave owing to its broad bandwidth, large tunability, efficiency, and cost-effectiveness [27–30]. On the other hand, dual-wavelength single-longitude-mode fiber ring laser is also demonstrated to generate high-frequency microwave [31, 32], but the output performance is not very stable and a complex dual-wavelength fiber ring laser needs to be designed. And difference frequency mixing of two collinearly propagating optical beams inside electro-optic crystals can be used to generate THz signals [33]. However, all-fiber format is lost and its application in miniaturization and integration is limited. By using the optical heterodyne technique, Tang et al. have realized the 100 GHz microwave generation and 2 m wireless transmission [34]. But, it is also necessary to further study the performance of the generated sub-terahertz, especially the radiation power, and stability shows importance in terahertz measurement, and its practical application in radio-over-fiber technique also should be paid more attention.

In this paper, we experimentally demonstrated an effective approach for sub-THz/THz wave generation by optical heterodyne technique. Two distributed feedback (DFB) lasers were employed to generate optical microwave signal, with frequency ranging from 88 GHz to 101 GHz. The output power directly radiated towards free space reached up to 4 mW. And it was found experimentally that fiber dispersion contributed much less effect to the radiation power. Based on this sub-terahertz source, the transmittance experiment system was constructed and used to study the nonlinear absorption characteristic of two-dimensional Dirac material (TI: Bi_2Te_3 nanoplatelets, TI NPs). The experiment results reveal the saturable absorption behaviors of the TI: Bi_2Te_3 , with normalized modulation depth of 47% and saturable intensity of $32 \mu\text{W}/\text{cm}^2$. To further evaluate the quality, the microwave source integrated radio-over-fiber (ROF) communication system was under our investigation. In the communication system, we realized 6 Gb/s OOK signal transmission over 5 m wireless link. This illustrated a central point that the generated microwave source has a better performance of quality and stability, which is very critical for the measurement system. These results showed that the generated sub-THz has sufficiently high power and excellent beam quality that may fit for nonlinear response measurement and wireless communication.

2. Experiment and Results

2.1. High Power 0.1 THz Sub-Terahertz Wave Generation. The principle of mm-wave generating and phase controlling is shown in Figure 1. The CW light wave, modulated RF signal through a Mach-Zehnder modulator (MZM), is used to generate optical sidebands for optical mm-wave carrier generating. Through an optical comb filter, two second-order optical sidebands are separated out, and the phase information is loaded to one of them by phase modulator. And then, the sideband carried with phase information is recombined with the optical mm-wave to realize the phase controlling of mm-wave. A photodetector (PD) is employed to detect the optical signal realizing mm-wave signal conversion [31].

The experimental setup of 0.1 THz wave generation is illustrated in Figure 1. Two individual continuous light beams came from the DFBs with wavelength fixed at 1546.082 nm and 1546.858 nm, respectively. Then, they were recombined and directed into a 50/50 optical coupler (OC), from which dual-wavelength lasing spectrum had been measured as shown in the insert of Figure 1. In the following, an optical attenuator was used to adjust the input optical power before the PD, which can convert the optical signals to the sub-THz microwave signal through the mutual frequency beating effect. The generated 0.1 THz wave was further amplified by a high-frequency electrical amplifier and radiated to free space by a horn antenna (gain: 25 dBi). Before detecting the 0.1 THz wave by the absolute THz power meter, a chopper was employed to modulate it with a fixed frequency of 30 MHz.

The stability of the generated sub-THz wave has been studied. At an input optical power of 3.6 mW, the radiated power of sub-THz wave was measured to be about 3.2 mW. By repeatedly monitoring the radiation power, we note that the power was almost kept constant over 10 minutes at room temperature, as shown in Figure 2, indicating the high stability of the radiation output. If one input wavelength was fixed at 1546.858 nm, sub-THz radiation at different frequencies can be produced as the other wavelength continuously changed. Experimentally, the output frequencies of the wave can be tuned from 88 GHz to 101 GHz, while the input optical power was kept at 3.6 mW. Owing to the bandwidth limitation of the amplifier, we note that the operating frequency has a dynamic range and the optimal operating frequency located from 96 GHz to 98 GHz, as shown in Figure 3(a). Particularly, the microwave power decreased dramatically for the frequency beyond 99 GHz, as the input optical power holding constant.

Figure 3(b) demonstrates the relationship of input optical power and radiation microwave power at different situations. Under the weak power regime, the output power almost synchronously increased with the increase of the input power. However, once the input power exceeds 6 mW, the output power becomes saturated. In order to study the role of the fiber dispersion on the microwave generation, transmission experiments through back to back (BTB), 10 km DSF, 10 km single mode fiber (SMF), and 20 km SMF were under investigation. However, as noted in Figure 3(b), there is no significant difference, indicating that the real impact of fiber dispersion is limited.

2.2. Nonlinear Response Measurement of TI at Sub-Terahertz Band. A quality and stable microwave source is essential for nonlinear response measurement of variety nonlinear media, especially for sub-terahertz which overlapped the microwave and terahertz band. The microwave generated by optical heterodyne technique has many great assets in nonlinear response measurement, such as broadband tunability of wavelength and high output power. To verify its application in nonlinear response measurement, we constructed the measurement system like that in [8, 26] to investigate the nonlinear absorption property of the TI (TI: Bi_2Te_3 NPs transferred onto the square quartz glass) [26].

Here, the diethylene glycol (DEG) mediated polyol method was introduced into the composite few-layer TI:

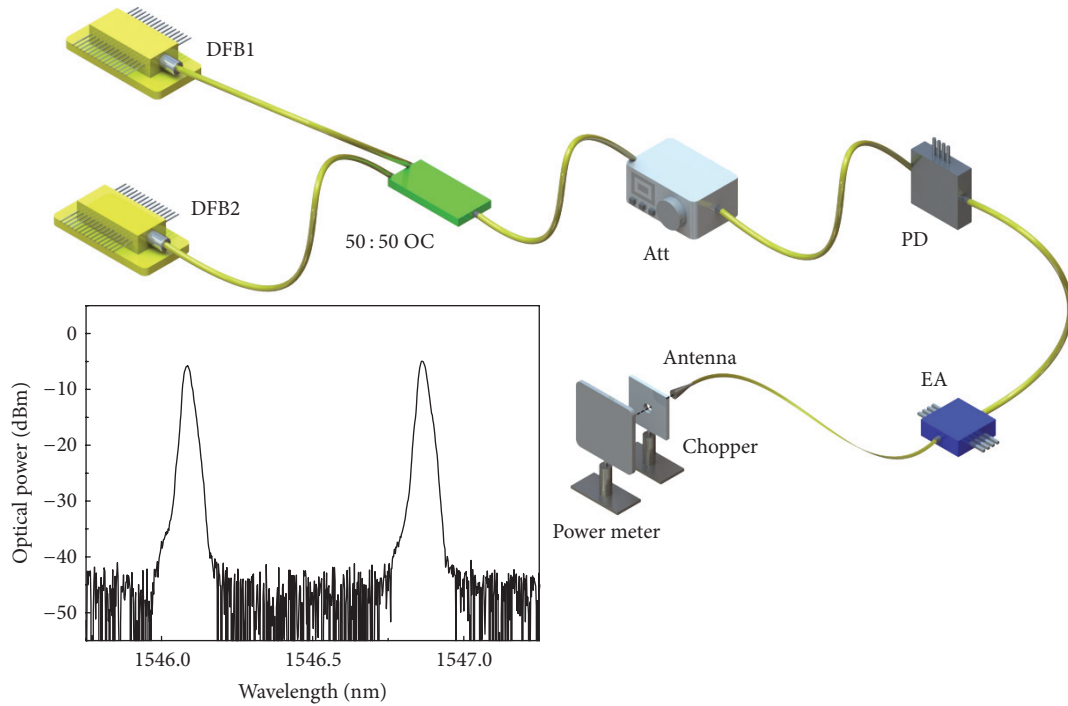


FIGURE 1: Schematic of the 0.1 THz microwave generation system, and the insert is the optical spectrum of the source for optical heterodyne.

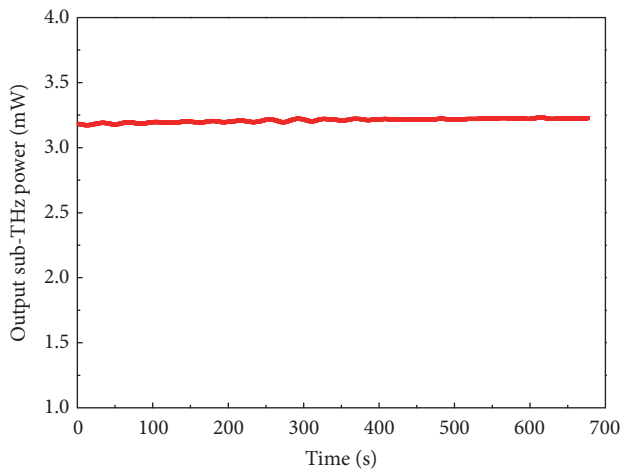


FIGURE 2: Power radiated from the antenna takes over 10 minutes with input optical power at 3.6 mW.

Bi_2Te_3 NPs [35]. The physical photo of TI: Bi_2Te_3 ethanol solution is shown in Figure 4(a). Figure 4(b) shows the transmission electron microscopy (TEM) images; it can be clearly seen that TI exhibits symmetric hexagonal morphology, which indicates relative high stability [26]. Atomic force microscope (AFM) images are shown in Figure 4(c), it further corroborated the symmetric hexagonal morphology of prepared TI NPs, and the sample thickness is measured to be an average of 55 nm.

The experimental setup shows in Figure 5(a) that, with the attenuator adjusting, the microwave power can be changed

from $20 \mu\text{W}$ to 4 mW. The chopper has the aperture diameter of 15 mm, which shows that the maximum output intensity can reach $2.27 \text{ mW}/\text{cm}^2$. This is a sufficient approach for most measurement. The corresponding transmittance curve at this sub-terahertz band is shown in Figure 5(b); as can be seen from the diagram, the transmittance goes to a steady value with the input intensity increasing from 20 to $160 \mu\text{W}/\text{cm}^2$. After fitting with formula, $T(I) = 1 - \Delta T * \exp(-I/T_{\text{sat}}) - T_{\text{ns}}$, where $T(I)$ is the transmission, ΔT is the modulation depth, I is the input intensity, I_{sat} is the saturation power intensity, and T_{ns} is the nonsaturable absorbance, we obtained the corresponding saturable absorption parameters [36]. The modulation depth and saturation intensity of TI are 47% and $32 \mu\text{W}/\text{cm}^2$, respectively. The results coincide with the results reported in [26], which indicated that the sub-terahertz result from this approach is of high quality and appropriate for nonlinear response measurement.

As schematically shown in Figure 6(a), the structure of TI: Bi_2Te_3 can be considered as layers made up of 5 atom thick Te-Bi-Te-Bi-Te covalently bound sheets coupled together by much weaker van der Waals forces [35]. And its band structure is shown in Figure 6(b); like graphene, they are all direct-band-gap material, which is conducive to exciting electronic transitions. Except for the difference that TI: Bi_2Te_3 has insulating bulk state, it also possesses the gapless metallic surface state like graphene. This raises an interesting issue about what role did the insulating bulk state and metallic surface state play in the nonlinear response. As the TI: Bi_2Te_3 was on exposure to light or microwave, the electrons in the valence band can be excited to conduction band and occupied the lowest energy states following

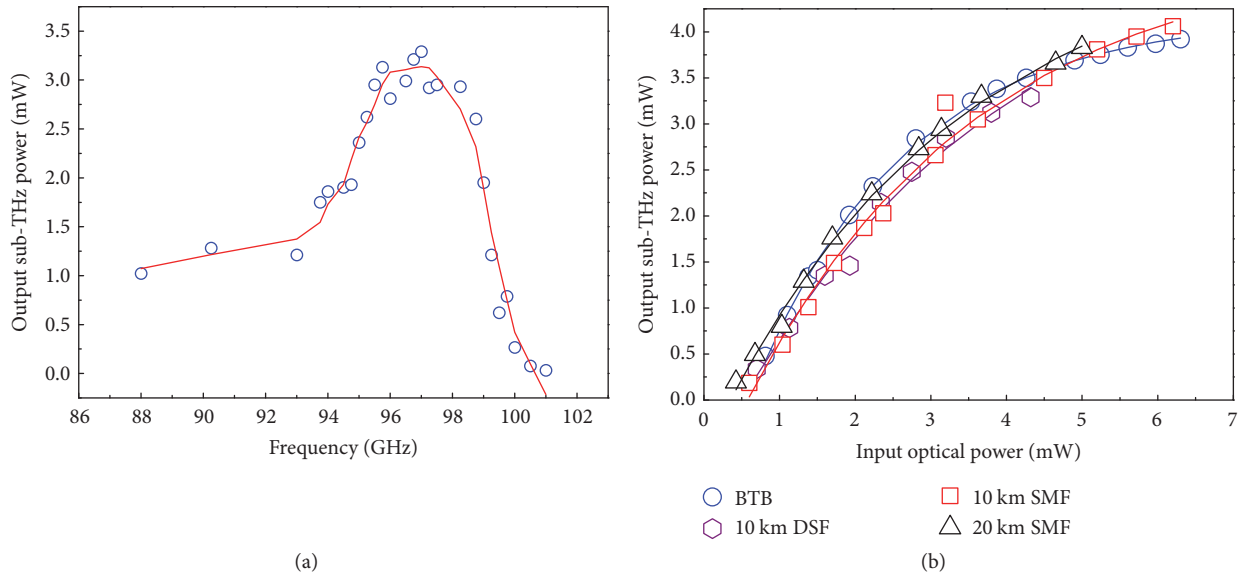
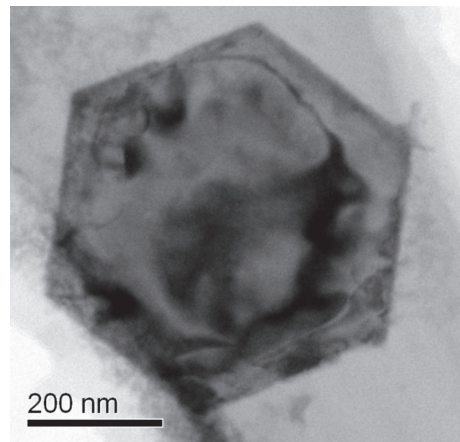


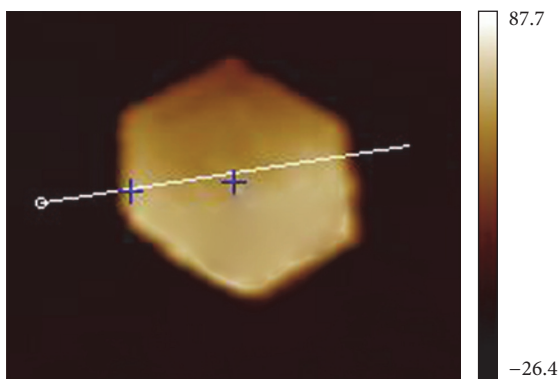
FIGURE 3: Dependence of sub-THz wave radiation power (a) on different wavelength spacing with input optical power at 3.6 mW and (b) on PD input optical power with BTB, 10 km DSE, 10 km SMF, and 20 km SMF.



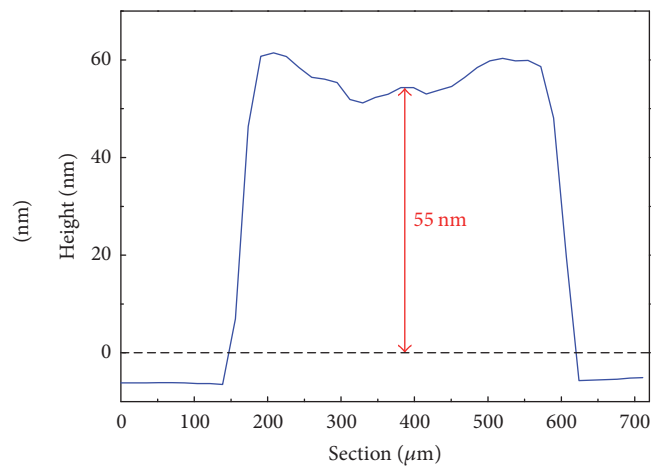
(a)



(b)



(c)



(d)

FIGURE 4: (a) The physical photo of TI: Bi_2Te_3 ethanol solution, (b) TEM images, (c) AFM images, and height profiles of the as-prepared few-layer TI: Bi_2Te_3 NPs.

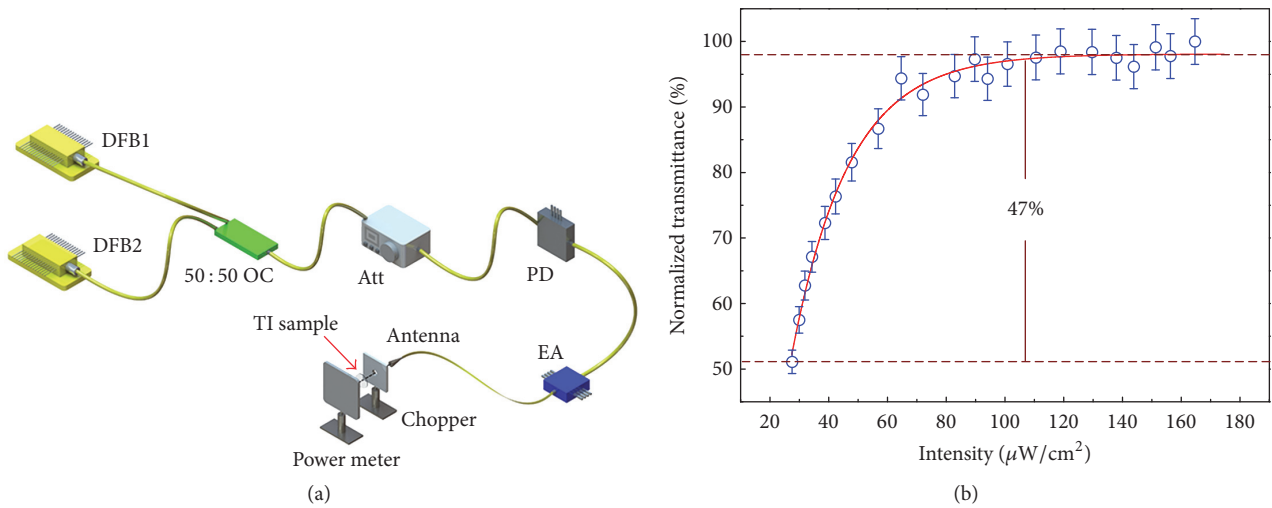


FIGURE 5: (a) Experimental setup for nonlinear response measurement system and (b) the measured normalized transmittance curve of TI: Bi_2Te_3 at sub-terahertz band.

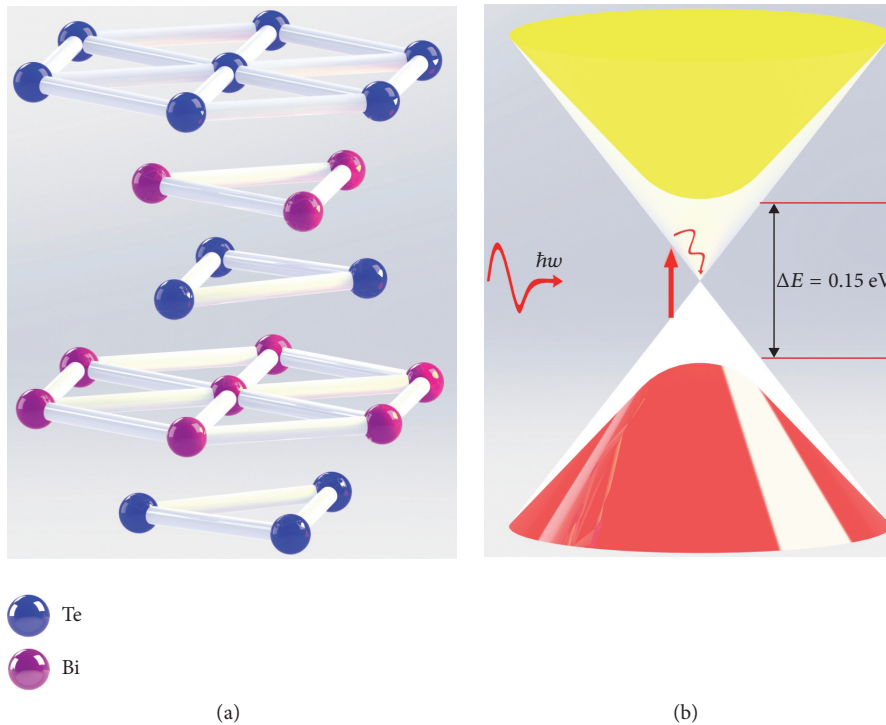


FIGURE 6: (a) The atomic structure and (b) the band structure of TI: Bi_2Te_3 .

the Pauli exclusion principle. With the incident intensity increasing, the generated carriers fill the valence bands and prevent the further excitation of electrons at valence band leading to saturated. However, the insulating band-gap value is about 0.15 eV (at the bulk state of TI: Bi_2Te_3), indicating that the single photon energy less than 0.15 eV is difficult to excite the electron leaps into conduction band at the bulk state. This saturable absorption process at sub-terahertz band confirmed that the surface metallic state is responsible for the saturable absorption at microwave band, where the

single photon energy is far below 0.15 eV. All this suggests that the microwave/terahertz band with low photo energy may has important significance in more detailed study of the linear/nonlinear response of material. And the effective microwave source is a guarantee of the linear/nonlinear measurement.

2.3. Radio-over-Fiber Communication System with 0.1 THz Sub-Terahertz Wave. To further evaluate the quality of the generated sub-terahertz wave, it was used to carry digital

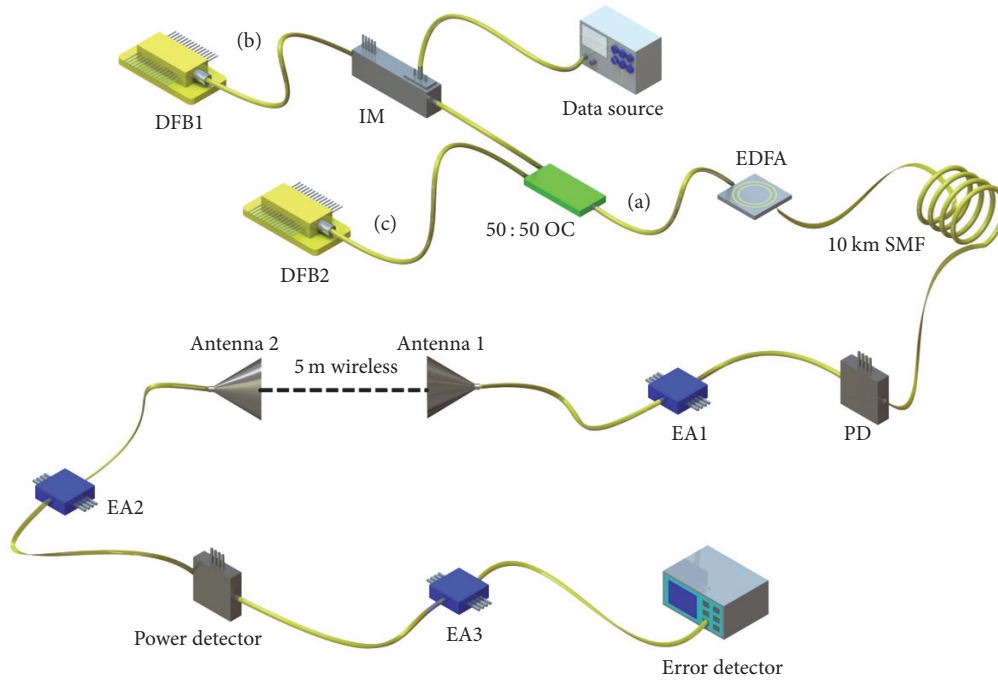


FIGURE 7: Experimental setup of radio-over-fiber system with 0.1 THz carrier.

signal. Figure 7 shows the experimental setup of 0.1 THz radio-over-fiber system with 5 m delivery. The continuous-wave (CW) at 1546.082 nm and 1546.858 nm with ~ 6 dBm output power emitted from DFBs functions as the optical source, with the corresponding optical spectrum shown in Figures 8(b) and 8(c), respectively. This suggests that the frequency spacing between DFB1 and DFB2 is 97 GHz. And the CW light wave at 1546.082 nm from DFB1 was modulated by intensity modulator (IM). The 2 Gb/s downlink baseband signals with a pseudorandom binary sequence (PRBS) length of 231-1 were used to drive the IM. Together with the output of DFB2, both of them acted as input of the 50/50 OC, with the optical spectrum shown in Figure 8(a). After 10 km SMF-28 transmission, in order to obtain the optimal output, which requires that the input power into the PD cannot be too low, a following erbium-doped fiber amplifier (EDFA) was utilized to compensate the attenuation of the fiber. Then a 0.1 THz PD was employed to detect the optical signal and therefore allows for the conversion of the 0.1 THz signals. The signals were subsequently amplified by a low-noise electrical amplifier (EA1). And then a W-band antenna with a gain of 25 dBi was used to radiate the 0.1 THz wave with 2 Gb/s OOK signals loaded.

After 5 m wireless delivery, the data were received by another antenna with identical parameters of antenna 1 and were then amplified by EA2. Then, a power detector was used to downconvert the data into the baseband. After a broadband EA3, signals were launched into an error detector to measure the BER index.

The BER performances of the data signals under different conditions are shown in Figure 6. The insert (a) of Figure 9 is the eye diagram after only 5 m wireless transmission, while

the insert (b) shows the eye diagram after 10 km SMF-28 and 5 m wireless transmission. The result shows that the presence of fiber in the system can significantly distort the eye diagram, which is caused by fiber dispersion [23]. And the power penalty was measured to be 3 dB, as shown in Figure 9.

When the data were loaded at different rates, the corresponding eye diagrams after 5 m wireless transmission were also measured. As shown in Figure 10, Figures 10(a)–10(d) are the eye diagram as data rate sets at 3, 4, 5, and 6 Gb/s, respectively. The results show that once the loading data rate was set beyond 5 Gb/s, significant distortion can occur. This is because of bandwidth limitation of the electrical amplifiers. By upgrading the amplifiers, the output power and transmission distance can be scaled up.

3. Conclusion

In conclusion, we had experimentally demonstrated a robust method for generating 0.1 THz signal based on optical heterodyne technique, together with its application for nonlinear response measurement. The frequency of radiation microwave was confined at the range of 0.1 THz due to the limitation of electrical amplifier. Further long distance transmission experiments indicate that chromatic dispersion shows limited effect on the radiation power, and 6 Gb/s OOK signals were successfully propagated across 5 m wireless carried by the 0.1 THz wave indicating the generated sub-terahertz wave is of high quality. Under the 0.1 THz sub-terahertz wave excitation, TI shows saturable absorption behaviors which further corroborated the contribution of the metallic surface state of TI: Bi_2Te_3 in nonlinear absorption response. Our result constitutes a major step forward the

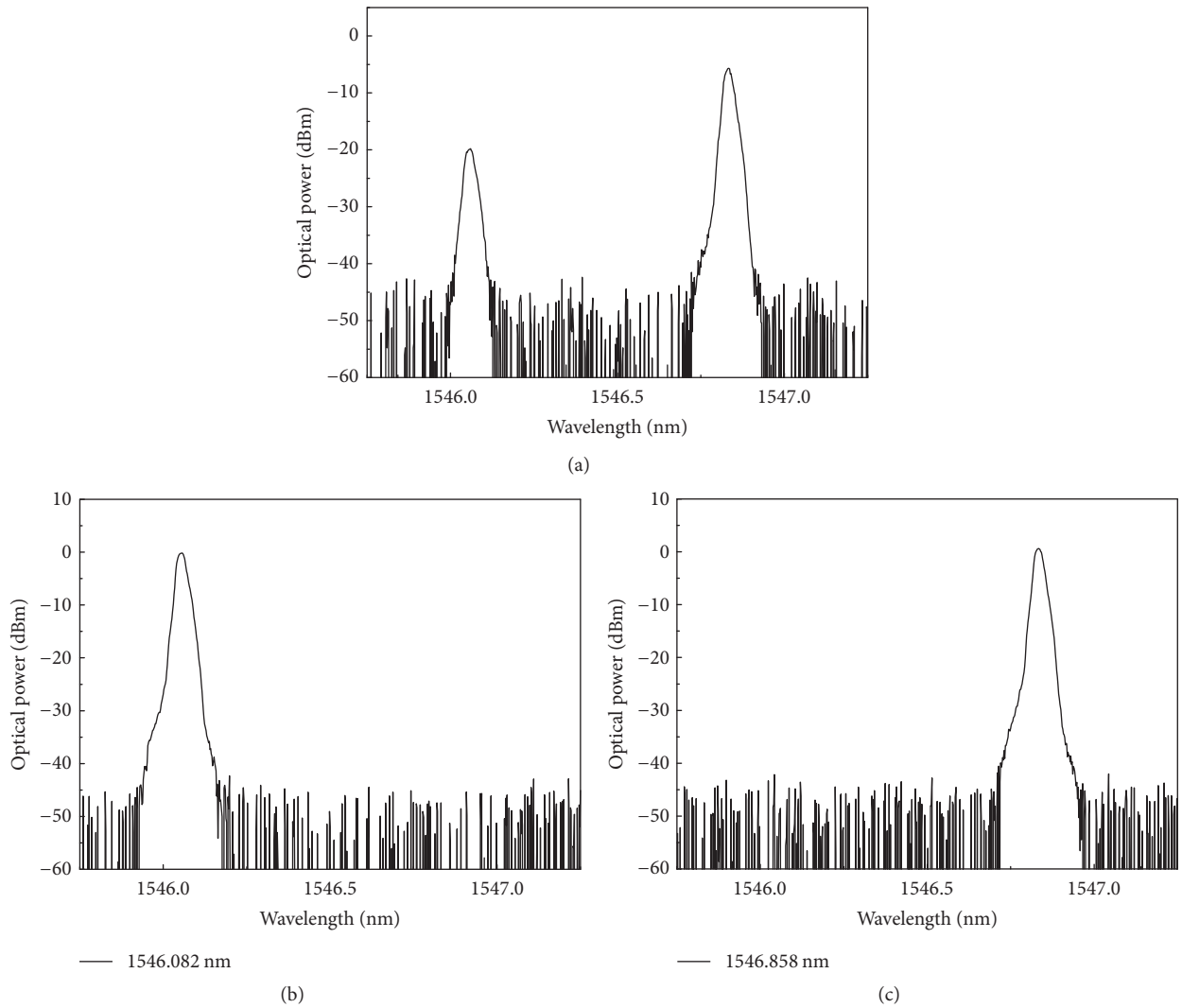


FIGURE 8: Optical spectrum (a) after OC, (b) after DFB1, and (c) after DFB2, as shown in Figure 7.

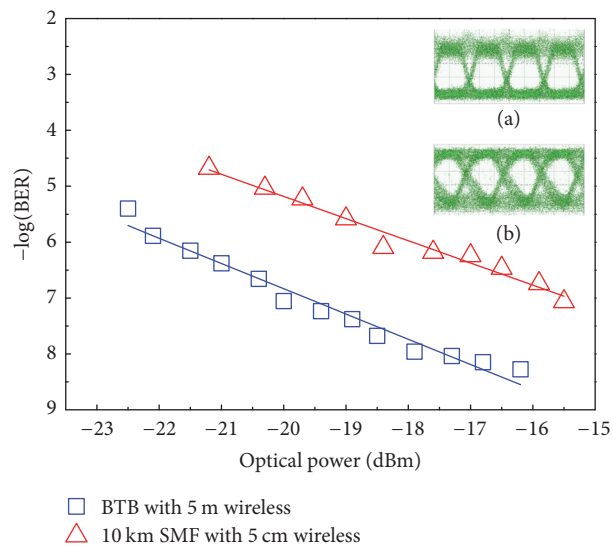


FIGURE 9: The measured BER curves of 2 Gb/s signal, insert eye diagrams of signals (a) after 5 m wireless transmission without fiber, and (b) after 10 km fiber and 5 m wireless.

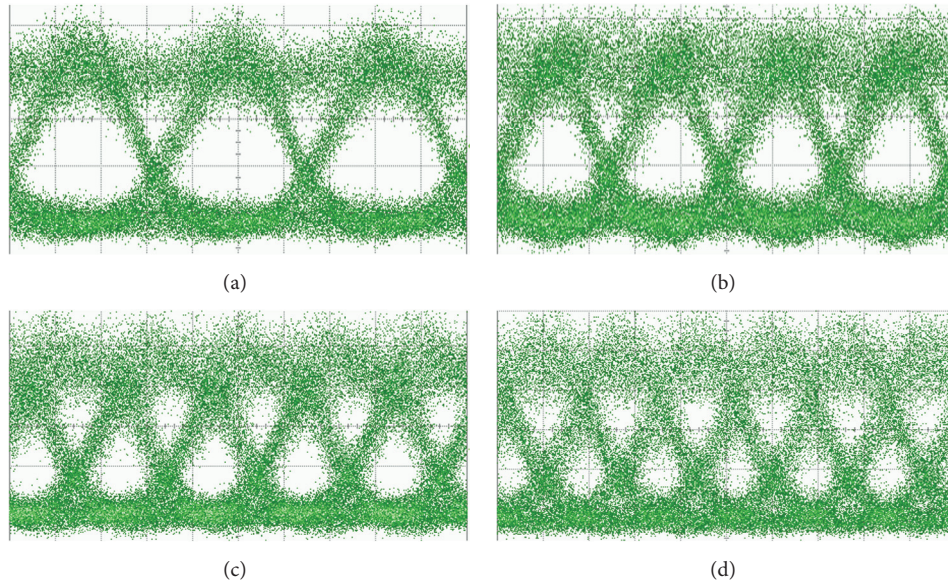


FIGURE 10: Eye diagram after 5 m wireless transmission when data rates are (a) 3, (b) 4, (c) 5, and (d) 6 Gb/s.

development of photonic generation of high-power sub-terahertz and terahertz source, which shows tremendous potential in measurement domain.

Conflicts of Interest

The authors declare that they have no conflicts of interest.

Acknowledgments

This work is partially supported by the program of Fundamental Research of Shenzhen Science and Technology Plan (Grants nos. JCYJ20160422152152634, JCYJ2016032814464, and JCYJ20150324141711651), the National Science Foundation of China (Grants nos. 61575127 and 61505122), the Project Supported by Guangdong Natural Science Foundation (Grant nos. 2016A030310065 and 2014A030310279), the Natural Science Foundation of SZU (Grant nos. 000059 and 2016031), Science and Technology Planning Project of Guangdong Province (2016B050501005), and the Natural Science Foundation Guangdong Education Department (Grants nos. 2015KTSCX124 and 2015KQNCX146).

References

- [1] T. Nagatsuma, "Generating Millimeter and Terahertz Waves," *IEEE Microwave Magazine*, vol. 10, no. 4, pp. 64–74, 2009.
- [2] M. Tonouchi, "Cutting-edge terahertz technology," *Nature Photonics*, vol. 1, no. 2, pp. 97–105, 2007.
- [3] I. Duling and D. Zimdars, "Terahertz imaging: Revealing hidden defects," *Nature Photonics*, vol. 3, no. 11, pp. 630–632, 2009.
- [4] H.-J. Song and T. Nagatsuma, "Present and future of terahertz communications," *IEEE Transactions on Terahertz Science and Technology*, vol. 1, no. 1, pp. 256–263, 2011.
- [5] S. J. B. Yoo, R. P. Scott, D. J. Geisler, N. K. Fontaine, and F. M. Soares, "Terahertz information and signal processing by RF-photonics," *IEEE Transactions on Terahertz Science and Technology*, vol. 2, no. 2, pp. 167–176, 2012.
- [6] A. Hirata, M. Harada, and T. Nagatsuma, "120-GHz Wireless Link Using Photonic Techniques for Generation, Modulation, and Emission of Millimeter-Wave Signals," *Journal of Lightwave Technology*, vol. 21, no. 10, pp. 2145–2153, 2003.
- [7] D. M. Mittleman, R. H. Jacobsen, and M. C. Nuss, "T-ray imaging," *IEEE Journal on Selected Topics in Quantum Electronics*, vol. 2, no. 3, pp. 679–692, 1996.
- [8] Z. Zheng, C. Zhao, S. Lu et al., "Microwave and optical saturable absorption in graphene," *Optics Express*, vol. 20, no. 21, pp. 23201–23214, 2012.
- [9] V. P. Gusynin, S. G. Sharapov, and J. P. Carbotte, "Unusual microwave response of dirac quasiparticles in graphene," *Physical Review Letters*, vol. 96, no. 25, Article ID 256802, 2006.
- [10] H.-W. Hübers, "Terahertz heterodyne receivers," *IEEE Journal on Selected Topics in Quantum Electronics*, vol. 14, no. 2, pp. 378–391, 2008.
- [11] H.-J. Song, N. Shimizu, and T. Nagatsuma, "Generation of two-mode optical signals with broadband frequency tunability and low spurious signal level," *Optics Express*, vol. 15, no. 22, pp. 14901–14906, 2007.
- [12] E. Rouvalis, M. J. Fice, C. C. Renaud, and A. J. Seeds, "Millimeter-wave optoelectronic mixers based on uni-traveling carrier photodiodes," *IEEE Transactions on Microwave Theory and Techniques*, vol. 60, no. 3, pp. 686–691, 2012.
- [13] H. Ito, T. Furuta, F. Nakajima, K. Yoshino, and T. Ishibashi, "Photonic generation of continuous THz wave using uni-traveling-carrier photodiode," *Journal of Lightwave Technology*, vol. 23, no. 12, pp. 4016–4021, 2005.
- [14] D. Saeedkia and S. Safavi-Naeini, "Terahertz photonics: Optoelectronic techniques for generation and detection of Terahertz waves," *Journal of Lightwave Technology*, vol. 26, no. 15, pp. 2409–2423, 2008.

- [15] W. Liu, M. Wang, and J. Yao, "Tunable microwave and sub-terahertz generation based on frequency quadrupling using a single polarization modulator," *Journal of Lightwave Technology*, vol. 31, no. 10, Article ID 6487368, pp. 1636–1644, 2013.
- [16] D. Stanze, A. Deninger, A. Roggenbuck, S. Schindler, M. Schlak, and B. Sartorius, "Compact cw terahertz spectrometer pumped at 1.5 μm wavelength," *Journal of Infrared, Millimeter, and Terahertz Waves*, vol. 32, no. 2, pp. 225–232, 2011.
- [17] J. Ye, L. Yan, Z. Chen et al., "Photonic generation of microwave phase-coded signals based on frequency-to-time conversion," *IEEE Photonics Technology Letters*, vol. 24, no. 17, pp. 1527–1529, 2012.
- [18] J. Ye, L. Yan, W. Pan et al., "Photonic generation of triangular-shaped pulses based on frequency-to-time conversion," *Optics Letters*, vol. 36, no. 8, pp. 1458–1460, 2011.
- [19] Z. Deng and J. Yao, "Photonic generation of microwave signal using a rational harmonic mode-locked fiber ring laser," *IEEE Transactions on Microwave Theory and Techniques*, vol. 54, no. 2, pp. 763–767, 2006.
- [20] A. C. Bordonalli, B. Cai, A. J. Seeds, and P. J. Williams, "Generation of microwave signals by active mode locking in a gain bandwidth restricted laser structure," *IEEE Photonics Technology Letters*, vol. 8, no. 1, pp. 151–153, 1996.
- [21] L. Goldberg, H. F. Taylor, J. F. Weller, and D. M. Bloom, "Microwave signal generation with injection-locked laser diodes," *Electronics Letters*, vol. 19, no. 13, pp. 491–493, 1983.
- [22] L. Goldberg, A. M. Yurek, H. F. Taylor, and J. F. Weller, "35 GHz microwave signal generation with an injection-locked laser diode," *Electronics Letters*, vol. 21, no. 18, pp. 814–815, 1985.
- [23] J. Yu, Z. Jia, L. Yi, Y. Su, G.-K. Chang, and T. Wang, "Optical millimeter-wave generation or up-conversion using external modulators," *IEEE Photonics Technology Letters*, vol. 18, no. 1, pp. 265–267, 2006.
- [24] S. Pan and J. Yao, "Tunable subterahertz wave generation based on photonic frequency sextupling using a polarization modulator and a wavelength-fixed notch filter," *IEEE Transactions on Microwave Theory and Techniques*, vol. 58, no. 7, pp. 1967–1975, 2010.
- [25] G. Qi, J. Yao, J. Seregelyi, S. Paquet, and C. B elisle, "Optical generation and distribution of continuously tunable millimeter-wave signals using an optical phase modulator," *Journal of Lightwave Technology*, vol. 23, no. 9, pp. 2687–2695, 2005.
- [26] S. Chen, C. Zhao, Y. Li et al., "Broadband optical and microwave nonlinear response in topological insulator," *Optical Materials Express*, vol. 4, no. 4, pp. 587–596, 2014.
- [27] F. Fan and M. Dagenais, "Optical generation of a megahertz-linewidth microwave signal using semiconductor lasers and a discriminator-aided phase-locked loop," *IEEE Transactions on Microwave Theory and Techniques*, vol. 45, no. 8, pp. 1296–1300.
- [28] A. Hirata, M. Harada, K. Sato, and T. Nagatsuma, "Low-Cost Millimeter-Wave Photonic Techniques for Gigabit/s Wireless Link," *IEICE Transactions on Electronics*, vol. E86-C, no. 7, pp. 1123–1128, 2003.
- [29] D. Wake, C. R. Lima, and P. A. Davies, "Optical generation of millimeter-wave signals for fiber-radio systems using a dual-mode DFB semiconductor laser," *IEEE Transactions on Microwave Theory and Techniques*, vol. 43, no. 9, pp. 2270–2276, 1995.
- [30] H.-J. Song, N. Shimizu, T. Furuta, K. Suizu, H. Ito, and T. Nagatsuma, "Broadband-frequency-tunable sub-terahertz wave generation using an optical comb, AWGs, optical switches, and a uni-traveling carrier photodiode for spectroscopic applications," *Journal of Lightwave Technology*, vol. 26, no. 15, pp. 2521–2530, 2008.
- [31] X. Chen, Z. Deng, and J. Yao, "Photonic generation of microwave signal using a dual-wavelength single-longitudinal-mode fiber ring laser," *IEEE Transactions on Microwave Theory and Techniques*, vol. 54, no. 2, pp. 804–809, 2006.
- [32] D. Chen, H. Fu, W. Liu, Y. Wei, and S. He, "Dual-wavelength single-longitudinal-mode erbium-doped fibre laser based on fibre Bragg grating pair and its application in microwave signal generation," *Electronics Letters*, vol. 44, no. 7, pp. 459–461, 2008.
- [33] S. Hoffmann and M. R. Hofmann, "Generation of Terahertz radiation with two color semiconductor lasers," *Laser and Photonics Reviews*, vol. 1, no. 1, pp. 44–56, 2007.
- [34] C. Tang, R. Li, Y. Shao et al., "Experimental demonstration for 40-km fiber and 2-m wireless transmission of 4-Gb/s OOK signals at 100-GHz carrier," *Chinese Optics Letters*, vol. 11, no. 2, Article ID 020608, 2013.
- [35] L. Ren, X. Qi, Y. Liu et al., "Large-scale production of ultrathin topological insulator bismuth telluride nanosheets by a hydrothermal intercalation and exfoliation route," *Journal of Materials Chemistry*, vol. 22, no. 11, pp. 4921–4926, 2012.
- [36] S. Lu, C. Zhao, Y. Zou et al., "Third order nonlinear optical property of Bi₂Se₃," *Optics Express*, vol. 21, no. 2, pp. 2072–2082, 2013.

Research Article

Over 19 W Single-Mode 1545 nm Er,Yb Codoped All-Fiber Laser

Jiadong Wu,^{1,2} Chunxiang Zhang,³ Jun Liu,^{1,2} Ting Zhao,⁴ Weichao Yao,¹ Pinghua Tang,³ Le Zhang,^{1,5} and Hao Chen^{1,5}

¹Jiangsu Key Laboratory of Advanced Laser Materials and Devices, School of Physics and Electronic Engineering, Jiangsu Normal University, Xuzhou, Jiangsu 221116, China

²International Collaborative Laboratory of 2D Materials for Optoelectronic Science and Technology, Key Laboratory of Optoelectronic Devices and Systems of Ministry of Education and Guangdong Province, College of Optoelectronic Engineering, Shenzhen University, Shenzhen 518060, China

³Laboratory for Micro-/Nano-Optoelectronic Devices of Ministry of Education, IFSA Collaborative Innovation Center, School of Physics and Electronics, Hunan University, Changsha 410082, China

⁴School of Electronic Engineering, Nanjing Xiaozhuang University, Nanjing, Jiangsu 211171, China

⁵Jiangsu Collaborative Innovation Center of Advanced Laser Technology and Emerging Industry, Jiangsu Normal University, Xuzhou 221116, China

Correspondence should be addressed to Jun Liu; liuj1987@szu.edu.cn and Hao Chen; chenhao@jsnu.edu.cn

Received 27 June 2017; Revised 15 August 2017; Accepted 24 August 2017; Published 4 October 2017

Academic Editor: Jörg Fink

Copyright © 2017 Jiadong Wu et al. This is an open access article distributed under the Creative Commons Attribution License, which permits unrestricted use, distribution, and reproduction in any medium, provided the original work is properly cited.

We report a high-power cladding-pumped Er,Yb codoped all-fiber laser with truly single transverse mode output. The fiber laser is designed to operate at 1545 nm by the use of a pair of fiber Bragg gratings (FBGs) to lock and narrow the output spectrum, which can be very useful in generating the eye-safe ~1650 nm laser emission through the Stimulated Raman Scattering (SRS) in silica fibers that is of interest in many applications. Two pieces of standard single-mode fibers are inserted into the laser cavity and output port to guarantee the truly single-mode output as well as good compatibility with other standard fiber components. We have obtained a maximum output power of 19.2 W at 1544.68 nm with a FWHM spectral width of 0.08 nm, corresponding to an average overall slope efficiency of 31.9% with respect to the launched pump power. This is, to the best of our knowledge, the highest output power reported from simple all-fiber single-mode Er,Yb codoped laser oscillator architecture.

1. Introduction

High-power fiber lasers in the eye-safe wavelength regime around 1.5–1.6 μm have attracted considerable attention in various applications such as spectroscopy, remote sensing, range finding, and free-space and satellite communications. Cladding-pumped Er,Yb codoped fiber laser systems provide a common approach to produce high-power laser emissions in this wavelength region owing to the commercially available efficient double clad gain fiber and high-power InGaAs laser diodes at ~980 nm as a pump source [1–6]. In 2007, Jeong et al. achieved 297 W of output power at 1.567 μm in an Er,Yb codoped fiber laser, which is the highest output power achieved with the Er,Yb codoped fibers until now [1]. However, the vast majority of high-power Er,Yb codoped laser systems reported so far were implemented with large mode

area (LMA) gain fibers supporting tens or even hundreds of modes to mitigate the harmful nonlinear effects, which, unfortunately, degrade the output laser beam quality [2–4]. In addition, many high-power laser configurations incorporate several free-space optical components, increasing the complexity of the system and thus cost of maintenance. Nevertheless, for many applications in the eye-safe wavelength range, the requirement for high output power is also accompanied by the need of good beam quality and high efficiency resulting from simple laser structures. All-fiber geometries without free-space optics can offer alignment-free, efficient, compact, and reliable laser architecture. Single-mode all-fiber Er,Yb codoped laser systems have naturally become an attractive candidate for achieving high output power level while maintaining good laser beam quality to meet the requirement for particular applications. Nowadays, more than 10 W output

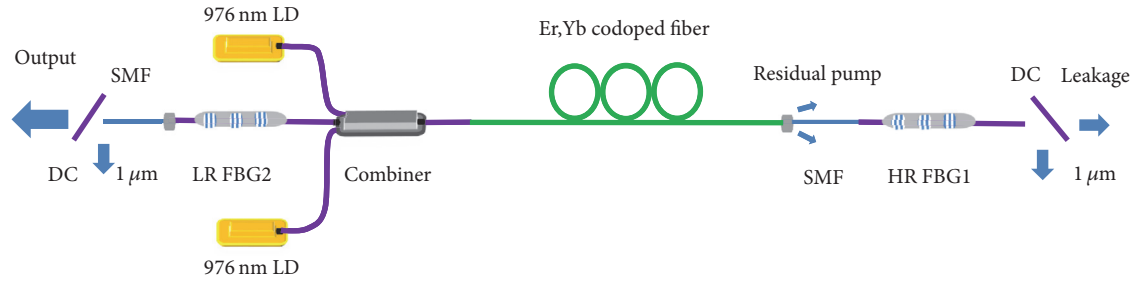


FIGURE 1: Experimental schematic of the single-mode all-fiber Er,Yb codoped laser. DC: dichroic mirror; SMF: standard single-mode fiber; FBG: fiber Bragg grating.

powers of single-mode laser emissions at $\sim 1.5 \mu\text{m}$ in the Er,Yb codoped laser systems have been achieved based on the more complex master oscillator power amplifier (MOPA) configurations [7, 8], while the extremely simple all-fiber Er,Yb codoped fiber laser oscillators still remain of a limited output power level of several watts [9–11].

In this paper, we use a simple and compact cavity design with two pieces of standard single-mode fiber incorporated into the laser resonator and the output port, respectively, and demonstrate a truly single-mode high-power Er,Yb codoped all-fiber laser based on a slightly multimode gain fiber. The operating wavelength of the fiber laser is locked at 1545 nm, which corresponds to the first-order Stokes wavelength of 1658 nm that can be used to precisely generate the dual mid-IR laser emissions of 2.7 μm and 4.3 μm through the nonlinear optical parametric frequency conversion [12–14]. A maximum overall output power of 19.2 W is obtained at 1544.68 nm with a FWHM spectral width of 0.08 nm and an overall slope efficiency of 31.9%, limited only by the available pump power. To the best of our knowledge, this is so far the highest output power reported from all-fiber single-mode Er,Yb codoped laser oscillators.

2. Experiment

The experimental schematic of the single-mode all-fiber Er,Yb codoped fiber laser is shown in Figure 1. The gain medium was a 3 m long Er,Yb codoped multimode double clad fiber (Nufern, MM-EYDF-12/130) with a nominal cladding-pump absorption of 3.10 dB/m at 915 nm, which had a core of 12 μm diameter and ~ 0.2 NA, and a pure silica inner-cladding of 130 μm diameter and ~ 0.46 NA covered with a low refractive index Acrylate outcladding also as protective coating. The gain fiber had a V number (cut-off frequency or normalized frequency) of 4.8, suggesting the number of laser modes that the gain fiber can support is around 11. Therefore, a piece of standard single-mode-fiber was inserted as a spatial filter into the new laser cavity with the output port made of another piece of standard single-mode fiber, in order to guarantee truly single-mode laser output and at the same time eliminate the residual pump in the cladding and other unwanted laser modes coupled into the cladding by using a high-index gel. The splicing between the unmatched fibers was carefully carried out by a specialty splicer (Fujikura,

FSM-100P+) with splicing loss of below 0.2 dB. The heat load yielded from quantum defect over the gain fiber was dissipated by simple fan-cooling.

The lasing feedback was provided by a pair of FBGs written in a compatible single-mode double clad passive fiber (Nufern, GDF-1550). FBG1 is highly reflective with a peak reflectivity of 99% and spectral bandwidth of 0.5 nm at 1544.5 nm. FBG2 is a 10% low-reflection output coupler with the center wavelength of 1544.6 nm and bandwidth of 0.7 nm, as shown in Figure 2. Due to limited effective reflectivity and slight shift of center wavelength and bandwidth for the two FBGs, as well as possible laser spectral broadening in the high-power operation, some power leakage may occur through the high-reflection FBG1 end. Thus, we also monitored the possible power leakage and corresponding spectrum from the free end facet of FBG1. Both output end facets of the fiber laser were angle-cleaved at $\sim 8^\circ$ to suppress the impact of Fresnel reflections from the uncoated fiber facets on the laser stability as well as the corresponding broadband feedback and then to reduce the $\sim 1 \mu\text{m}$ parasitic lasing resulting from transitions of some Yb ions excluded from the energy transfer process between Yb and Er ions. Two 45° dichroic mirrors with high-reflection at the laser wavelength and high-transmission in the $\sim 1 \mu\text{m}$ wavelength band were inserted into the output path to steer the laser beam from the possible $\sim 1 \mu\text{m}$ parasitic laser for measurement. Two commercial fiber-coupled 35 W wavelength stabilized 976 nm laser diodes were served as the pump source, the output ports of which were directly spliced to a $(2 + 1) \times 1$ pump combiner to cladding-pump the gain fiber in the backward pumping regime. Both pump laser diodes were spectrally narrowed and locked at 976 nm by a volume Bragg grating with a 3 dB spectral width of 0.5 nm to match the absorption peak of the Er,Yb codoped fiber. The spectral characteristics of the laser output were recorded using an optical spectrum analyzer (AQ6370C, Yokogawa).

3. Results and Discussion

The lasing characteristics of the single-mode all-fiber Er,Yb codoped laser were evaluated. Figure 3 shows the output powers from the single-mode fiber output end as a function of the launched pump power. The laser reached threshold at a launched pump power of ~ 1 W and generated an output

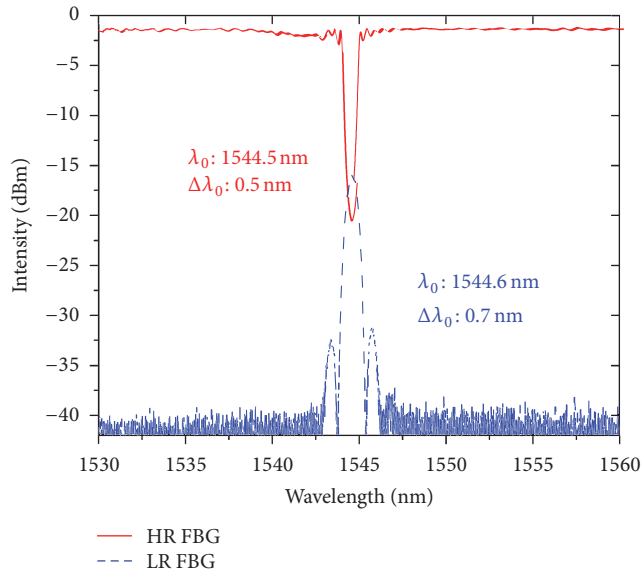


FIGURE 2: Measured transmission spectrum and reflection spectrum of the high-reflection (HR) FBG (red line) and low-reflection (LR) FBG (blue dash), respectively.

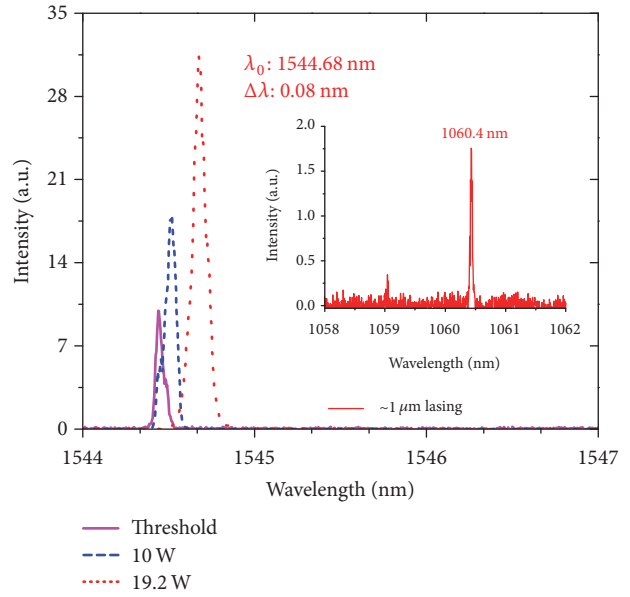


FIGURE 4: Laser output spectrum from standard single-mode fiber end and spectrum of the leaked laser from the high-reflection FBG1 end in comparison. Inset: measured spectrum of $\sim 1 \mu\text{m}$ parasitic lasing.

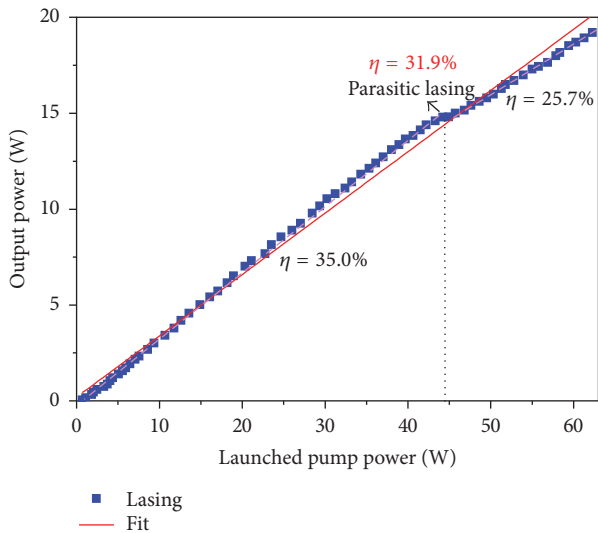


FIGURE 3: Laser output powers as a function of the launched pump power.

power of 19.2 W for the maximum launched pump power of 62.3 W, corresponding to an average slope efficiency of 31.9% with respect to the launched pump power. The output laser powers showed a linear dependence with the launched pump power over the whole pump range. The output powers remained quite stable during the whole measurement. However, parasitic lasing of Yb at 1060.4 nm began to oscillate at the launched pump power of 44.2 W, and an overall output power of 2.1 W was yielded at the maximum launched pump power from both fiber ends. The $\sim 1 \mu\text{m}$ parasitic oscillation reduced the lasing slope efficiency from 35% to 25.7%, which can be seen obviously in Figure 3. Despite this, no roll-off

resulting from the unfavorable nonlinear effects or thermal loading was observed. The leaked laser power from the FBG1 end was 0.2 W, which is acceptable due to the limited effective reflectivity of the high-reflection FBG. In addition, it is worth noting that the fiber laser was operated in the backward pumping regime to avoid any gain fiber burning adjacent to the combiner that commonly occurred in the forward pumping regime due to the abrupt change of temperature gradient in this position [15].

Figure 4 shows the output spectral evolution at different laser power levels from the standard single-mode fiber output end. We can see that the laser center wavelength is redshifted from 1544.44 nm near the threshold to 1544.68 nm at the output power of 19.2 W, which is primarily attributed to the temperature dependence of reflection wavelength of the FBGs. The spectral width was broadened from a FWHM linewidth of 0.04 nm to 0.08 nm correspondingly. Despite the spectral broadening, the oscillating laser modes still remained within the bandwidth of the two FBGs. In the lasing feedback of each round trip, FBG2 will sample a nominal 10% of the lasing components within its reflection band and reflect it back into the cavity. This portion of light will then be amplified in the backward direction. Upon reaching FBG1 the laser modes within the reflection band are highly reflected (99% in our case) and then successively amplified in the forward direction towards FBG2, where 90% of the laser will be outcoupled while the small reflected portion returns to the next lasing cycle. In our experiment the laser leakage from FBG1 was primarily attributed to its limited effective reflectivity since the bandwidth of FBG2 is slightly larger than that of FBG1. Despite this, the leaked laser from FBG1 was measured to have roughly the same spectral profile without central dip or any spectral ripples as that from the output end

in terms of center wavelength and width. Thus, both output beams can be simply combined for certain applications. Alternatively, we can also use a high-reflection FBG with much higher reflectivity and broader bandwidth instead to reduce the leakage power from this end.

In addition, it is worth noting that the truly single-mode laser output was actually achieved literally through first a piece of standard single-mode fiber in the cavity and then another piece of standard single-mode fiber on the output end without sacrificing much laser output power loss. Although the Er,Yb codoped gain fiber was capable of supporting 11 laser modes at $\sim 1.5 \mu\text{m}$, the amount of output laser modes from the gain fiber was actually much less than specified, owing to the intense mode competition where only the modes with lowest loss survived. Besides, the standard single-mode fiber inserted in the cavity and single-mode double clad pig-tailed fiber of FBG2 connected to the Er,Yb codoped fiber further suppressed most of the higher order laser modes yielded in the gain fiber, which ensures a relatively low splicing loss with the standard single-mode fiber. The last piece of standard single-mode fiber in the output end guaranteed a truly single-mode laser output from the 1545 nm all-fiber laser.

4. Conclusions

We demonstrate a truly single-mode all-fiber high-power Er,Yb codoped laser at 1545 nm which is potentially significant for some applications. The laser output port is convinced with a piece of standard single-mode fiber to guarantee the truly single-mode output while keeping good compatibility with other standard fiber components. A maximum overall output power of 19.2 W at 1544.68 nm with a FWHM spectral width of 0.08 nm is obtained in the fiber laser, corresponding to an average slope efficiency of 31.9% with respect to the launched pump power. To the best of our knowledge, this is the highest single-mode output power achieved from a simple all-fiber Er,Yb codoped laser oscillator architecture.

Conflicts of Interest

The authors declare that there are no conflicts of interest regarding the publication of this paper.

Authors' Contributions

Jiadong Wu and Chunxiang Zhang contributed equally to the paper.

Acknowledgments

This work is partially supported by the National Natural Science Fund Foundation of China (Grant nos. 61505124 and 61505122 and 61605166), the Science and Technology Planning Project of Guangdong Province of China (Grant no. 2016B050501005), the Educational Commission of Guangdong Province (Grant no. 2016KCXTD006), and Natural Science Foundation of SZU (Grant no. 2017022).

References

- [1] Y. Jeong, S. Yoo, C. A. Codemard et al., "Erbium:ytterbium codoped large-core fiber laser with 297-W continuous-wave output power," *IEEE Journal on Selected Topics in Quantum Electronics*, vol. 13, no. 3, pp. 573–578, 2007.
- [2] D. Y. Shen, J. K. Sahu, and W. A. Clarkson, "Highly efficient Er, Yb-doped fiber laser with 188 W free-running and > 100 W tunable output power," *Optics Express*, vol. 13, no. 13, pp. 4916–4921, 2005.
- [3] J. Liu, D. Shen, H. Huang, X. Zhang, X. Liu, and D. Fan, "Volume Bragg grating-based tunable Er,Yb fiber lasers covering the whole C- and L-band," *IEEE Photonics Technology Letters*, vol. 25, no. 15, pp. 1488–1491, 2013.
- [4] J. W. Kim, P. Jelger, J. K. Sahu, F. Laurell, and W. A. Clarkson, "High-power and wavelength-tunable operation of an Er:Yb fiber laser using a volume Bragg grating," *Optics Letters*, vol. 33, no. 11, pp. 1204–1206, 2008.
- [5] Y. Jeong, J. K. Sahu, D. B. S. Soh, C. A. Codemard, and J. Nilsson, "High-power tunable single-frequency single-mode erbium:ytterbium codoped large-core fiber master-oscillator power amplifier source," *Optics Letters*, vol. 30, no. 22, pp. 2997–2999, 2005.
- [6] Y. Chen, G. Jiang, S. Chen et al., "Mechanically exfoliated black phosphorus as a new saturable absorber for both Q-switching and mode-locking laser operation," *Optics Express*, vol. 23, no. 10, pp. 12823–12833, 2015.
- [7] G. Sobon, D. Sliwinska, K. M. Abramski, and P. Kaczmarek, "10 W single-mode Er/Yb co-doped all-fiber amplifier with suppressed Yb-ASE," *Laser Physics Letters*, vol. 11, no. 2, Article ID 025103, 2014.
- [8] B. Morasse, S. Aggerb, S. Chatignya, É. Gagnona, J. Sandroa, and C. Poulsen, "10W ASE-free single-mode high-power double-cladding Er³⁺-Yb³⁺ amplifier," in *Fiber Lasers IV: Technology, Systems, and Applications*, vol. 6453 of *Proceeding of the SPIE*, 2007.
- [9] S. Gurram, A. Kuruvilla, R. Singh, and K. S. Bindra, "Generation of 6.8 W of CW output power at 1550 nm using small mode field diameter Er:Yb co-doped double clad fiber in laser oscillator configuration," *Laser Physics*, vol. 27, no. 6, p. 065113, 2017.
- [10] P. Peterka, I. Kašik, V. Kubeček et al., "Optimization of erbium-ytterbium fibre laser with simple double-clad structure," in *Proceedings of the Photonics, Devices and Systems III*, vol. 6180 of *Proceeding of the SPIE*, 2006.
- [11] M. A. Jebali, J.-N. Maran, S. LaRochelle, S. Chatigny, M. A. Lapointe, and E. Gagnon, "A 103 W high efficiency in-band cladding-pumped 1593 nm all-fiber erbium-doped fiber laser," in *Proceedings of the CLEO: Science and Innovations, CLEO-SI '12*, p. JThI.3, May 2012.
- [12] J. Liu, D. Shen, H. Huang, C. Zhao, X. Zhang, and D. Fan, "High-power and highly efficient operation of wavelength-tunable Raman fiber lasers based on volume Bragg gratings," *Optics Express*, vol. 22, no. 6, pp. 6605–6612, 2014.
- [13] M. Wang, L. Zhu, W. Chen, and D. Fan, "Efficient all-solid-state mid-infrared optical parametric oscillator based on resonantly pumped 1.645 μm Er:YAG laser," *Optics Letters*, vol. 37, no. 13, pp. 2682–2684, 2012.
- [14] J. Liu, P. Tang, Y. Chen et al., "Highly efficient tunable mid-infrared optical parametric oscillator pumped by a wavelength locked, Q-switched Er:YAG laser," *Optics Express*, vol. 23, no. 16, pp. 20812–20819, 2015.

- [15] C. Shi, R. T. Su, H. W. Zhang et al., "Experimental study of output characteristics of bi-directional pumping high power fiber amplifier in different pumping schemes," *IEEE Photonics Journal*, vol. 9, no. 3, pp. 1-10, 2017.

Research Article

Submicrosecond Q-Switching Er-Doped All-Fiber Ring Laser Based on Black Phosphorus

Yao Cai, Yanliang He, Xiaoke Zhang, Rui Jiang, Chenliang Su, and Ying Li

SZU-NUS Collaborative Innovation Center for Optoelectronic Science & Technology,
Key Laboratory of Optoelectronic Devices and Systems of Ministry of Education and Guangdong Province,
College of Optoelectronic Engineering, Shenzhen University, Shenzhen 518060, China

Correspondence should be addressed to Ying Li; queenly@szu.edu.cn

Received 30 June 2017; Accepted 29 August 2017; Published 4 October 2017

Academic Editor: Yan Luo

Copyright © 2017 Yao Cai et al. This is an open access article distributed under the Creative Commons Attribution License, which permits unrestricted use, distribution, and reproduction in any medium, provided the original work is properly cited.

Black phosphorus (BP), a new two-dimensional (2D) material, has been deeply developed for extensive applications in electronics and optoelectronics due to its similar physical structure to graphene and thickness dependent direct band gap. Here, we demonstrated a submicrosecond passive Q-switching Er-doped fiber laser with BP as saturable absorber (SA). The BP saturable absorber was fabricated by mechanical exfoliation method. By taking full advantage of the ultrafast relaxation time of BP-SA and careful design of compact ring cavity, we obtained stable Q-switching pulses output with a shortest duration as narrow as 742 ns. With increasing the pump power, the pulse repetition rate accreted gradually almost linearly from 9.78 to 61.25 kHz, and the pulse duration declined rapidly at lower pump power regime and retained approximate stationary at higher pump power regime from 3.05 to 0.742 μ s. The experimental results indicate that BP-SA can be an effective SA for nanosecond Q-switching pulse generation.

1. Introduction

Pulsed fiber lasers have been widely applied in various applications ranging within machining, material processing, environmental sensing, medicine, laser processing, fiber sensor, and long-range optical communication. The most common pulse generation methods used in fiber laser include Q-switching and mode-locking techniques [1–6]. There are two types of Q-switching approaches: active and passive one. Among them, passive Q-switching technology based on saturable absorber (SA) has made remarkable progress in view of compact, low cost, flexible, and so on. Since the Nd:glass (the first generation of SA) was successfully used for pulse generation in 1966 [7], a wide variety of SAs have been intensively developed, such as Semiconductor Saturable Absorption Mirrors (SESAMs) [8, 9], Carbon Nanotubes (CNTs) [10–13], graphene [14–18], Topological Insulator (TI) [19, 20], and Transition Metal Dichalcogenides (TMDs) [21–24]. The SESAMs are utilized in most of commercially available laser systems for high flexibility and stability. However, SESAMs have relatively narrow operation bandwidth and require complex fabrication and packaging [1]. Recently, the research

on broadband SAs based on CNT or graphene has presented explosive development for broad operation bandwidth, ultrafast recovery times, low saturation intensity, low cost, and easy fabrication [10–18]. Nevertheless, they still have some drawbacks. The spectral response range of CNTs sensitively depends on their diameter and chirality, restricting their practical applications in specific wavelength or broadband tenability [13]. And, graphene has relatively weak optical absorption ($\sim 2.3\%$ /layer [20]) due to its gapless band structure, which limits its application in fiber laser. Another 2D material, transition metal dichalcogenides (TMDs) (MoS_2 [21], WS_2 [22], MoSe_2 [23, 24], etc.) has been developed as saturable absorber with high performances [21]. Although they have higher optical absorption at specific wavelength, the optical response mainly locates at visible region due to their comparatively large band gap (~ 1.8 eV for MoS_2 , ~ 2.1 eV for WS_2 , and ~ 1.7 eV for MoSe_2) [25, 26].

Very recently, another 2D material, black phosphorus (BP), has been rediscovered for various applications in electronics and optoelectronics [27]. Its structure is similar to graphene, in which individual atomic layers stacked together by van der Waals interaction. BP has layer-dependent direct

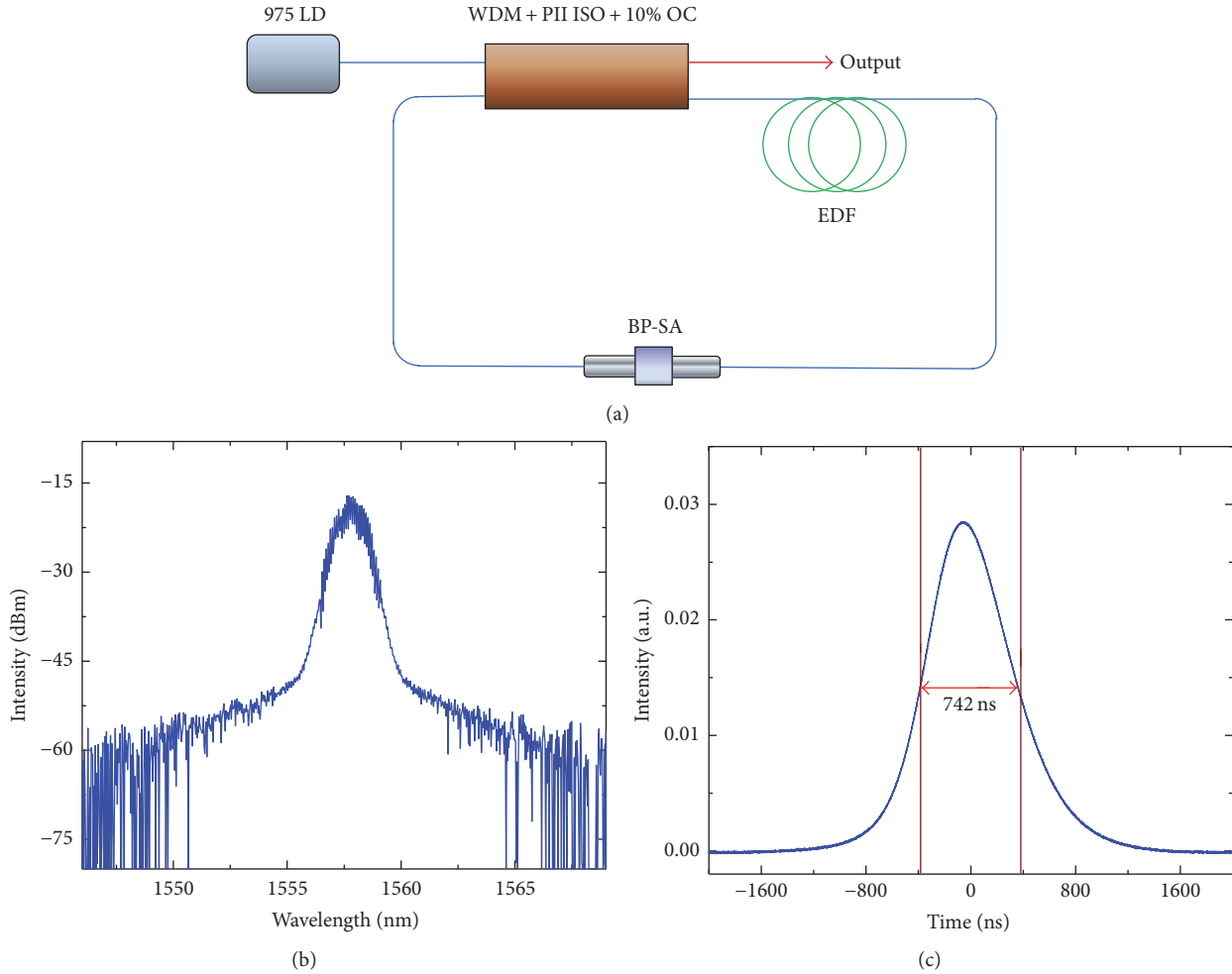


FIGURE 1: (a) Schematic of Er-doped black phosphorus-based Q-switching fiber laser. (b) Typical Q-switched output optical spectrum. (c) The minimum duration pulse obtained in our fiber laser.

electronic band gap, which can be tuned from ~ 0.3 (bulk) to ~ 2 eV (monolayer) [28], covering nearly whole near and mid-infrared wavelength. Therefore BP can be regarded as a significant benefit material for ultrafast photonics and high frequency optoelectronics in infrared wavelength. Lately, researches have paid close attention to its nonlinear optical response and used it as SA in lasers [29–31]. Even [32] shows the recovery time of BP is as short as 26 fs (much shorter than other SAs mentioned above), revealing its tremendous potential in ultrafast pulse generation.

In this paper, we also focus on the capacity of BP in ultra-short pulse generation and demonstrate a submicrosecond Q-switching pulse with a compact Er-doped all-fiber ring laser. The BP material was prepared by mechanical exfoliation method and as an effective SA for short Q-switching pulse generation. After inserting this BP-SA into a well design compact Er-doped fiber laser, we achieved stable Q-switching pulse output. The narrowest Q-switching pulse we obtained is as short as 742 ns. The experimental results show the BP's potential for narrow Q-switching pulse generation.

2. Experimental Setup and Results

The black phosphorus-based SA was prepared by mechanical exfoliation method, whose details have been shown in [30]. To achieve a submicrosecond Q-switched pulse, ultrashort laser cavity should be employed. We designed a special compact all-fiber ring cavity shown in Figure 1(a) with an optical integrated device for the joint function of wavelength-division multiplexer (WDM), polarization-insensitive isolator (PI-ISO), and 10% output coupler (OC). The total cavity length is 4.7 m with 0.95 m highly doped erbium-doped fiber (EDF, LIEKKI Er 80-8/125) as gain medium. Others are standard single-mode fiber (SMF-28). The laser is pumped by a 975 nm laser diode (LD) with maximum power of 500 mW. The BP-SA is incorporated into the cavity between the EDF and integrated device. There is not any extra component in this fiber laser. The output is characterized by an optical spectrum analyzer (Ando AQ-6317B) and a real-time oscilloscope with bandwidth of 4 GHz (Agilent Technol., DSO9404A) combined with a 5 GHz photodetector (Thorlabs SIR5).

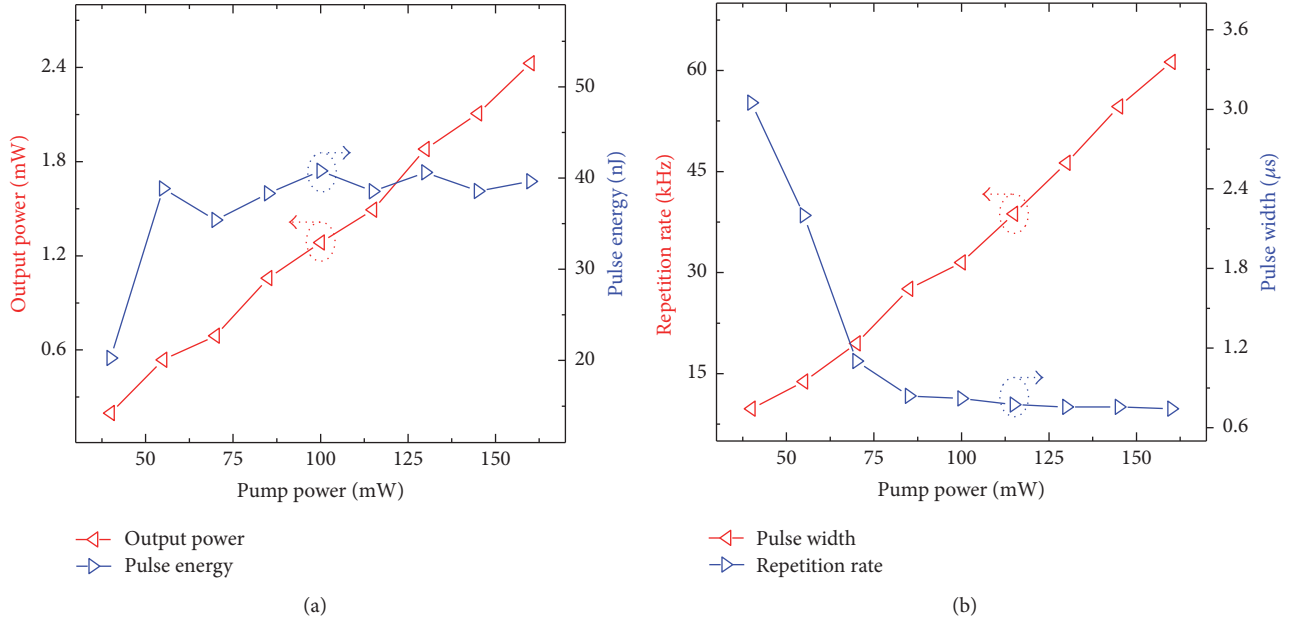


FIGURE 2: The evolution of output average power and pulse energy (a) and pulse repetition rate and duration versus incident pump power (b) as pump power increases.

Without the BP-SA device, the central wavelength is located at 1600 nm, suggesting that the optical integrated device possesses low insertion loss. In this condition, we cannot obtain Q-switching operation state no matter how we adjust pump power and apply stress on fiber (correspondingly changing fiber birefringence to control the polarization rate of light in cavity). After the BP-SA device is introduced into the cavity, stable Q-switching output can be obtained once the pump power exceeds 40 mW. Figure 1(b) shows typical Q-switching spectrum with slight modulation. The central wavelength is 1557.9 nm. With increasing pump power, the durations of Q-switching pulse decrease gradually. At max revealable pump power of 160 mW, we obtained minimum pulse width as narrow as 742 ns as shown in Figure 1(c). It is worth noting that, keeping increasing pump power above 160 mW, the Q-switching state becomes unstable and disappears ultimately.

In addition, we also measured the evolution process of pulses with the pump power increasing to confirm the Q-switching operating state, shown in Figure 2. As it can be seen, with pump power increasing from 40 to 160 mW, the average output power increases almost linearly from 198 μ W to 2.43 mW, but the pulse energy fluctuates between 20.2 and 40.8 nJ. Simultaneously, the pulse repetition rate accretes gradually also almost linearly from 9.78 to 61.25 kHz, and the pulse duration declines rapidly at lower pump power regime and keeps approximately unchanged at higher power regime from 3.05 to 0.742 μ s. These entire matches with typical Q-switching state confirm its operating state.

3. Conclusions

In conclusion, we focus on the capacity of BP in ultra-short pulse generation and demonstrate a submicrosecond

Q-switching pulse with a compact Er-doped all-fiber ring laser. The BP material was prepared by mechanical exfoliation method and as an effective SA for short Q-switching pulse generation. It has narrow Q-switching pulse as short as 742 ns. With increasing the pump power, the pulse repetition rate accreted gradually almost linearly from 9.78 to 61.25 kHz, and the pulse duration declined rapidly at lower pump power regime and retained approximate stationary at higher pump power regime from 3.05 to 0.742 μ s. The experimental results indicate that BP-SA can be an effective SA for nanosecond Q-switching pulse generation.

Conflicts of Interest

The authors declare that there are no conflicts of interest regarding the publication of this paper.

Acknowledgments

The authors would like to acknowledge supports from the National Natural Science Foundation of China (Grant nos. 61575127, 61505122, and 61505117), the Natural Science Foundation of Guangdong Province (Grant nos. 2016A030310065 and 2014A030310279), the Science and Technology Planning Project of Guangdong Province (Grant no. 2016B050501005), and the Educational Commission of Guangdong Province (Grant nos. 2016KCXTD006 and 2015KQNCX146).

References

- [1] U. Keller, "Recent developments in compact ultrafast lasers," *Nature*, vol. 424, no. 6950, pp. 831–838, 2003.
- [2] V. V. Dvoryin, V. M. Mashinsky, and E. M. Dianov, "Yb - Bi pulsed fiber lasers," *Optics Letters*, vol. 32, no. 5, pp. 451–453, 2007.

- [3] P. Dupriez, A. Piper, A. Malinowski et al., "High average power, high repetition rate, picosecond pulsed fiber master oscillator power amplifier source seeded by a gain-switched laser diode at 1060 nm," *IEEE Photonics Technology Letters*, vol. 18, no. 9, pp. 1013–1015, 2006.
- [4] F. X. Kärtner, J. Aus der Au, and U. Keller, "Mode-locking with slow and fast saturable absorbers—what's the difference?" *IEEE Journal on Selected Topics in Quantum Electronics*, vol. 4, no. 2, pp. 159–168, 1998.
- [5] H. L. Offerhaus, N. G. Broderick, D. J. Richardson, R. Sammut, J. Caplen, and L. Dong, "High-energy single-transverse-mode Q-switched fiber laser based on a multimode large-mode-area erbium-doped fiber," *Optics Letters*, vol. 23, no. 21, pp. 1683–1685, 1998.
- [6] B. Ding, Y. Cheng, J. Wu et al., "A unique multifunctional cluster-based nano-porous Terbium organic material: real-time detection of benzaldehyde, visually luminescent sensor for nitrite and selective high capacity capture of Congo Red," *Dyes and Pigments*, vol. 146, pp. 455–466, 2017.
- [7] D. A. Stetser and A. J. Demaria, "Optical spectra of ultra-short optical pulses generated by mode-locked glass:nd lasers," *Applied Physics Letters*, vol. 9, no. 3, pp. 118–120, 1966.
- [8] U. Keller, K. J. Weingarten, F. X. Kärtner et al., "Semiconductor saturable absorber mirrors (SESAM's) for femtosecond to nanosecond pulse generation in solid-state lasers," *IEEE Journal on Selected Topics in Quantum Electronics*, vol. 2, no. 3, pp. 435–451, 1996.
- [9] J. F. Li, H. Y. Luo, Y. L. He et al., "Semiconductor saturable absorber mirror passively Q-switched 2.97 μm fluoride fiber laser," *Laser Physics Letters*, vol. 11, no. 6, Article ID 065102, 2014.
- [10] S. W. Harun, M. A. Ismail, F. Ahmad et al., "A Q-switched erbium-doped fiber laser with a carbon nanotube based saturable absorber," *Chinese Physics Letters*, vol. 29, no. 11, Article ID 114202, 2012.
- [11] B. Dong, J. Hao, J. Hu, and C.-Y. Liaw, "Short linear-cavity Q-switched fiber laser with a compact short carbon nanotube based saturable absorber," *Optical Fiber Technology*, vol. 17, no. 2, pp. 105–107, 2011.
- [12] K. Kieu and F. W. Wise, "Soliton thulium-doped fiber laser with carbon nanotube saturable absorber," *IEEE Photonics Technology Letters*, vol. 21, no. 3, pp. 128–130, 2009.
- [13] D.-P. Zhou, L. Wei, B. Dong, and W.-K. Liu, "Tunable passively Q-switched erbium-doped fiber laser with carbon nanotubes as a saturable absorber," *IEEE Photonics Technology Letters*, vol. 22, no. 1, pp. 9–11, 2010.
- [14] W.-J. Cao, H.-Y. Wang, A.-P. Luo, Z.-C. Luo, and W.-C. Xu, "Graphene-based, 50 nm wide-band tunable passively Q-switched fiber laser," *Laser Physics Letters*, vol. 9, no. 1, pp. 54–58, 2012.
- [15] L. Q. Zhang, Z. Zhuo, J. X. Wang, and Y. Z. Wang, "Passively Q-switched fiber laser based on graphene saturable absorber," *Laser Physics*, vol. 22, no. 2, pp. 433–436, 2012.
- [16] Z. T. Wang, Y. Chen, C. J. Zhao, H. Zhang, and S. C. Wen, "Switchable dual-wavelength synchronously Q-switched erbium-doped fiber laser based on graphene saturable absorber," *IEEE Photonics Journal*, vol. 4, no. 3, pp. 869–876, 2012.
- [17] H. Ahmad, F. D. Muhammad, M. Z. Zulkifli, and S. W. Harun, "Graphene-oxide-based saturable absorber for all-fiber Q-switching with a simple optical deposition technique," *IEEE Photonics Journal*, vol. 4, no. 6, pp. 2205–2213, 2012.
- [18] Q. Bao, H. Zhang, Y. Wang et al., "Atomic-layer craphene as a saturable absorber for ultrafast pulsed lasers," *Advanced Functional Materials*, vol. 19, no. 19, pp. 3077–3083, 2009.
- [19] C. Zhao, H. Zhang, and X. Qi, "Ultra-short pulse generation by a topological insulator based saturable absorber," *Applied Physics Letters*, vol. 101, no. 21, Article ID 211106, 2012.
- [20] S. Chen, L. Miao, X. Chen et al., "Few-layer topological insulator for all-optical signal processing using the nonlinear kerr effect," *Advanced Optical Materials*, vol. 3, no. 12, pp. 1769–1778, 2015.
- [21] H. Zhang, S. B. Lu, J. Zheng et al., "Molybdenum disulfide (MoS₂) as a broadband saturable absorber for ultra-fast photonics," *Optics Express*, vol. 22, no. 6, pp. 7249–7260, 2014.
- [22] M. Zhang, G. Hu, G. Hu et al., "Yb- and Er-doped fiber laser Q-switched with an optically uniform, broadband WS₂ saturable absorber," *Scientific Reports*, vol. 5, Article ID 17482, 2015.
- [23] B. Chen, X. Zhang, K. Wu, H. Wang, J. Wang, and J. Chen, "Q-switched fiber laser based on transition metal dichalcogenides MoS₂, MoSe₂, WS₂, and WSe₂," *Optics Express*, vol. 23, no. 20, pp. 26723–26737, 2015.
- [24] R. I. Woodward, R. C. T. Howe, T. H. Runcorn et al., "Wide-band saturable absorption in few-layer molybdenum diselenide (MoSe₂) for Q-switching Yb-, Er- and Tm-doped fiber lasers," *Optics Express*, vol. 23, no. 15, pp. 20051–20061, 2015.
- [25] F. Bonaccorso and Z. Sun, "Solution processing of graphene, topological insulators and other 2d crystals for ultrafast photonics," *Optical Materials Express*, vol. 4, no. 1, pp. 63–78, 2014.
- [26] Q. H. Wang, K. Kalantar-Zadeh, A. Kis, J. N. Coleman, and M. S. Strano, "Electronics and optoelectronics of two-dimensional transition metal dichalcogenides," *Nature Nanotechnology*, vol. 7, no. 11, pp. 699–712, 2012.
- [27] F. Xia, H. Wang, and Y. Jia, "Rediscovering black phosphorus as an anisotropic layered material for optoelectronics and electronics," *Nature Communications*, vol. 5, article 4458, 2014.
- [28] L. Li, Y. Yu, G. J. Ye et al., "Black phosphorus field-effect transistors," *Nature Nanotechnology*, vol. 9, no. 5, pp. 372–377, 2014.
- [29] Y. Chen, G. Jiang, S. Chen et al., "Mechanically exfoliated black phosphorus as a new saturable absorber for both Q-switching and mode-locking laser operation," *Optics Express*, vol. 23, no. 10, pp. 12823–12833, 2015.
- [30] J. Sotor, G. Sobon, W. Macherzynski, P. Paletko, and K. M. Abramski, "Black phosphorus saturable absorber for ultrashort pulse generation," *Applied Physics Letters*, vol. 107, no. 5, Article ID 051108, 2015.
- [31] Z.-C. Luo, M. Liu, Z.-N. Guo et al., "Microfiber-based few-layer black phosphorus saturable absorber for ultra-fast fiber laser," *Optics Express*, vol. 23, no. 15, pp. 20030–20039, 2015.
- [32] H. Mu, S. Lin, Z. Wang et al., "Black phosphorus-polymer composites for pulsed lasers. *Advanced Optical Materials*," *Advanced Optical Materials*, vol. 3, no. 10, pp. 1447–1453, 2015.

Research Article

Self-Reconstruction Property of a Special Speckle Pattern after Obstructing by an Opaque Obstruction

Yanyu Chen, Huang Tan, and Gaofeng Wu

School of Physics, Northwest University, Xi'an 710069, China

Correspondence should be addressed to Gaofeng Wu; gfwu@nwu.edu.cn

Received 29 June 2017; Accepted 21 August 2017; Published 26 September 2017

Academic Editor: Shuqing Chen

Copyright © 2017 Yanyu Chen et al. This is an open access article distributed under the Creative Commons Attribution License, which permits unrestricted use, distribution, and reproduction in any medium, provided the original work is properly cited.

Numerical simulation of random optical field with special autocorrelation is performed. It can be seen that the speckle pattern with special autocorrelation is different from the general speckle pattern whose autocorrelation is a Gaussian function. Furthermore, we study the propagation property of the special speckle in free space after blocking by an opaque obstruction and find the self-healing effect of speckle. In particular, we investigate the influence of size and shape of obstruction and the coherence of speckle on the speckle's reconstruction process. We find that it is affected by the size of obstruction and the coherence of the speckle but is almost not affected by the shape of obstruction. Our results can be applied to the imaging, optical communication, and so on.

1. Introduction

Random scattering strongly distorts the optical fields, creating the well-known speckle pattern. The speckle pattern is formed by superposing all the random optical fields. In past times, speckle pattern is harmful to the optical imaging, optical communication, and so on. People usually avoid producing speckle. However, in recent years, random scattering has emerged as a rich research field. This is because it has useful application. The scattering field can form a subwavelength focal spot by modulating the wavefront [1, 2]. Disordered scattering has been applied to improve imaging resolution [3–5]. Noninvasive imaging of a fluorescent object has been done by measuring the autocorrelation of the speckle [6]. The biological imaging using speckle scanning microscopy was studied [7].

There are some special light beams, called nondiffraction beam, can keep its beam profile during propagation, like Bessel beams [8], Airy beams [9], and so on. They can be self-healing when those beams are partially blocked by an opaque obstruction. Hence, they have been widely applied to microscopic particle manipulation [10], human tissue microscopy [11], quantum entanglement propagation in the presence of obstructions [12], and optical communications through inhomogeneous media [13, 14]. In 2014, Alves et al.

found that the speckle showed a robust self-healing property [15], but they only paid attention to the speckle generated by the Gaussian beam and the Bessel beam. In the present paper, we will simulate the special speckle generated by the hyperbolic cosine-Gaussian beam and investigate its propagation after blocking by an opaque obstruction.

2. Simulation of the Speckle Generation

Speckle pattern is the random intensity distribution. The numerical simulation of the speckle can follow Goodman's book [16]. We use a matrix with 512×512 pixels and every pixel size is 0.097656 mm. First, a matrix of random phasors was generated and then multiplied by the incident beam. The incident beam can be Gaussian, Bessel, or other kinds of beams. Here, we use the hyperbolic cosine-Gaussian function as the incident beam

$$I(f_x, f_y) = 2\pi\delta^2 \cosh(n\sqrt{2\pi}\delta f_x) \cosh(n\sqrt{2\pi}\delta f_y) \cdot \exp\left(-\frac{\delta^2(f_x^2 + f_y^2) + 2n^2\pi}{2}\right), \quad (1)$$

where n and δ are positive real constants. $\cosh(x)$ is the hyperbolic cosine function. After that, we can get the speckle

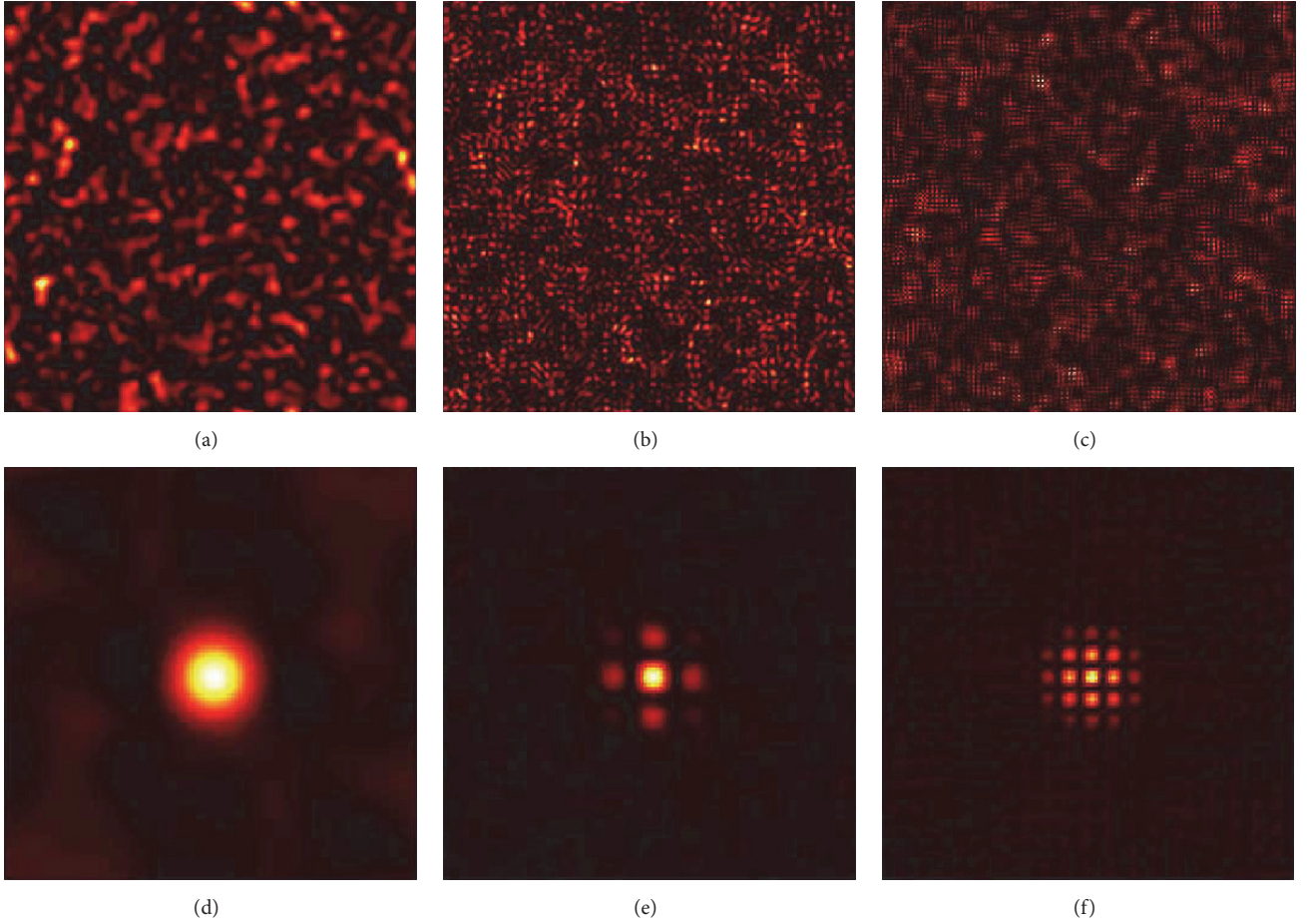


FIGURE 1: The simulation of speckle pattern in the source plane for different n with $\delta = 6$ mm, (a) $n = 0$, (b) $n = 1$, and (c) $n = 2$ and the autocorrelation corresponding to the speckle pattern, (d) $n = 0$, (e) $n = 1$, and (f) $n = 2$.

by performing the fast Fourier transform of the resulting matrix. Figure 1 shows the speckle pattern for selected value of n . One can find that the parameter n affects the speckle distribution. We obtain the ordinary speckle, that is, Gaussian speckle, when $n = 0$, and the special speckle pattern when $n \neq 0$. The difference among those patterns can be found from the autocorrelation which is defined as

$$\begin{aligned} AC(\Delta x, \Delta y) &= \iint I_{\text{out}}(x, y) I_{\text{out}}(x - \Delta x, y - \Delta y) dx dy, \end{aligned} \quad (2)$$

where $I_{\text{out}}(x, y) = E^*(x, y)E(x, y)$ is the speckle pattern, that is, the speckle intensity, and $E(x, y)$ is the electric field. For the Gaussian speckle, its autocorrelation is a Gaussian distribution [see Figure 1(a)], but the autocorrelation of those speckle with $n \neq 0$ is different. There is a spot in the center surrounded by other spots. The amount of the surrounded spots is large when the value of n is large [see Figure 1(c)]. Figure 2 shows the speckle pattern and autocorrelation for different δ . It is found that the average size of the speckle (speckle-coherence length) increases as

the value of δ increases. That is also reflected by the pattern of autocorrelation. It is big with a large value of δ . If we change the value of δ with different n , one can see the average size of the speckle pattern change. It is also found that the size of the autocorrelation varies as the value of δ changes. In fact, the inverse of δ is related to the incident beam size [17]. Therefore, we can control the average size of the speckle by varying the beam size of the incident beam.

3. The Propagation of Speckle

The propagation of the speckle can be expressed by the Huygens-Fresnel integral as

$$\begin{aligned} E_2(x_2, y_2, z) &= \left(-\frac{i}{\lambda z}\right) \exp(ikz) \iint E_1(x_1, y_1, 0) \\ &\times \exp\left\{\frac{ik}{2z} [(x_2 - x_1)^2 + (y_2 - y_1)^2]\right\} dx_1 dy_1, \end{aligned} \quad (3)$$

where $E_1(x_1, y_1, 0)$ and $E_2(x_2, y_2, z)$ are the random electric field in the source plane and received plane, respectively. $k = 2\pi/\lambda$ denotes the wavenumber with wavelength λ . x_1, y_1 and

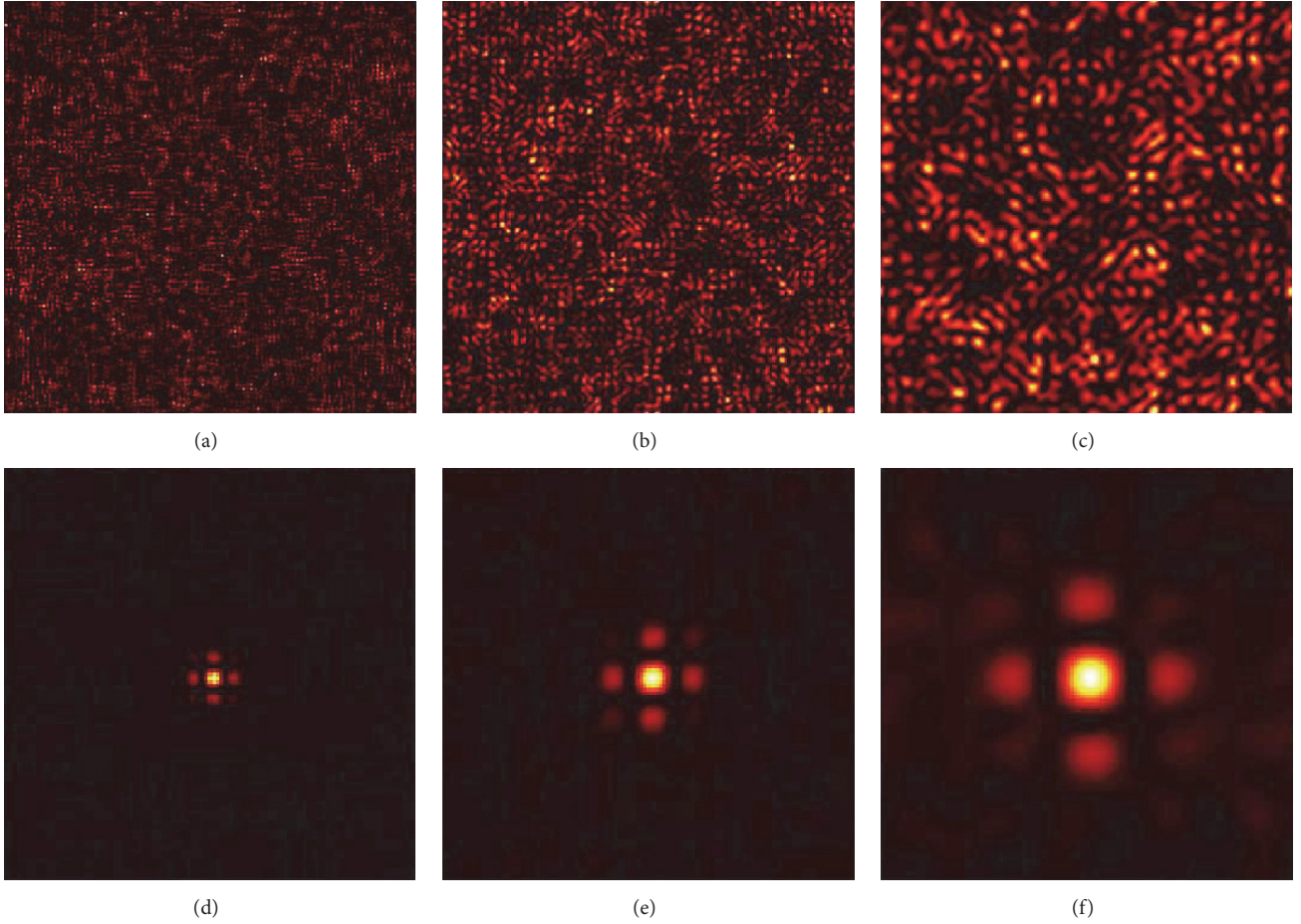


FIGURE 2: The simulation of speckle pattern in the source plane and corresponding to the autocorrelation for different δ with $n = 1$, (a), (d) $\delta = 3$ mm, (b), (e) $\delta = 6$ mm, and (c), (f) $\delta = 12$ mm.

x_2, y_2 are the transverse coordinates in the source plane and received plane. Equation (3) can be written in an altered form as

$$E_2(x_2, y_2, z) = \left(-\frac{i}{\lambda z}\right) \exp(ikz) \exp\left[\frac{ik}{2z}(x_2^2 + y_2^2)\right] \cdot \int \int E_1(x_1, y_1, 0) \exp\left[\frac{ik}{2z}(x_1^2 + y_1^2)\right] \cdot \exp\left[-\frac{ik}{z}(x_2x_1 + y_2y_1)\right] dx_1 dy_1. \quad (4)$$

One can find from (4) that the integral is a Fourier transform. Namely,

$$E_2(x_2, y_2, z) = \left(-\frac{i}{\lambda z}\right) \exp(ikz) \exp\left[\frac{ik}{2z}(x_2^2 + y_2^2)\right] \times \bar{F} \left\{ E_1(x_1, y_1, 0) \exp\left[\frac{ik}{2z}(x_1^2 + y_1^2)\right] \right\}. \quad (5)$$

The Fourier transform can be easily performed by the fast Fourier transform algorithm. If the speckle in the source plane is blocked by an opaque obstruction, the propagation of the missing speckle can be expressed as

$$E_2(x_2, y_2, z) = \left(-\frac{i}{\lambda z}\right) \exp(ikz) \exp\left[\frac{ik}{2z}(x_2^2 + y_2^2)\right] \times \bar{F} \left\{ E_1(x_1, y_1, 0) T(x_1, y_1, 0) \cdot \exp\left[\frac{ik}{2z}(x_1^2 + y_1^2)\right] \right\}, \quad (6)$$

where $T(x_1, y_1, 0)$ denotes the transmission function of the obstruction. When $T(x_1, y_1, 0) = 1$ for every point in the source plane, the random field $E_1(x_1, y_1, 0)$ does not been modulated by the obstruction. That means there is no obstruction. When $T(x_1, y_1, 0) = 0$ which means the random field is completely blocked by the obstruction, the speckle can not propagate. We will investigate the situation that the speckle is partially blocked by the obstruction. The

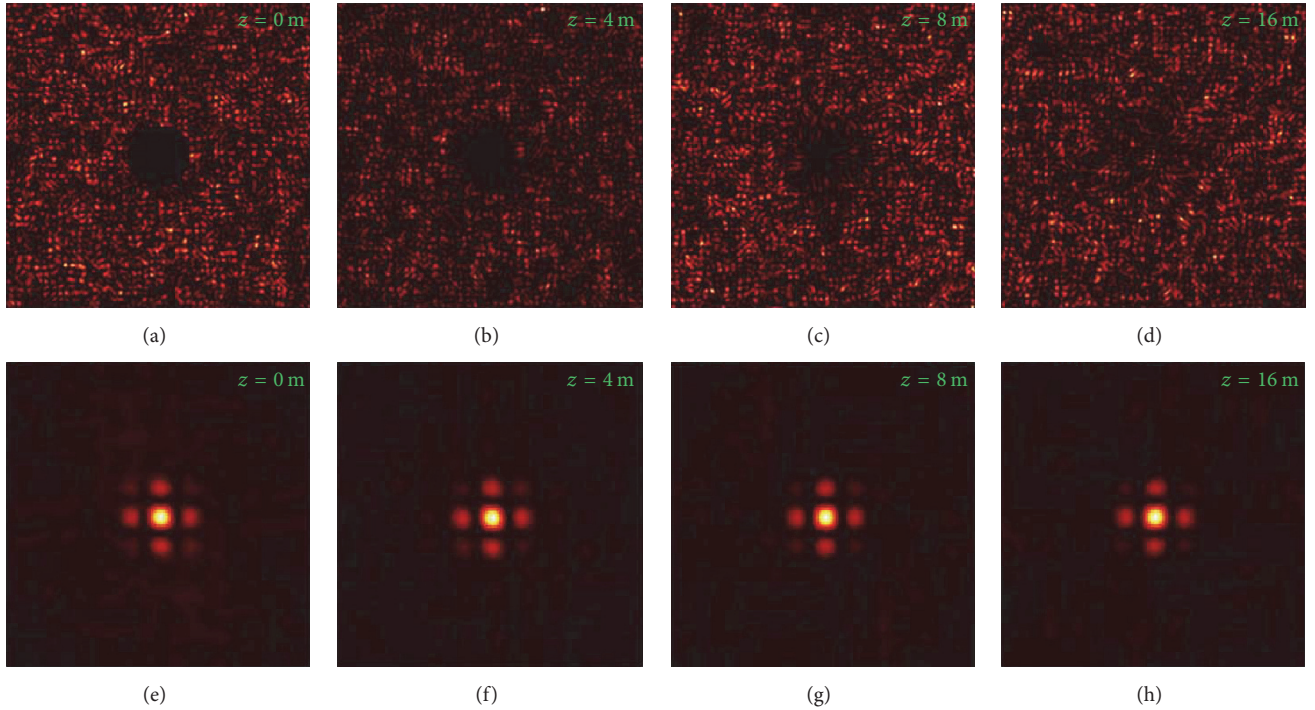


FIGURE 3: (a)–(d) The simulation of speckle pattern at different propagating distances with $R = 5$ mm, $\delta = 6$ mm, and $n = 1$. (e)–(h) corresponding to the distribution of the autocorrelation.

wavelength λ is 632.8 nm. The obstruction is an opaque disk with radius $R = 5$ mm.

From Figure 3, one can find that the speckle pattern in the source plane is blocked by an opaque disk in the center. Therefore, one can find a black hole in the center. However, the hole gradually disappears as the speckle propagates in free space. When the speckle propagates to the plane $z = 16$ m, one almost cannot find the hole in the center. That means the speckle can reconstruct itself as it propagates in free space. On the other hand, it is found that the autocorrelation at every plane is almost the same. In other words, the autocorrelation almost is not affected by the obstruction.

The influence of the size of obstruction on the reconstruction of speckle is showed in Figure 4. The first row shows the speckle in the source plane with different size of obstruction. The second row shows the speckle pattern in the plane of $z = 16$ m. One can find that the speckle with a small obstruction can primarily reconstruct itself, whereas the speckle with a large obstruction does not at the same propagating distance. It needs long distance to diffract and to finish its reconstruction. The third row shows the autocorrelation in the plane of $z = 16$ m. It is found that the autocorrelation distribution is hardly affected by the size of the obstruction. Figure 5 shows the influence of the shape of obstruction on the reconstruction of speckle pattern and on autocorrelation. The obstruction has the same area but with different shape. It is found that the shape does not affect the reconstruction of speckle pattern. Although the pattern is partially blocked by different shape of obstruction, it can be self-healing as the speckle propagates

in free space. As showed in the second row of Figure 5, all the speckle patterns finished their reconstruction process and one cannot find the obvious hole in the center. One can also find that the autocorrelation of the speckle pattern in the plane of $z = 16$ m is the same. They keep the same shape as it in the source plane. Figure 6 shows the speckle pattern at different propagating distance for different coherence length. One can find that there is a circle hole in the center of the speckle pattern with the coherence length $\delta = 3$ mm in the source plane. This is because the opaque obstruction partially blocks the speckle. When the speckle propagates to the plane of $z = 4$ m, one can still find the hole. However, there is no obvious hole when the speckle propagates to the plane of $z = 8$ m. That means the speckle almost finished its reconstruction process when it propagates to the plane of $z = 8$ m. However, in the second row, one can find that there is a hole in the center when the speckle propagates to the same distance $z = 8$ m and it disappears at the plane of $z = 16$ m. In the third row, one can find that the hole disappears at the plane of $z = 28$ m. Those imply that the speckles with a high coherence need a long propagating distance to reconstruct themselves.

4. Conclusions

We have simulated the laser speckle with special autocorrelation and investigated its propagation in free space after partial blocking by an opaque obstruction. It was found that the missing speckle pattern can reconstruct itself and

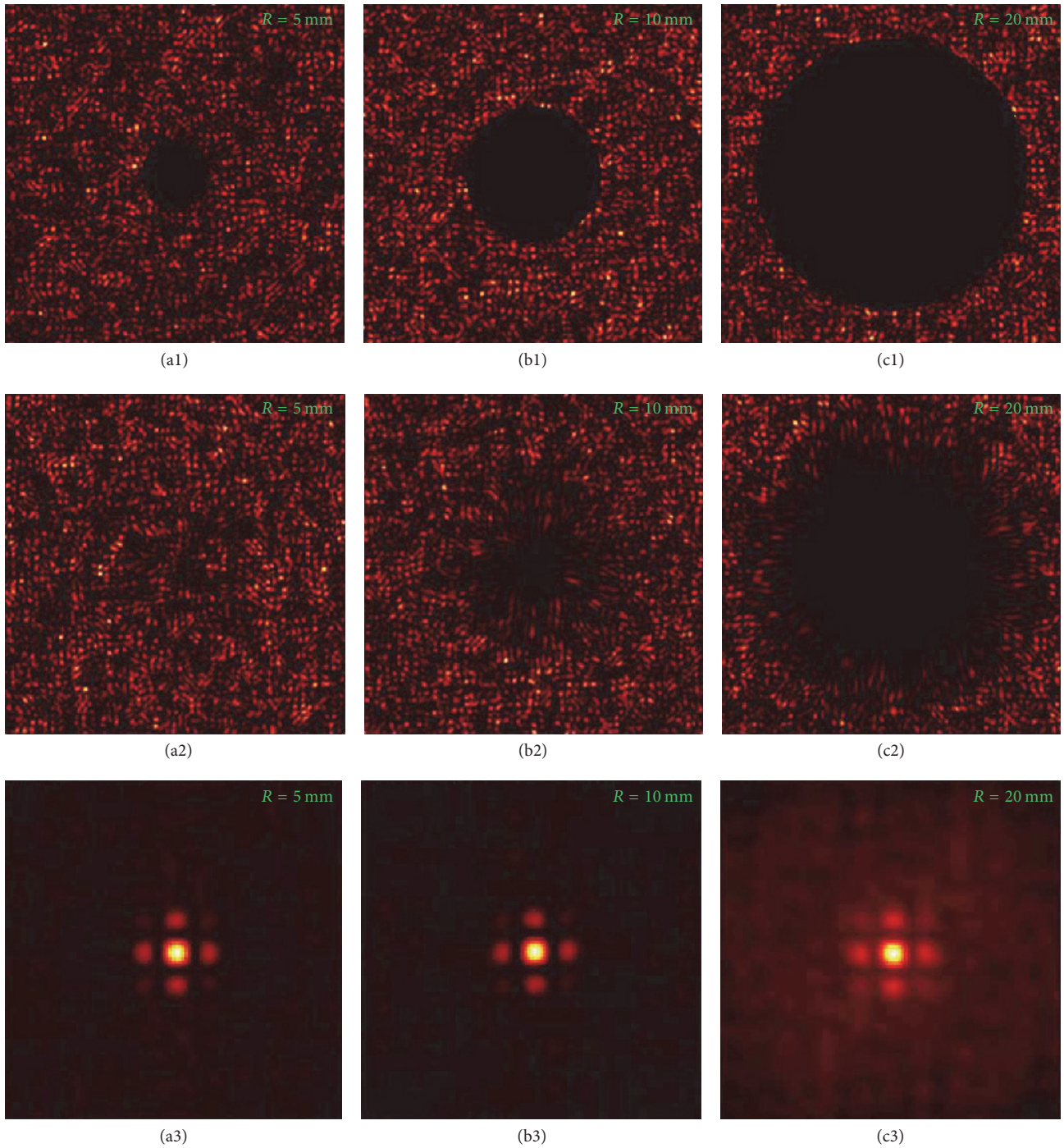


FIGURE 4: The simulation of speckle pattern and corresponding to the autocorrelation for different size of obstruction with $\delta = 6$ mm; $n = 1$. The first row denotes the speckle pattern in the source plane, the second row denotes the speckle pattern in the plane of $z = 16$ m, and the third row denotes the autocorrelation of the speckle pattern in the second row.

its autocorrelation kept the same shape as it propagated in free space. The reconstruction of the speckle is not affected by the shape of the obstruction but relates to the size of the obstruction. The speckle needs a long distance to reconstruct itself when the size of the obstruction is large. We also found the influence of coherence of speckle on

its reconstruction. The speckle needs a long propagating distance to reconstruct when the coherence of the speckle is high. It is also found that the size and shape of the obstruction have a little influence on the autocorrelation. This implies that we can use the autocorrelation to resist disturbance and load information.

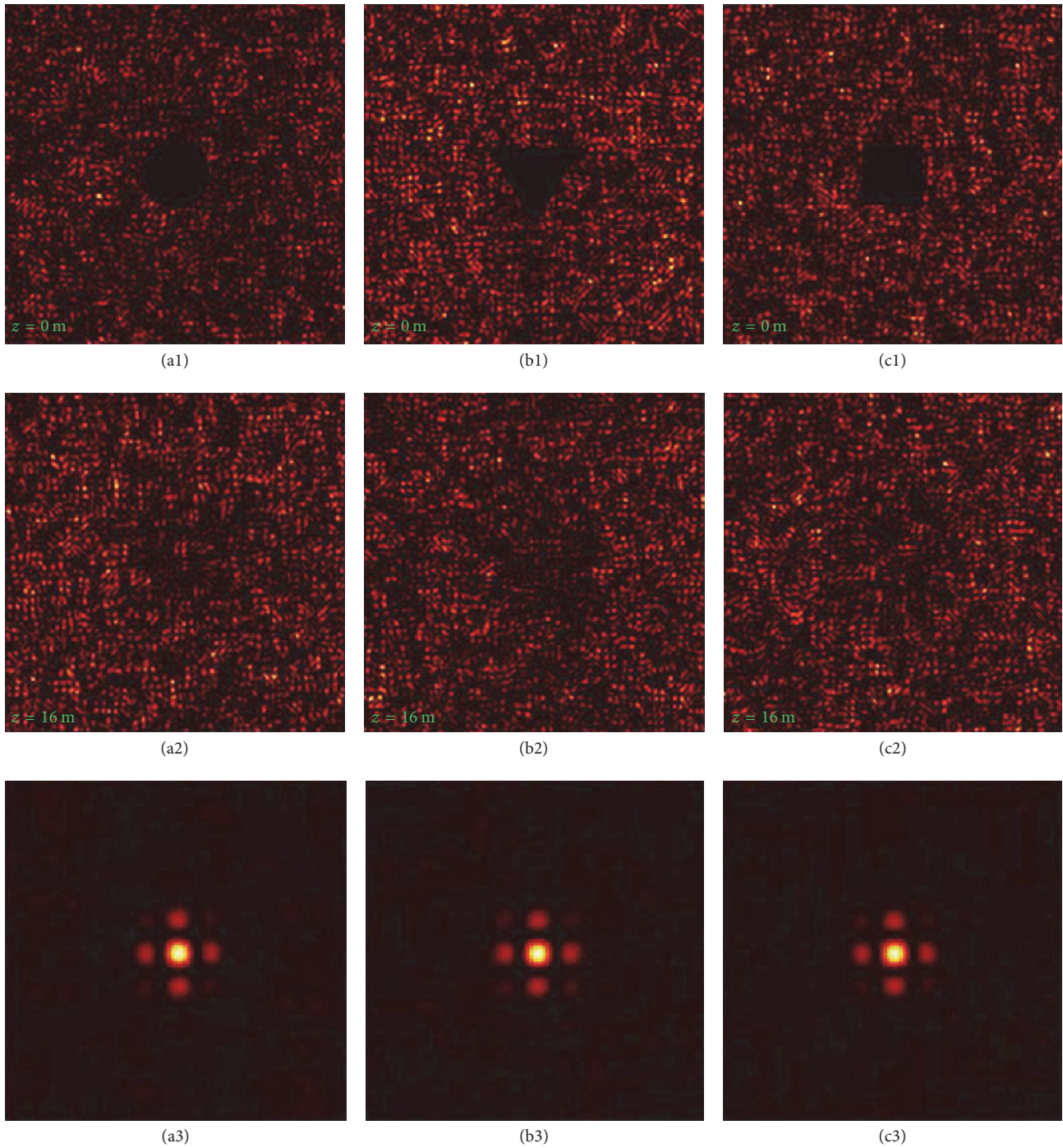


FIGURE 5: The simulation of speckle pattern and corresponding to the autocorrelation for different shape of obstruction with $\delta = 6$ mm; $n = 1$. The shape of the obstruction is circle (a1), equilateral triangle (b1) and square (c1). The first row denotes the speckle pattern in the source plane, the second row denotes the speckle pattern in the plane of $z = 16$ m, and the third row denotes the autocorrelation of the speckle pattern in the second row.

Conflicts of Interest

The authors declare that there are no conflicts of interest regarding the publication of this paper.

Acknowledgments

This work is supported by Natural Science Basic Research Plan in Shaanxi Province of China (Program no. 2016JQ1021);

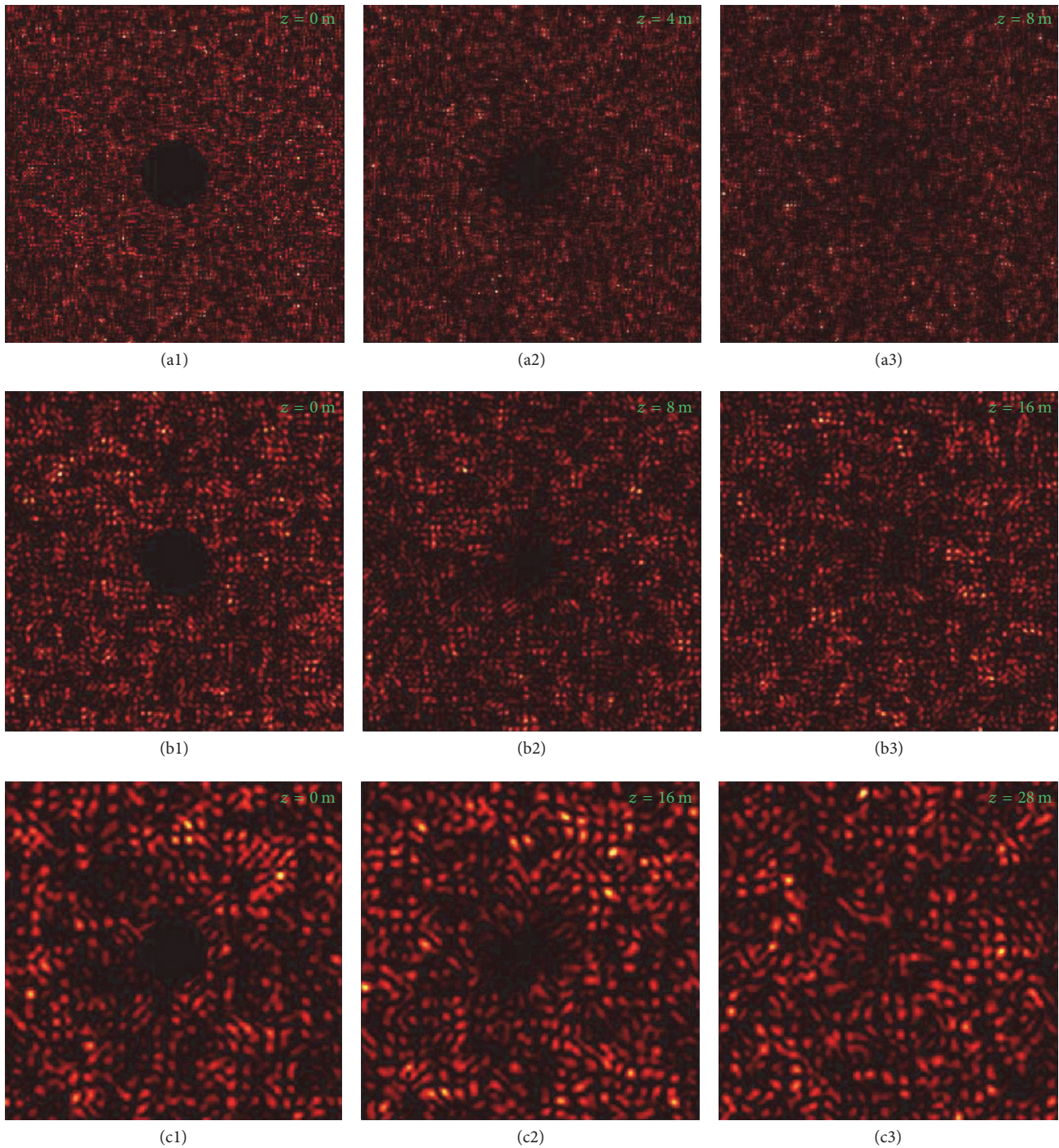


FIGURE 6: The simulation of speckle pattern at different propagating distance for different coherence length with $R = 5$ mm, $n = 1$. The first row $\delta = 3$ mm, the second row $\delta = 6$ mm, and the third row $\delta = 12$ mm.

the National Natural Sciences Foundation of China (NSFC) (11604264); Science Foundation of Northwest University (15NW28).

References

- [1] I. M. Vellekoop, A. Lagendijk, and A. P. Mosk, "Exploiting disorder for perfect focusing," *Nature Photonics*, vol. 4, no. 5, pp. 320–322, 2010.
- [2] O. Katz, E. Small, Y. Bromberg, and Y. Silberberg, "Focusing and compression of ultrashort pulses through scattering media," *Nature Photonics*, vol. 5, no. 6, pp. 372–377, 2011.
- [3] I. M. Vellekoop and C. M. Aegerter, "Scattered light fluorescence microscopy: Imaging through turbid layers," *Optics Letters*, vol. 35, no. 8, pp. 1245–1247, 2010.
- [4] E. G. Van Putten, D. Akbulut, J. Bertolotti, W. L. Vos, A. Lagendijk, and A. P. Mosk, "Scattering lens resolves sub-100 nm

- structures with visible light,” *Physical Review Letters*, vol. 106, no. 19, Article ID 193905, 2011.
- [5] Y. Choi, T. D. Yang, C. Fang-Yen et al., “Overcoming the diffraction limit using multiple light scattering in a highly disordered medium,” *Physical Review Letters*, vol. 107, no. 2, Article ID 023902, 2011.
- [6] J. Bertolotti, E. G. Van Putten, C. Blum, A. Lagendijk, W. L. Vos, and A. P. Mosk, “Non-invasive imaging through opaque scattering layers,” *Nature*, vol. 491, no. 7423, pp. 232–234, 2012.
- [7] X. Yang, Y. Pu, and D. Psaltis, “Imaging blood cells through scattering biological tissue using speckle scanning microscopy,” *Optics Express*, vol. 22, no. 3, pp. 3405–3413, 2014.
- [8] J. Durnin, J. Miceli Jr., and J. H. Eberly, “Diffraction-free beams,” *Physical Review Letters*, vol. 58, no. 15, pp. 1499–1501, 1987.
- [9] G. A. Siviloglou, J. Broky, A. Dogariu, and D. N. Christodoulides, “Observation of accelerating airy beams,” *Physical Review Letters*, vol. 99, no. 21, Article ID 213901, 2007.
- [10] V. Garcés-Chávez, D. McGloin, H. Melville, W. Sibbett, and K. Dholakia, “Simultaneous micromanipulation in multiple planes using a self-reconstructing light beam,” *Nature*, vol. 419, no. 6903, pp. 145–147, 2002.
- [11] F. O. Fahrbach, P. Simon, and A. Rohrbach, “Microscopy with self-reconstructing beams,” *Nature Photonics*, vol. 4, no. 11, pp. 780–785, 2010.
- [12] M. McLaren, T. Mhlanga, M. J. Padgett, F. S. Roux, and A. Forbes, “Self-healing of quantum entanglement after an obstruction,” *Nature Communications*, vol. 5, article no. 3248, 2014.
- [13] J. Broky, G. A. Siviloglou, A. Dogariu, and D. N. Christodoulides, “Self-healing properties of optical Airy beams,” *Optics Express*, vol. 16, no. 17, pp. 12880–12891, 2008.
- [14] Y. Yuan, T. Lei, Z. Li et al., “Beam wander relieved orbital angular momentum communication in turbulent atmosphere using Bessel beams,” *Scientific Reports*, vol. 7, Article ID 42276, 2017.
- [15] C. R. Alves, A. J. Jesus-Silva, and E. J. S. Fonseca, “Self-reconfiguration of a speckle pattern,” *Optics Letters*, vol. 39, no. 21, pp. 6320–6323, 2014.
- [16] J. W. Goodman, *Speckle Phenomena in Optics: Theory and Applications*, Roberts, 2007.
- [17] C. Liang, F. Wang, X. Liu, Y. Cai, and O. Korotkova, “Experimental generation of cosine-Gaussian-correlated Schell-model beams with rectangular symmetry,” *Optics Letters*, vol. 39, no. 4, pp. 769–772, 2014.

Research Article

Dynamics of Dispersive Wave Generation in Gas-Filled Photonic Crystal Fiber with the Normal Dispersion

Zhixiang Deng¹ and Meng Zhang²

¹*School of Electrical Engineering, University of South China, Hengyang 421001, China*

²*Oriental Science and Technology College, Hunan Agricultural University, Changsha 410082, China*

Correspondence should be addressed to Meng Zhang; zhangmeng024678@163.com

Received 18 May 2017; Accepted 1 August 2017; Published 30 August 2017

Academic Editor: Xiaofeng Zhou

Copyright © 2017 Zhixiang Deng and Meng Zhang. This is an open access article distributed under the Creative Commons Attribution License, which permits unrestricted use, distribution, and reproduction in any medium, provided the original work is properly cited.

The absence of Raman and unique pressure-tunable dispersion is the characteristic feature of gas-filled photonic crystal fiber (PCF), and its zero dispersion points can be extended to the near-infrared by increasing gas pressure. The generation of dispersive wave (DW) in the normal group velocity dispersion (GVD) region of PCF is investigated. It is demonstrated that considering the self-steepening (SS) and introducing the chirp of the initial input pulse are two suitable means to control the DW generation. The SS enhances the relative average intensity of blue-shift DW while weakening that of red-shift DW. The required propagation distance of DW emission is markedly varied by introducing the frequency chirp. Manipulating DW generation in gas-filled PCF by the combined effects of either SS or chirp and three-order dispersion (TOD) provides a method for a concentrated transfer of energy into the targeted wavelengths.

1. Introduction

The high design flexibility of photonic crystal fibers has attracted the attention of many researchers in recent decade [1]. Kagomé-lattice hollow-core PCF reported in 2002 represents a milestone in the development of microstructured fibers [2]. It demonstrates numerous additional significance properties by filling its hollow core with gas [3]. The non-linearity and the GVD can be remarkably controlled by adjusting gas pressure or replacing of gas species [3, 4]. The Raman-related effect disappears when the hollow core is filled with high pressure monatomic gases such as Ar, also the zero GVD point of fiber can be artificially adjusted from the ultraviolet to the near-infrared [4]. These features highly increase the versatility of hollow-core PCF, which make it an ideal platform to investigate different nonlinear optical effects.

As we all know, optical spectrum broadening and broadband frequency conversion are inherent features for nonlinear optical processes [5]. Dispersive wave (DW), also called nonsolitonic radiation or Cherenkov radiation [6], is particularly important for supercontinuum generation, broadband

light sources, and broadband frequency conversion in fiber optics, and manipulating DW generation is a technique with a concentrated transfer of energy into a narrow spectral band. The generation of DW by intense optical pulses propagating, in particular, in photonic crystal fibers has been extensively studied in the past 30 years [6–9]. However, it has been originally presented at the background of the propagation of higher-order soliton. In that situation, higher-order soliton was propagated in the anomalous GVD regime which is generally perturbed by the third- and higher-order dispersion [10–13]. In our previous work, the roles of the self-steepening (SS) effect in the generation and controlling of DW in metamaterials are disclosed [14], and in photonic crystal fiber, the manipulation of DW by the frequency chirped is unfolded [15, 16].

In the time-domain, DW emission is described as the resonant amplification of a linear wave propagating with the same phase velocity as that of the soliton [17]. Recently, in the frequency-domain, phase-matched cascaded four-wave mixing (CFWM) is identified as the nonlinear origins of the DW generation process [18–20]. It was demonstrated that the DW emission is no longer thought to be the exclusive

of solitons because the dispersive wave can be emitted even when pumping in the normal dispersion regime in the presence of a zero GVD wavelength [21]. In this regime, the physical origin of DW emission, which is perturbed by high-order dispersion, is intimately related to the dispersive shock waves resulting from the nonlinearity overbalancing a weak second-order dispersion [22]. The expression of the detuned frequency of dispersive waves can be accurately determined by the phase-matching selection rules, which involve the velocity of the dispersive shock waves due to emerging from a gradient catastrophe [22–24]. The roles of high-order dispersions in the generation and controlling of DW are also exposed [24–26]. However, to the best of our knowledge, so far the effect of the self-steepening and initial frequency chirp on DW generation with pumping in normal dispersion regime has not been discussed yet.

In the present paper, we demonstrate that the controllable generation of DW with pumping in the normal GVD dispersion can be realized by two means: either considering the SS effect of fiber or introducing the frequency chirp of the initial input pulse. The paper is organized as follows. In the second section, the defocusing nonlinear Schrödinger equation (dNLSE) for ultrashort pulse propagation in gas-filled photonic crystal fibers with TOD and SS effect is introduced. In the third section, we discuss the controllable DW generation and reveal the roles of the SS effect in the red-shifted and blue-shifted DW generation. In the fourth section, the impact on the DW generation on the basis of the different frequency chirp of the initial input pulse is investigated. Finally, we summarize our results.

2. Numerical Model

To technically elucidate the mechanism of resonant dispersive wave emission, our numerical model is based on the following normalized form of the defocusing nonlinear Schrödinger equation with the Raman term removed [27]:

$$\frac{\partial U}{\partial \xi} + \frac{i}{2} \frac{\partial^2 U}{\partial \tau^2} - \frac{\delta_3}{6} \frac{\partial^3 U}{\partial \tau^3} = iN^2 \left(1 + is \frac{\partial}{\partial \tau} \right) (|U|^2 U). \quad (1)$$

Note that the Raman scattering effect is absent in the noble gas-filled PCF such as Ar considered here. We have introduced the normalized variables $\tau = (t - z \cdot v_g^{-1})/T_0$, $\xi = z/L_{d_2}$, and $U = A/\sqrt{P_0}$, where T_0 is the duration of the launched pulse, P_0 is the power of the input field, v_g^{-1} is the group velocity at the central frequency ω_0 , and $L_{d_m} = T_0^m/\beta_m$ is the m th-order dispersion length and $L_{nl} = (\gamma P_0)^{-1}$ is the nonlinear length. Note that the defocusing feature arises from the assumption of the normal group velocity dispersion and nonlinear coefficient $\gamma > 0$. $N^2 = L_{d_2}/L_{nl}$ and $\delta_3 = L_{d_2}/L_{d_3}$ represent the normalized nonlinear coefficient and the normalized three-order dispersion coefficient, respectively. The nonlinear term in the right-hand side of (1) consists of the Kerr effect term $N^2|U|^2U$ and the shock derivative term $sN^2\partial(|U|^2U)/\partial\tau$, which gives rise to a frequency-dependent nonlinear coefficient. However, in our numerical simulation, the dispersion expansion can be truncated to the first correction to GVD, that is, third-order

dispersion, whereas all the higher-order dispersive terms can be safely neglected.

To quantify ensemble frequency changes of the DW during propagation process, we introduce the intensity-weighted central frequency of the DW as a function of propagation distance z [28]:

$$\langle \omega_{\text{DW}}(z) \rangle = \frac{\int_{\omega_a}^{\omega_b} \omega |A_{\text{DW}}(\omega, z)| d\omega}{\int_{\omega_a}^{\omega_b} |A_{\text{DW}}(\omega, z)| d\omega}. \quad (2)$$

Dispersion effects are described by the first term on the right-hand side of (1), where the range of integration (from ω_a to ω_b) is selected to be no more than -30 dB compared to the maximum intensity of the DW and $|A_{\text{DW}}|^2$ represents a function of the spectral intensity of the DW with propagation distance.

In order to obtain more intuitive information of the intensity distribution of DW, the performance of the continuum spectral distribution is characterized by the decibel scale of the relative intensity [29]

$$I(\omega, z) = 10 \lg \left(\frac{|A(\omega, z)|^2}{\max |A(\omega, z)|^2} \right) \quad (3)$$

and the relative average intensity of DW

$$\eta(z) = 10 \lg \left(\frac{\int_{\omega_a}^{\omega_b} |A(\omega, z)|^2 d\omega}{\int_{-\infty}^{\infty} |A(\omega, z)|^2 d\omega} \right). \quad (4)$$

The decibel scale used here permits us to clearly show the low-intensity radiation. However, if the intensity spectrum is presented in the form $|A(\omega, z)|^2 / \max |A(\omega, z)|^2$, its value is so small that can be submerged with the background of the strong pulse.

3. Manipulating the Dispersive Wave Generation by Self-Steepening Effect

It was well-known that the SS effect in gas-filled photonic crystal fiber can not be ignored in practice [4]. The pulse propagating in the normal dispersion regime is also affected by the higher-order dispersion and nonlinear terms. Thus, the combined effects of the SS and TOD on the DW generation should be discussed.

To discuss the DW generation in the fiber, we employ the standard split step Fourier method to solve the dNLSE numerically. In the numerical simulation, the normalized input pulse $U(0, \tau) = \text{sech}(\tau)$ is employed. For convenience, we only consider the DW generation under the condition of $N^2 = 200$. The reason for the selection can be that efficient generation of DWs from a pump in the normal GVD region typically requires the nonlinear length of the pump to be much shorter than the dispersion length of the pump. To gain a physical understanding of the effects, the loss of fiber is neglected. If not otherwise specified, only the normal GVD is considered.

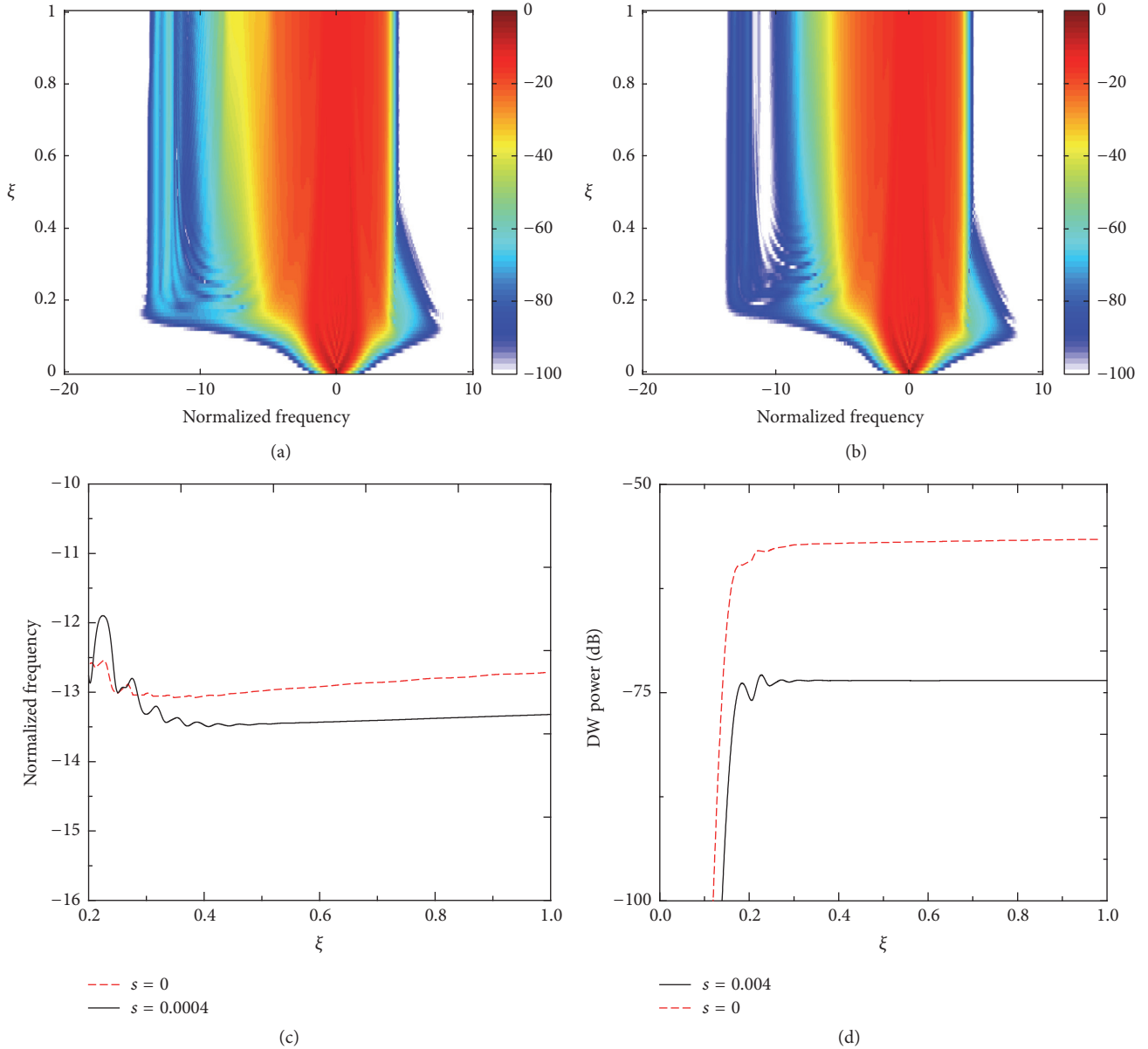


FIGURE 1: Simulate spectrum of a hyperbolic secant pulse propagating in the normal dispersion regime at the different SS coefficients, (a) $s = 0$, (b) $s = 0.004$, where $\delta_3 = 0.0267$, $N^2 = 200$. Central frequency (c) and relative average intensity (d) of the red-shift DW as a function of normalized propagation distance, where $s = 0$ (red dashed curve) and $s = 0.004$ (dark solid curve).

3.1. Dispersive Wave Generation for Positive Dispersion Slope. In the normal GVD of gas-filled PCF, DW emitted by dispersive shock waves owing to the positive dispersion slope (i.e., the positive TOD) will be frequency downshifted with respect to the pump. Therefore, it is called red-shift DW.

Figure 1 shows how the self-steepening effect influences the red-shift DW generation; here the positive TOD ($\delta_3 = 0.0267$) is considered. In Figures 1(a) and 1(b), we plot the spectral evolution of the pulse as a function of normalized propagation distance when the self-steepening effect is switched off (i.e., set $s = 0$) and included (i.e., set $s = 0.004$), respectively. Obviously, in the initial stages of propagation, the spectrum of the pump pulse displays strong and symmetrical broadening due to self-phase-modulation-induced

pulse compresses in the presence of weak normal dispersion, but as the spectral tail of the broadened pulse overlaps with the phase-matched frequency, the occurrence of resonant energy transfer process can be seen. As the propagating distance increases, the DW emitted by dispersive shock waves begins to emerge in the red-shifted band. As can be seen by comparing Figure 1(a) with Figure 1(b), the SS effect is important for red-shift DW generation. For the two cases that the SS effect is excluded/included, the evolutions of the output spectra have the following characteristics: to begin with, the pulse spectra become narrow. When the SS effect is included, the spectrum narrowing is obvious. Therefore, this is a disadvantage to the supercontinuum generation. Secondly, the central frequency of the red-shift DW moves

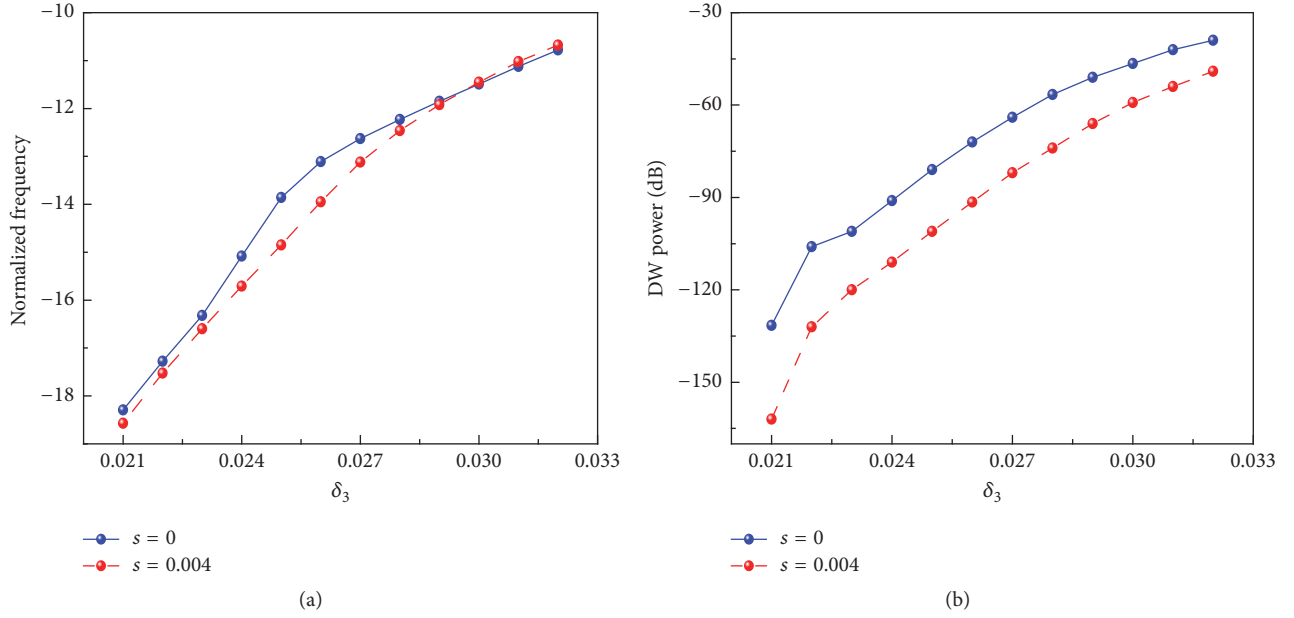


FIGURE 2: Central frequency (a) and relative average intensity (b) of the red-shift DW plotted as a function of TOD coefficient δ_3 , where $s = 0$ (blue filled circles lines) and $s = 0.004$ (red dashed circles lines).

away from the spectral body of the residual pump pulse. In other words, the SS effect leads to the increase of the frequency detuning $\Delta\nu$ from the pump. The cause of this result is that the frequency of DW is determined by the phase-matched condition associated with the nature group velocity, but SS increases the group velocity at resonant frequency eventually because it affects the group velocity in an intensity dependent fashion [30]. As can be seen from Figure 1(c), the shifting is not remarkable, which indicates that the influences of the SS effect on the frequency shifts of red-shift DW are less important than TOD. Finally, one conspicuous observation is that the relative average intensity of red-shift DW is weakened. The spectral intensity of the DW is related to the strength of the pump spectrum at the phase-matched frequency [31, 32]. Since the SS effect asymmetrically weakens the spectrum toward the red, the efficiency of DW generation dropped. As shown in Figure 1(d), the relative average intensity of red-shift DW is -56 dB when the SS effect set $s = 0$ and drops to -75 dB when the SS effect set $s = 0.004$.

To fully understand the impact of the SS effect on the red-shift DW generation, we will consider the manipulatable generation of red-shift DW by the self-steepening effect switched off or included under the different positive TOD coefficient. Next, we discuss the weighted central frequency and relative average intensity as the function of the TOD coefficient, as shown in Figure 2. We see that for the red-shift DW the frequency detuning $\Delta\nu$ from the pump decreases and the average intensity enhances as δ_3 increases. In Figure 2, it also shows the influence of SS coefficient on DWs. For $\delta_3 < 0.024$ or $\delta_3 > 0.028$, the influence of the SS coefficient on the frequency detuning can be neglected; however, in the range $0.024 < \delta_3 < 0.028$, the influence of the SS coefficient on the frequency detuning $\Delta\nu$ is significant. The average intensity of DWs is influenced by the SS effect distinctly; however, in

contrast to the case of without SS effect, the average intensity of DWs reduces to over 20 dB when the SS effect is included. Based on these analysis results, we reach the conclusion that the SS effect weakens the red-shift DW generation. For instance, when $\delta_3 = 0.032$, the average intensity is about -40 dB if SS effect is switched off; however, it can be weakened by the SS coefficient to -55 dB at $s = 0.004$.

3.2. Dispersive Wave Generation for Negative Dispersion Slope. The former section just considers the role of the positive TOD parameter in the DW generation. Indeed, we can also obtain the negative value of TOD parameter by varying either the pressure or temperature of the filling gas in the photonic crystal fibers. The case is that the dispersive wave appears to be located at higher frequencies compared with our pump pulse; therefore, it is the so-called the blue-shift DW. Next, we turn to the discussion about the role of the negative TOD combined with SS effect in the blue-shift DW generation. For $\delta_3 = -0.0267$, Figures 3(a) and 3(b) show the contour of the injected pulse when the SS effect is switched off and included, respectively. In stark contrast to the result of the positive TOD, the evolutions of the output spectra based on whether the SS effect is included or not have the distinct feature as follows: firstly, the pulse spectra become narrow. When the SS effect is included, the spectrum broadening is obvious. Therefore, this is favorable to the supercontinuum generation. Next, the central frequency of blue-shift DW moves toward the spectral body of the residual pump pulse. In other words, for blue-shift DW, the frequency detuning $\Delta\nu$ from the pump pulse is decreased. Reasonable explanation is that the SS effect alters the group velocity associated with the expression of the phase-matching condition. As can be seen from Figure 3(c), at $\xi = 1$, the average location of blue-shift DW when the SS effect is ignored is 0.3 above that

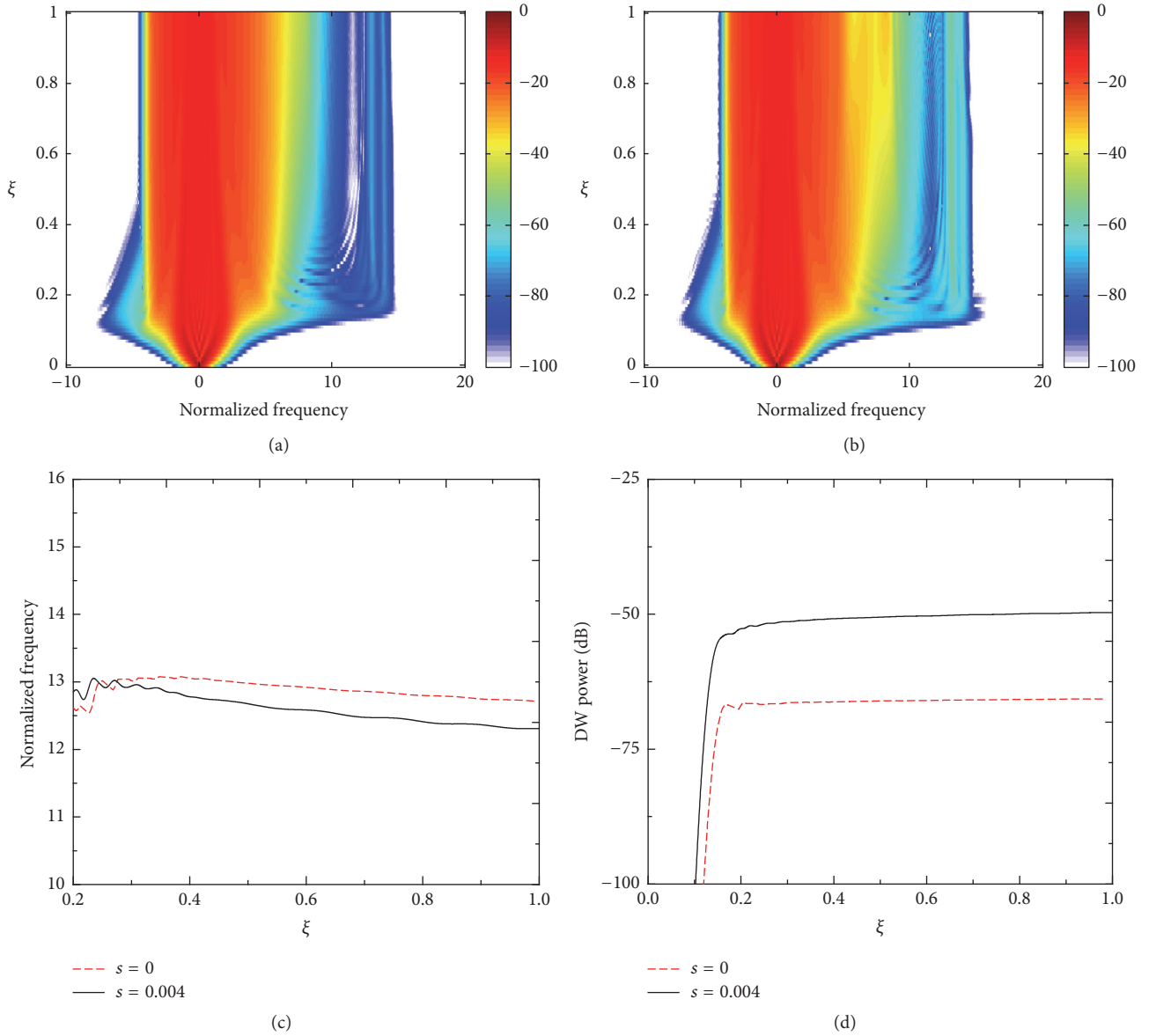


FIGURE 3: Simulate spectrum of a hyperbolic secant pulse propagating in the normal dispersion regime at the different SS coefficients, (a) $s = 0$ and (b) $s = 0.004$, where $\delta_3 = -0.0267$ and $N^2 = 200$. Central frequency (c) and the relative average intensity (d) of the blue-shift DW as a function of normalized propagation distance, where $s = 0$ (red dashed curve) and $s = 0.004$ (dark solid curve).

of blue-shift DW when it is taken into account. Ultimately, the relative average intensity of blue-shift DW is enhanced. Since the effect of SS asymmetrically enhances the spectrum toward the blue, it is improving the efficiency of blue-shift DW generation. As shown in Figure 3(d), the relative average intensity of blue-shift DW is -67 dB when the SS effect is switched off, while it increases to -49 dB when it is included.

To further get a thorough understanding of the influence of the SS effect on the blue-shift DW generation, Figure 4 indicates, on the basis of the two cases of the SS effect are included or not, the frequency detuning and relative average intensity of the blue-shift DW plotted as a function of negative TOD coefficient. In both cases, as can be seen from Figure 4(a), the blue-shift DW shifts to lower frequency

with the increasing $|\delta_3|$. However, note that the frequency detuning $\Delta\nu$ of the blue-shift DW in the presence of the SS effect is lower than that of the DW neglecting the SS effect, especially when $|\delta_3|$ is placed in the range $0.022 < |\delta_3| < 0.027$. As shown in Figure 4(b), the relative average intensity of DWs enhanced as TOD coefficient $|\delta_3|$ increases; nonetheless, it is noted that the amount of relative average intensity of the DW when the SS effect is neglected is about 20 dB below that of the DW when it is included. These results indicate that the relative average intensity of blue-shift DW is enhanced, rather weakened, and the average position of blue-shift DW can be shifted slightly to the spectral body of the residual pump pulse via considering the SS effect.

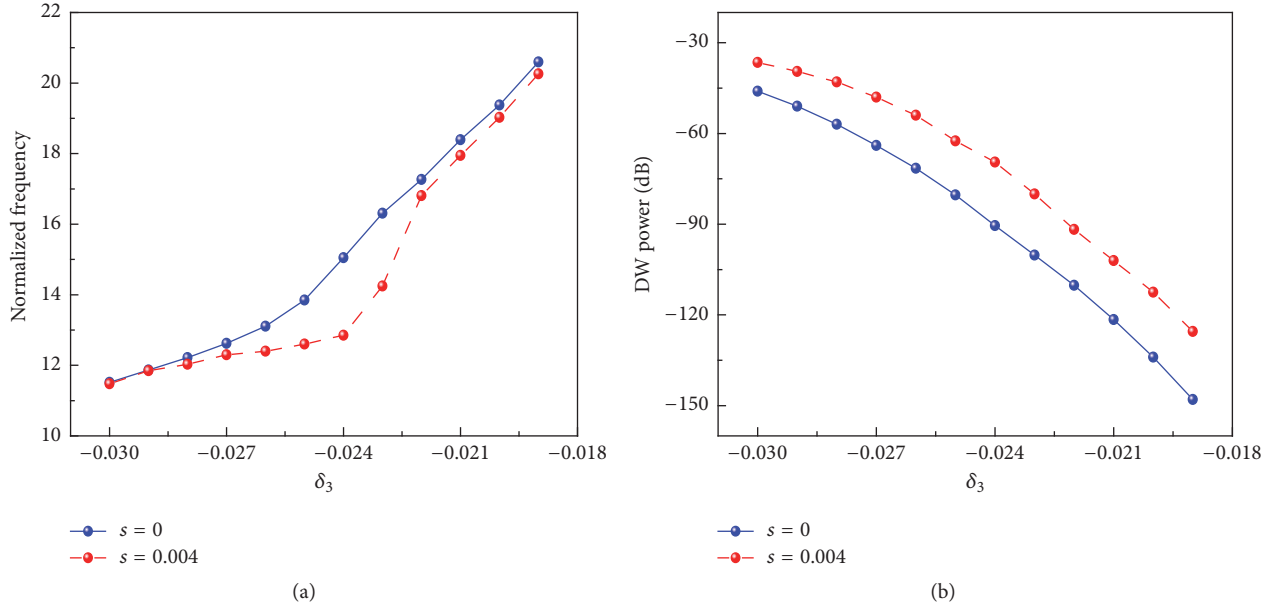


FIGURE 4: Central frequency (a) and relative average intensity (b) of the blue-shift DW plotted as a function of TOD coefficient δ_3 , where $s = 0$ (blue filled circles lines) and $s = 0.004$ (red dashed circles lines).

4. Manipulating the Dispersive Wave Generation by Frequency Chirp

From the realistic perspective, pulses emitted from laser sources are often chirped [33]. Therefore, apart from the self-steepening effect of dispersive waves emission discussed above, good understanding of the frequency chirp influence on dispersive waves emission is of great importance. In the section, we consider in detail the effect of initial frequency chirp on DW generation. In order to understand the pulse evolution, that is, the spectral expansion and DW generation, under the influence of pulse chirp we numerically simulated the pulse amplitude propagation using a split step Fourier simulation tool, as well. In order to highlight the role of frequency chirp on the DW generation, the SS effect in the next discussion is switched off. In our simulation, the initial incident pulse is assumed to have a normalized form of hyperbolic secant field profile:

$$U(0, \tau) = \text{sech}(\tau) \exp\left(-\frac{iC\tau^2}{2}\right), \quad (5)$$

where C is the parameter representing the initial linear frequency chirp. We started our simulations to verify this qualitative behavior.

4.1. Dispersive Wave Generation for Positive Dispersion Slope. For the sake of convenience, we supposed that the positive TOD coefficient is fixed at $\delta_3 = 0.0267$, that is, set $\delta_3 = 0.0267$. To better understand the effects of initial chirps, a series of spectral evolutions for different input chirps is displayed in Figure 5. Comparing Figures 5(a)–5(c), it is observed that the frequency chirp is vital to the DW generation. With the frequency chirp changing from negative

to positive, the evolutions of the output spectra have the following characteristics: firstly, the distance at which the spectral broaden to its maximum value is modified. In other words, the propagation distance which DW generation required is changed. If no chirp is applied, the initial pulse spectrum can be seen to approach a maximum spectrum width within the first $0.15L_{d_2}$ of propagation distance (see Figure 5(b)). If a negative input chirp is applied, the needed distance at which the DW generated is earlier compare to that of unchirped pulse [see black dash line in Figure 5(a)]. More interesting, Figure 5(c) shows that the initial pulse spectrum approach a maximum point is deferred when a positive input chirp is applied. The reason for this is that, for positive chirp coefficient, the pulse duration increases with distance due to $\beta_2 C > 0$. The decrease in intensity then lessens the nonlinear effects, leading to slow the rate of bandwidth broadening, whereas for a negative chirp coefficient, the pulse duration first decreases until it reaches minimum value at a distance due to $\beta_2 C < 0$. Such, the increase in intensity then enhances the nonlinear effects further, resulting in speed up the rate of bandwidth broadening. This consideration explains why the positive chirped pulse emits the DW later, or the negative chirped pulse emits the DW earlier compare to the case of unchirped pulse.

Secondly, the frequency centre of DW during the propagation is markedly changed. As can be seen from Figure 6(a), in the initial stage of the DW generation, the frequency detuning between the DW and the pump pulse gradually decrease when the parameter values C of the initial input chirp increased from -2 to 2 (note that we only draw the evolution of centre frequency of DW with propagation distance beyond $0.2L_{d_2}$ because of no DW generation in the earlier propagation). With the further increase of the propagation distance, the central frequency of DW becomes

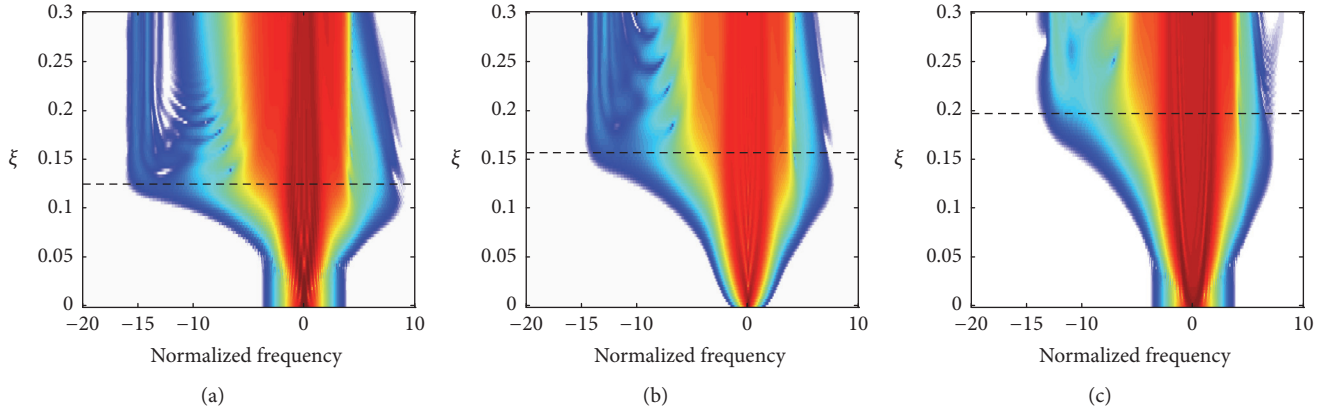


FIGURE 5: Pulse spectral evolution during propagation for different input pulse chirps, (a) $C = -2$, (b) $C = 0$, and (c) $C = 2$ as the sign of TOD is positive. The black horizontal dash line indicates the position at which the maximum spectral broadening occurs, that is, the DW generated.

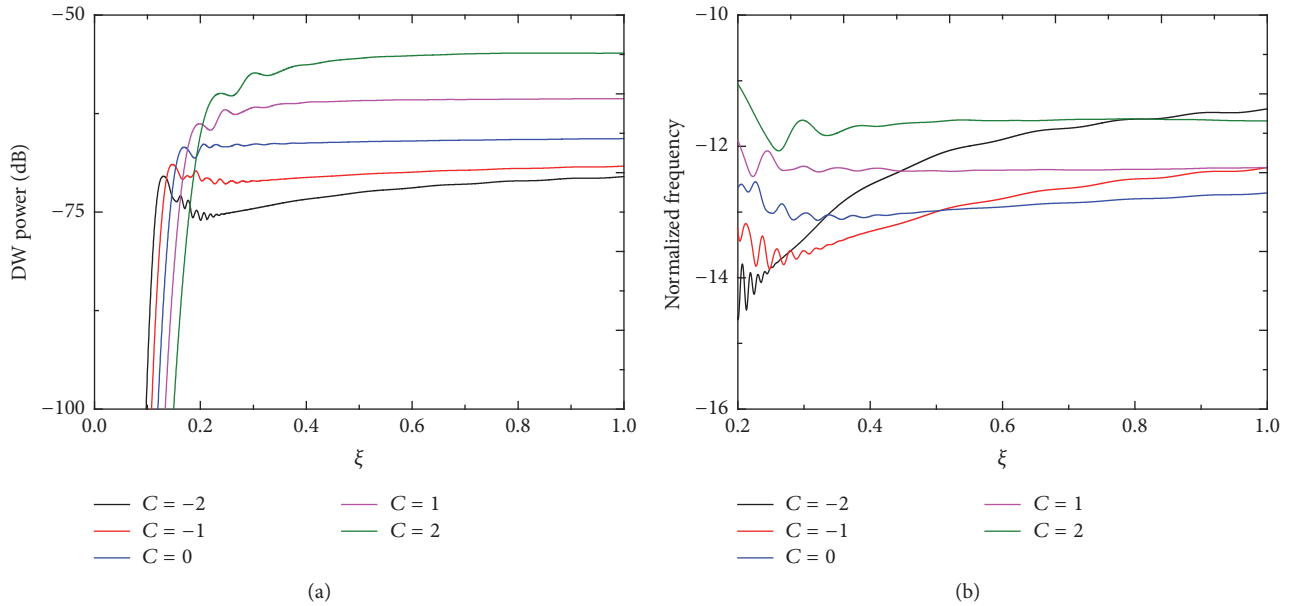


FIGURE 6: Evolution of the red-shift DW of relative average power (a) and central frequency (b) along the propagation distance, with different chirp but the sign of TOD is positive: dark solid curves $C = -2$; red solid curves $C = -1$; blue solid curves $C = 0$; magenta solid curves $C = 1$; olive solid curves $C = 2$.

saturated quickly when a positive input chirp is applied; however, for a negative input chirp, the central frequency of DW can be seen to shift gradually toward the spectral body of residual pump, and eventually, the frequency detuning $\Delta\nu$ from the pump pulse will be less than the case in the absence of the initial frequency chirp.

Finally, the relative average intensity of DW can be either enhanced or reduced. The dependence of relative average power on propagation distance is displayed in Figure 6(b) for a set of input pulse chirp parameters. From the figure, it is apparent that, in contrast to that of the unchirped input pulse, the positive chirp enhance the average intensity of the DW while the negative chirp weakens that of the DW. However, regardless of the sign of the initial input chirps, the average intensity of DW becomes saturated rapidly along fiber propagation.

4.2. Dispersive Wave Generation for Negative Dispersion Slope.

For completeness, in the following sections we considered the case of negative dispersion slope, that is, negative TOD. In order to better compare with the case of positive TOD discussed above, we will continue to the fixed TOD coefficient and set $\delta_3 = -0.0267$. The simulated optical spectral evolution of the pulse with three different chirp parameters is shown in Figures 7(a)–7(c). The required distance at which the DW emitted, the central frequency of DW and the relative average intensity of the DW are obviously altered as the frequency chirp is applied. More interesting, the transformation law plotted in Figure 8 is almost the same as the case of positive dispersion slope. This indicates that the effect of frequency chirp to blue-shift DW will be the same as that of red-shift DW. This provides a means to tune the DW emission by varying the initial chirp of the input pulse.

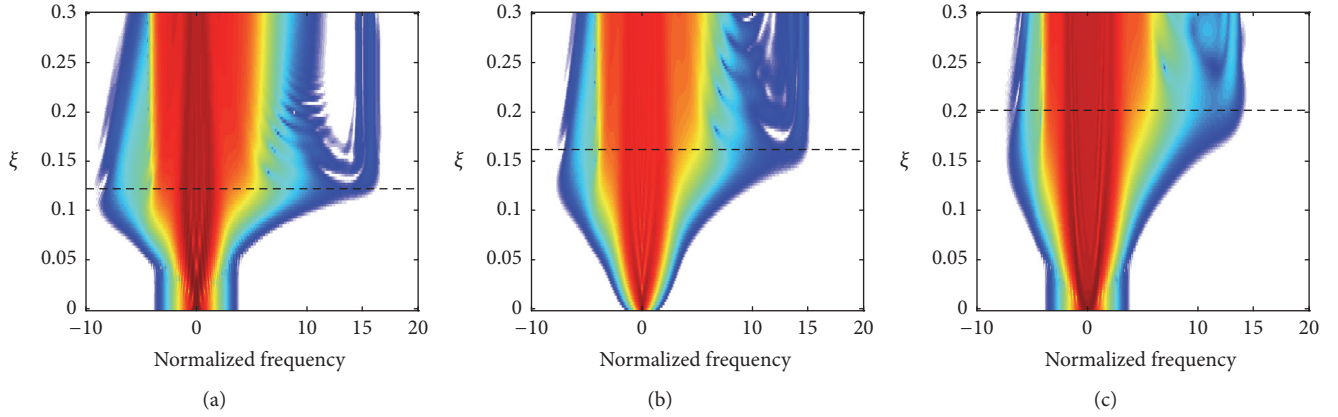


FIGURE 7: Density plots of spectral evolution during propagation for different input pulse chirps, (a) $C = -2$, (b) $C = 0$, and (c) $C = 2$ when the sign of TOD is negative. The black horizontal dash line indicates the position at which the maximum spectral broadening occurs, that is, the DW generated.

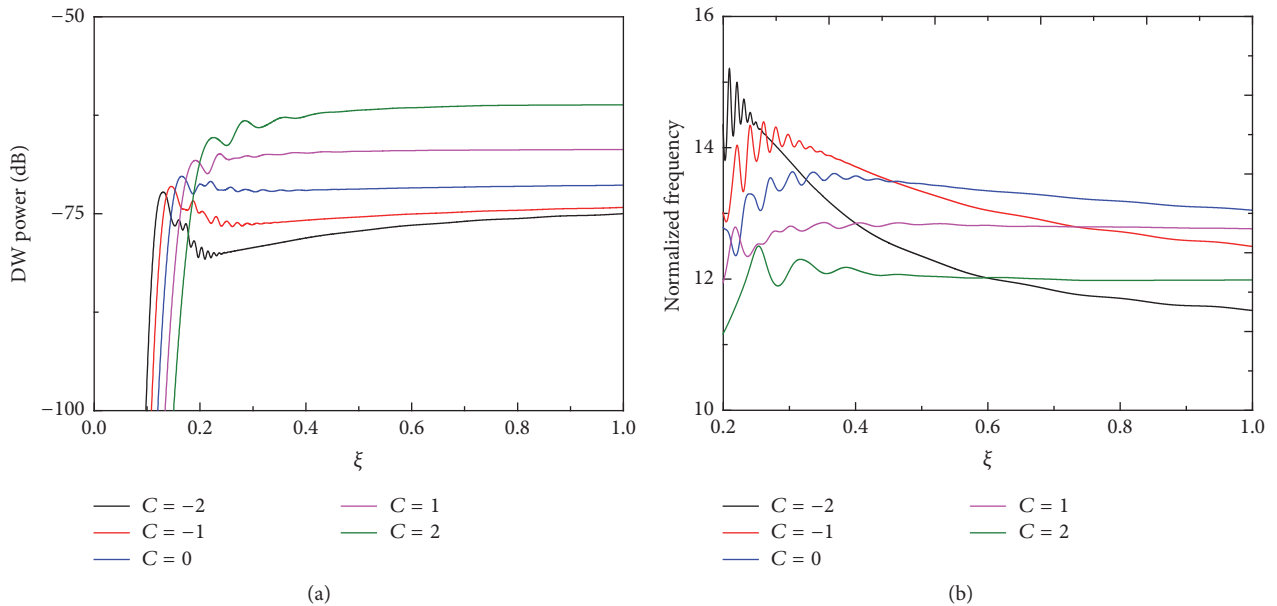


FIGURE 8: Evolution of the blue-shift DW of central frequency (a) and relative average intensity (b) along the propagation distance, with different chirp but the sign of TOD is negative: dark solid curves $C = -2$; red solid curves $C = -1$; blue solid curves $C = 0$; magenta solid curves $C = 1$; olive solid curves $C = 2$.

5. Conclusions

In summary, we have presented numerical results describing the nonlinear propagation of the ultrashort pulse in normal dispersion region in gas-filled photonic crystal fiber. When it satisfies the phase-matching condition at the different signs of dispersion slope, it will produce red-shift or blue-shift DW relative to the input pump pulse. Our results suggest that the properties of red-shifted or blue-shifted DW can be markedly manipulated by the SS effect. For the red-shifted DW, the relative average intensity of DW decreases rapidly and the central frequency of DW downshifts slightly when the SS effect is considered. However, the results are diametrically opposite to the case of blue-shifted DW. The effect of initial

chirp on the DW generation is also studied. Regardless of the red-shifted or blue-shifted DW, the negative chirp can speed up the DW generation while the positive chirp will slow it down. Meanwhile, the frequency chirp leads to marked changing of the relative average power and central frequency of DW, as well. Manipulating DW generation in gas-filled PCF by the combined effects of either SS or chirp and three-order dispersion provides an alternative route for an efficient and concentrated transfer of energy into the desired spectral bands.

Conflicts of Interest

The authors declare that they have no conflicts of interest.

Acknowledgments

This work was supported by the National Natural Science Foundation of China [Grant nos. 61571183, 61505122] and the Guangdong Natural Science Foundation (Grant no. 2014A030310279).

References

- [1] P. S. J. Russell, "Photonic crystal fibres," *Science*, vol. 299, no. 5605, pp. 358–362, 2003.
- [2] F. Benabid, J. C. Knight, G. Antonopoulos, and P. S. J. Russell, "Stimulated Raman scattering in hydrogen-filled hollow-core photonic crystal fiber," *Science*, vol. 298, no. 5592, pp. 399–402, 2002.
- [3] P. S. J. Russell, P. Hölzer, W. Chang, A. Abdolvand, and J. C. Travers, "Hollow-core photonic crystal fibres for gas-based nonlinear optics," *Nature Photonics*, vol. 8, no. 4, pp. 278–286, 2014.
- [4] J. C. Travers, W. Chang, J. Nold, N. Y. Joly, and P. S. J. Russell, "Ultrafast nonlinear optics in gas-filled hollow-core photonic crystal fibers," *Journal of the Optical Society of America B: Optical Physics*, vol. 28, no. 12, pp. A11–A26, 2011.
- [5] J. M. Dudley, G. Genty, and S. Coen, "Supercontinuum generation in photonic crystal fiber," *Reviews of Modern Physics*, vol. 78, no. 4, pp. 1135–1184, 2006.
- [6] N. Akhmediev and M. Karlsson, "Cherenkov radiation emitted by solitons in optical fibers," *Physical Review A*, vol. 51, no. 3, pp. 2602–2607, 1995.
- [7] P. K. A. Wai, H. H. Chen, and Y. C. Lee, "Radiations by solitons at the zero group-dispersion wavelength of single-mode optical fibers," *Physical Review A*, vol. 41, no. 1, pp. 426–439, 1990.
- [8] P. K. A. Wai, C. R. Menyuk, Y. C. Lee, and H. H. Chen, "Nonlinear pulse propagation in the neighborhood of the zero-dispersion wavelength of monomode optical fibers," *Optics Letters*, vol. 11, no. 7, pp. 464–466, 1986.
- [9] V. I. Karpman, "Radiation by solitons due to higher-order dispersion," *Physical Review E. Statistical, Nonlinear, and Soft Matter Physics*, vol. 47, no. 3, pp. 2073–2082, 1993.
- [10] H. Yang, F. Han, H. Hu, W. Wang, and Q. Zeng, "Spectral-temporal analysis of dispersive wave generation in photonic crystal fibers of different dispersion slope," *Journal of Modern Optics*, vol. 61, no. 5, pp. 409–414, 2014.
- [11] K. M. Hilligsøe, H. N. Paulsen, J. Thøgersen, S. R. Keiding, and J. J. Larsen, "Initial steps of supercontinuum generation in photonic crystal fibers," *Journal of the Optical Society of America B: Optical Physics*, vol. 20, no. 9, pp. 1887–1893, 2003.
- [12] S. Roy, S. K. Bhadra, and G. P. Agrawal, "Perturbation of higher-order solitons by fourth-order dispersion in optical fibers," *Optics Communications*, vol. 282, no. 18, pp. 3798–3803, 2009.
- [13] J. N. Elgin, T. Brabec, and S. M. J. Kelly, "A perturbative theory of soliton propagation in the presence of third order dispersion," *Optics Communications*, vol. 114, no. 3–4, pp. 321–328, 1995.
- [14] S. Hill, C. E. Kuklewicz, U. Leonhardt, and F. König, "Evolution of light trapped by a soliton in a microstructured fiber," *Optics Express*, vol. 17, no. 16, pp. 13588–13601, 2009.
- [15] X. Fu, L. Qian, S. Wen, and D. Fan, "Nonlinear chirped pulse propagation and supercontinuum generation in microstructured optical fibre," *Journal of Optics A: Pure and Applied Optics*, vol. 6, no. 11, pp. 1012–1016, 2004.
- [16] D. Lei, H. Dong, S. Wen, and H. Yang, "Manipulating dispersive wave generation by frequency chirp in photonic crystal fibers," *Journal of Lightwave Technology*, vol. 27, no. 20, pp. 4501–4507, 2009.
- [17] A. V. Husakou and J. Herrmann, "Supercontinuum generation of higher-order solitons by fission in photonic crystal fibers," *Physical Review Letters*, vol. 87, no. 20, Article ID 203901, 2001.
- [18] M. Erkintalo, Y. Q. Xu, S. G. Murdoch, J. M. Dudley, and G. Genty, "Cascaded phase matching and nonlinear symmetry breaking in fiber frequency combs," *Physical Review Letters*, vol. 109, no. 22, Article ID 223904, 2012.
- [19] K. E. Webb, M. Erkintalo, Y. Xu et al., "Nonlinear optics of fibre event horizons," *Nature Communications*, vol. 5, article no. 4969, 2015.
- [20] K. E. Webb, M. Erkintalo, Y. Q. Xu, G. Genty, and S. G. Murdoch, "Efficiency of dispersive wave generation from a dual-frequency beat signal," *Optics Letters*, vol. 39, no. 20, pp. 5850–5853, 2014.
- [21] K. E. Webb, Y. Q. Xu, M. Erkintalo, and S. G. Murdoch, "Generalized dispersive wave emission in nonlinear fiber optics," *Optics Letters*, vol. 38, no. 2, pp. 151–153, 2013.
- [22] M. Conforti and S. Trillo, "Dispersive wave emission from wave breaking," *Optics Letters*, vol. 38, no. 19, pp. 3815–3818, 2013.
- [23] J. Fatome, C. Finot, G. Millot, A. Armaroli, and S. Trillo, "Observation of optical undular bores in multiple four-wave mixing," *Physical Review X*, vol. 4, no. 2, Article ID 021022, 2014.
- [24] M. Conforti, F. Baronio, and S. Trillo, "Resonant radiation shed by dispersive shock waves," *Physical Review A - Atomic, Molecular, and Optical Physics*, vol. 89, no. 1, Article ID 013807, 2014.
- [25] S. Malaguti, M. Conforti, and S. Trillo, "Dispersive radiation induced by shock waves in passive resonators," *Optics Letters*, vol. 39, no. 19, pp. 5626–5629, 2014.
- [26] S. Malaguti, G. Bellanca, and S. Trillo, "Dispersive wave-breaking in coherently driven passive cavities," *Optics Letters*, vol. 39, no. 8, pp. 2475–2478, 2014.
- [27] N. Y. Joly, J. Nold, W. Chang et al., "Bright spatially coherent wavelength-tunable deep-UV laser source using an Ar-filled photonic crystal fiber," *Physical Review Letters*, vol. 106, no. 20, Article ID 203901, 2011.
- [28] C. Liu, E. J. Rees, T. Laurila, S. Jian, and C. F. Kaminski, "Periodic interactions between solitons and dispersive waves during the generation of noncoherent supercontinuum radiation," *Optics Express*, vol. 20, no. 6, pp. 6316–6324, 2012.
- [29] D. A. Korobko, O. G. Okhotnikov, D. A. Stoliarov, A. A. Sysolyatin, and I. O. Zolotovskii, "Broadband infrared continuum generation in dispersion shifted tapered fiber," *Journal of the Optical Society of America B: Optical Physics*, vol. 32, no. 4, pp. 692–700, 2015.
- [30] G. P. Agrawal, *Nonlinear Fiber Optics*, Academic, New York, 4th edition, 2007.
- [31] T. Marest, C. Mas Arabi, M. Conforti et al., "Emission of dispersive waves from a train of dark solitons in optical fibers," *Optics Letters*, vol. 41, no. 11, pp. 2454–2457, 2016.
- [32] Y. Chen, G. Jiang, S. Chen et al., "Mechanically exfoliated black phosphorus as a new saturable absorber for both Q-switching and mode-locking laser operation," *Optics Express*, vol. 23, no. 10, pp. 12823–12833, 2015.
- [33] S. Chen, L. Miao, X. Chen et al., "Few-layer topological insulator for all-optical signal processing using the nonlinear kerr effect," *Advanced Optical Materials*, vol. 3, no. 3, pp. 1769–1778, 2015.

Research Article

Optical Orbital Angular Momentum Demultiplexing and Channel Equalization by Using Equalizing Dammann Vortex Grating

Mingyang Su, Junmin Liu, Yanliang He, Shuqing Chen, and Ying Li

International Collaborative Laboratory of 2D Materials for Optoelectronics Science and Technology and Key Laboratory of Optoelectronic Devices and Systems of Ministry of Education and Guangdong Province, Shenzhen University, Shenzhen 518060, China

Correspondence should be addressed to Shuqing Chen; shuqingchen@szu.edu.cn

Received 21 April 2017; Accepted 23 May 2017; Published 21 June 2017

Academic Editor: Ashok Chatterjee

Copyright © 2017 Mingyang Su et al. This is an open access article distributed under the Creative Commons Attribution License, which permits unrestricted use, distribution, and reproduction in any medium, provided the original work is properly cited.

A novel equalizing Dammann vortex grating (EDVG) is proposed as orbital angular momentum (OAM) multiplexer to realize OAM signal demultiplexing and channel equalization. The EDVG is designed by suppressing odd diffraction orders and adjusting the grating structure. The light intensity of diffraction is subsequently distributed evenly in the diffraction orders, and the total diffraction efficiency can be improved from 53.22% to 82%. By using the EDVG, OAM demultiplexing and channel equalization can be realized. Numerical simulation shows that the bit error rate (BER) of each OAM channel can decrease to 10^{-4} when the bit SNR is 22 dB, and the intensity is distributed over the necessary order of diffraction evenly.

1. Introduction

Vortex beam is a structured light beam that can carry orbital angular momentum (OAM) and possess helical phase-front. The spiral phase wavefront beam can be represented by using a phase function $\exp(il\theta)$, and each photon can carry orbital angular momentum lh [1]. OAM can be used in photonic computer [2], quantum information processing [3–5], optical communication [6], and so forth. Especially for communication, OAM can be used as a new freedom degree of modulation/multiplexing to further increase the transmission capacity and capacity density [7]. The OAM free space optical communication, therefore, is one of the hot topics of research in recent years [7–12]. In 2010, Awaji et al. first applies the OAM multiplex technology into optical communication [11]. In addition, in 2014, Huang et al. fuse OAM multiplexing together with PDM and WDM technology achieved 100 T bits/s transmission rate in free space optical communication [13]. One of the most important issues for OAM optical multiplex communication system is looking for a highly efficient multiplexing/demultiplexing method to realize the space separation of different OAM

states and achieve the channel equalization among different OAM channels.

There was evidence that the intensity of OAM beams will attenuate while propagating in the free space caused by the influence of atmosphere turbulence, and the signal degradation and fading will not equalize among different channels [6]. The most common way of demultiplexing OAM beams is the using of multiple optics beam-splitter and spiral phase plate. However, it is hard to realize OAM channel equalization, and complex system structure is required to achieve parallel detection [7, 11, 12]. The binary gratings combined with coordinate transformation are also used to separate and detect OAM beams, but it is hard to ensure the equilibrium of OAM channels [14]. According to the earlier work, it can be seen that the phase diffractive optical elements (DOEs) can be used to decompose the coherent light fields in terms of an orthogonal basis with angular harmonics [15–17]. Dammann vortex grating (DVG), such as DOEs, which combined Dammann grating and vortex phase diagram, can be used to separate different OAM in free space by different order of diffraction and shows ability to parallel separate multi-OAM beams [18]. By designing the changing point of

phase with 0.23191, 0.42520, and 0.52571, the DVG can be used to produce seven optical vortexes with different OAM states [19]. Researchers also found that the light intensity can be focused on the necessary order of diffraction by proper designing grating by using different change point of phase. However, the diffraction orders intensity is imbalanced, and a lot of light energy concentrates on the zero order, which could easily lead to BER disequilibrium among OAM channels.

In this paper, an equalizing Dammann vortex grating (EDVG) is proposed by suppressing the even and zero diffraction order, which can be used to realize the uniform regulation of diffracted light intensity. Theoretical and simulation results show that the diffraction angle of grating can be increased from 0.9251° to 1.8502° which indicated a larger separation among diffraction orders can be realized, and the total diffraction efficiency is improved from 53.22% to 82%. By using the EDVG as multiplexer to separate OAM beams, the bit error rate (BER) of each OAM channel can decrease

to 10^{-4} when the bit SNR is 22 dB, and the BER equilibrium among all OAM channels can be achieved effectively.

2. The Design of Equalizing Dammann Vortex Grating

Dammann vortex grating, which evolved from traditional Dammann grating, can be used to produce and separate optical vortex parallelly. Its transmission function can be written as [20]

$$T_{\text{DG}} = \sum_{m=-\infty}^{+\infty} C_m \exp \left[im \times \left(\frac{2\pi x}{T} \right) \right], \quad (1)$$

where m is the diffraction order and T is the period of grating. C_m is the coefficient of the m th diffraction order, and it can be expressed by

$$C_m = \begin{cases} \frac{-iT}{2m\pi} \left[1 + 2 \sum_{n=1}^{N-1} (-1)^n \exp(-i2\pi x_n) + (-1)^N \exp(-i2\pi m x_N) \right], & m \neq 0, \\ T \left[\sum_{n=1}^{N-1} (-1)^n x_N + (-1)^N x_N \right], & m = 0, \end{cases} \quad (2)$$

where $\{x_n\}$ are the normalized phase transition points with boundary values of $x_0 = 0$ and $x_N = 1$ and N is the total number of these transition points. Putting the vortex phase of charge l into formula, the transmission function of the DVG can be written as

$$T_{\text{DVG}} = \sum_{m=-\infty}^{+\infty} C_m \exp \left[im \times \left(\frac{2\pi x}{T} + l\theta \right) \right]. \quad (3)$$

The topological charge value for generated optical vortex is $m \times l$ in m -order of diffraction. Here, the changing point of phase with 0.23191, 0.42520, and 0.52571 can be used to design the DVG, and the grating could produce seven different optical vortexes. When $l = 1$, it can be used to generate the optical vortex with topologies of 0, ± 1 , ± 2 , and ± 3 . The phase structure of the EDVG is showed in Figure 1.

For Gauss beam, the light field distribution can be represented as

$$E(r, \theta, z) = \frac{A_0}{w(z)} \exp \left(\frac{-r^2}{w^2(z)} \right), \quad (4)$$

where w_0 is the waist radius at the propagation distance of $Z = 0$ m, $w(z)$ is the beam waist radius at the propagation distance of $Z > 0$ m, $z_R = \pi w_0^2 / \lambda$ is Rayleigh distance, and $k = 2\pi / \lambda$ is wave vector.

As the light beam is transmitted through the DVG and Fourier transformation for the output light was carried out, the obtained light field distribution can be represented as

$$E_{\text{DVG}}(r, \theta, z) = \text{FFT} \{ T_{\text{DVG}} \cdot E \}. \quad (5)$$

The light intensity distribution and normalized spectrum diagram are showed in Figure 2, where the optical working wavelength is $\lambda = 1550$ nm. Figure 2(a) shows the emergent light intensity distribution, the output light intensity is concentrated on the diffraction order of 0, ± 1 , ± 2 , and ± 3 , and the total number of the diffraction order is 7. And it should be noted that the light intensity distribution of different diffractions is disproportionate. The normalized spectrum diagram is showed in Figure 2(b). From Figure 2(b), the light intensity of zero-order diffraction is significantly higher than other diffraction orders. The light intensity of zero order is unhelpful or harmful for OAM optical communication, because it cannot be multiplexing/demultiplexing. The intensity increase in zero-order diffraction means the decrease in the other diffraction order, which results in the degraded BER in the optical communication. And, as showed in Figure 2(a), the light intensity at the diffraction order of ± 2 is significantly greater than the order of ± 1 and ± 3 , and this phenomenon will lead to the BER imbalance among OAM channels. Therefore, the most urgent problem that needs to be resolved, which DVG used for OAM demultiplexer, is how to suppress the zero-order diffraction and realize the equalization of intensity distribution. Here, we proposed a EDVG by suppressing the odd-order diffraction and applying the intensity equally among the order diffractions. As showed in Figure 2(c), the emergent light intensity almost focused on the order of diffraction of ± 1 and ± 2 . The topological charges of the generated optical vortexes are ± 1 and ± 3 , respectively, and the light intensities are nearly equal among different diffraction orders. The normalized spectrum diagram also

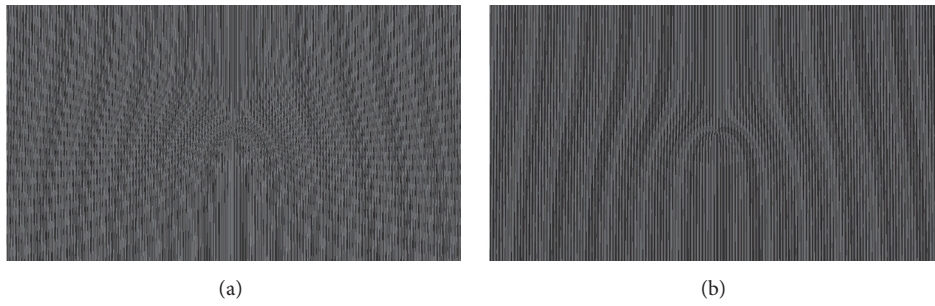


FIGURE 1: The phase structure of the Dammann vortex grating, (a) the original DVG and (b) the EDVG.

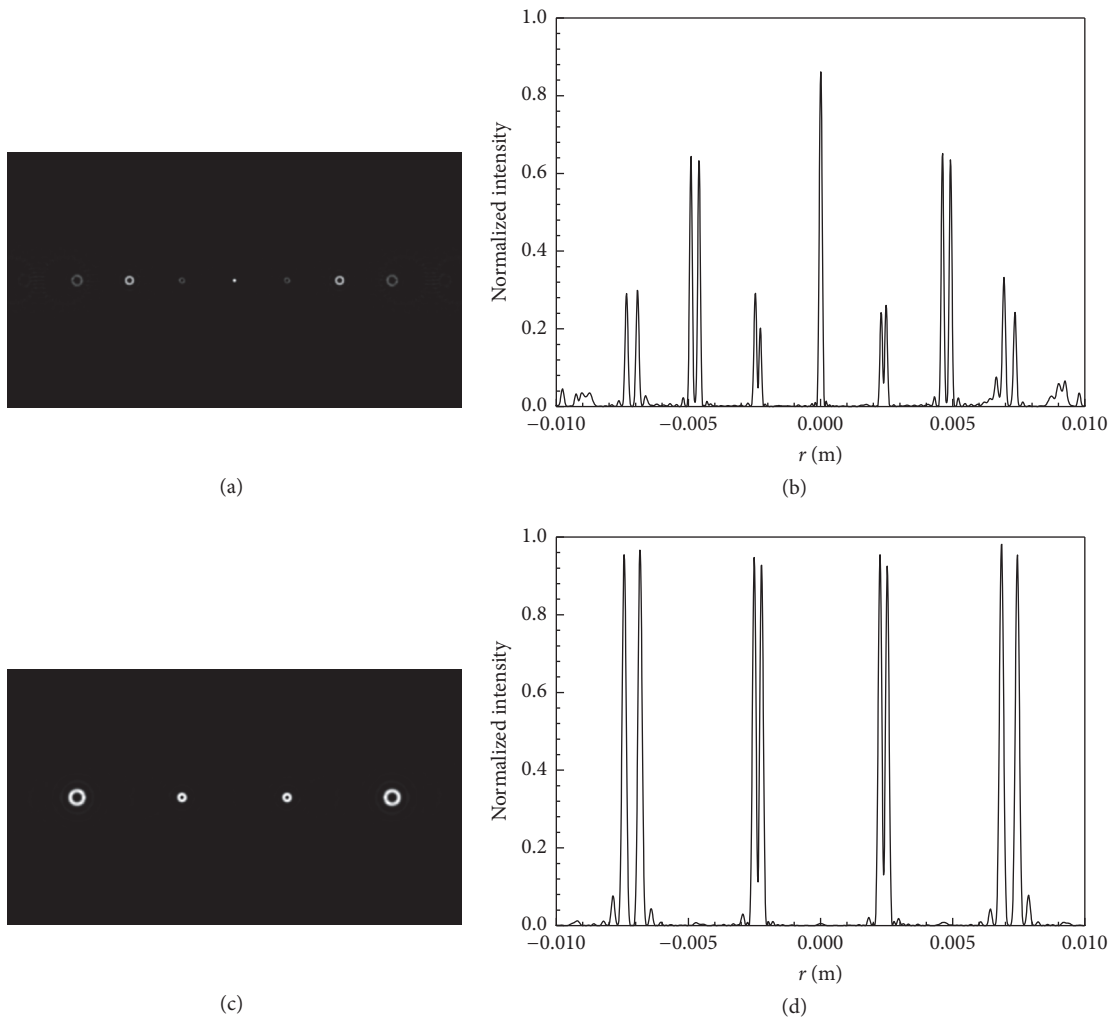


FIGURE 2: The emergent light intensity distribution and normalized spectrum diagram. (a) The light intensity distribution of the original DVG. (b) The corresponding normalized spectrum diagram. (c) The light intensity distribution of the EDVG. (d) The corresponding normalized spectrum diagram.

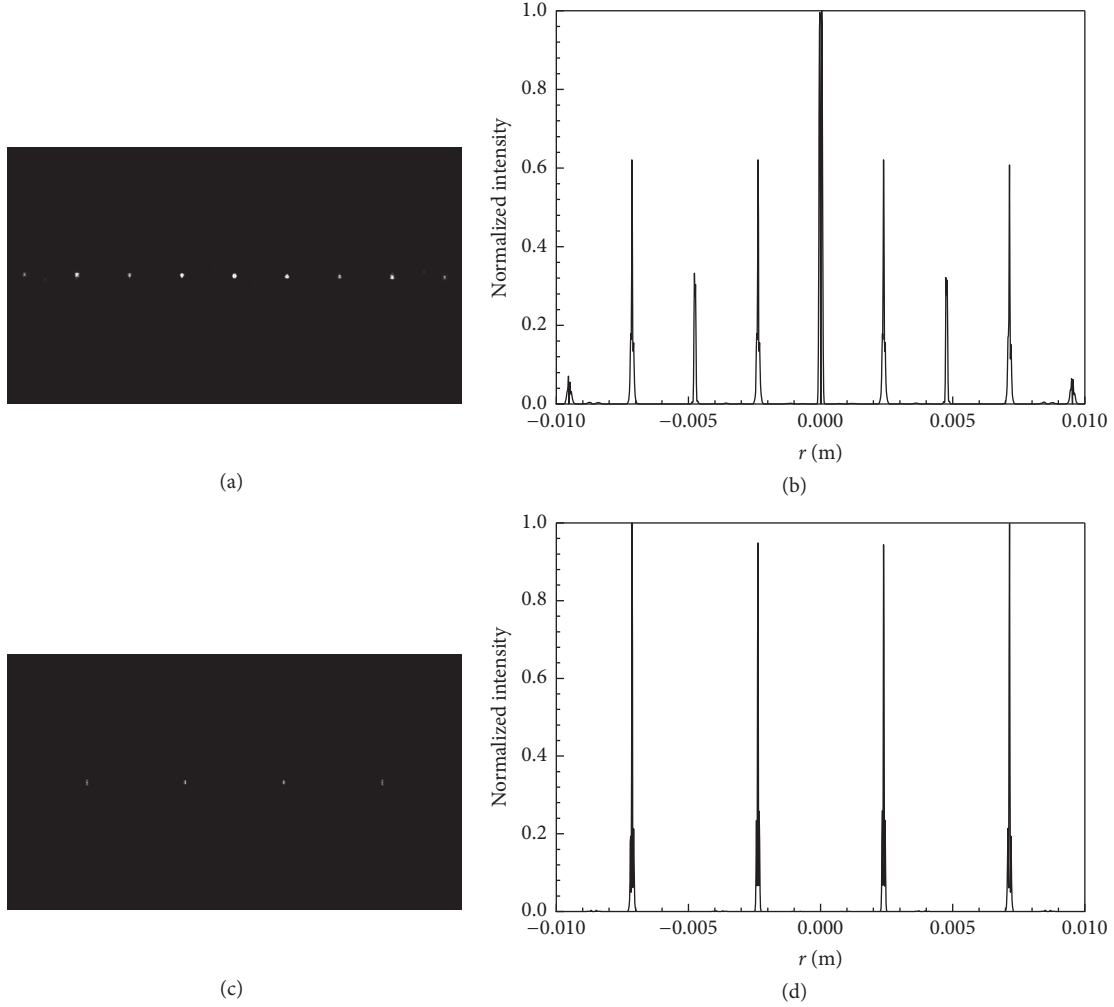


FIGURE 3: The detected light intensity distribution and normalized spectrum diagram. (a) The detected light intensity distribution of the original DVG. (b) The corresponding normalized spectrum diagram. (c) The detected light intensity distribution of the EDVG. (d) The corresponding normalized spectrum diagram.

verified that the average distribution of light intensity is achieved, which shows in Figure 2(d).

To measure the detection ability of EDVG, the LG beams with certain states will be coupled together. After propagating through the EDVG, it will be separated and recovered backed to Gauss beams. The simulation results are showed in Figure 3. The light field distribution of LG beams can be represented as

$$\begin{aligned}
 E_{\text{LG}}(r, \theta, z) = & \sqrt{\frac{2p!}{\pi(p+|l|)!}} \frac{1}{w(z)} \left[\frac{\sqrt{2}r}{w(z)} \right]^{|l|} \\
 & \cdot \exp\left[\frac{-r^2}{w^2(z)}\right] L_p^{|l|} \left[\frac{2r^2}{w^2(z)} \right] \\
 & \cdot \exp\left[\frac{ikr^2z}{2(z^2+z_R^2)}\right]
 \end{aligned}$$

$$\begin{aligned}
 & \cdot \exp\left[-i(2p+|l|+1)\tan^{-1}\left(\frac{z}{z_R}\right)\right] \\
 & \cdot \exp(i\theta),
 \end{aligned} \tag{6}$$

where w_0 is the waist radius of Gauss beam with the propagating distance of $Z = 0$ m, $w(z)$ is the waist radius with propagation distance of $Z > 0$ m, $z_R = \pi w_0^2/\lambda$ is Rayleigh distance, $k = 2\pi/\lambda$ is wave vector, l is azimuth pattern (also called optical vortex topological charges), and p is radial mode number.

If the radial mode number is $p = 0$, the optical field distribution can be represented as

$$E(r, \theta, z) = \sqrt{\frac{2}{\pi|l|!}} \frac{(\sqrt{2})^{|l|}}{w(z)} \left[\frac{r}{w(z)} \right]^{|l|} \exp\left[\frac{-r^2}{w^2(z)}\right]$$

$$\begin{aligned} & \cdot \exp \left[\frac{ikr^2z}{2(z^2 + z_R^2)} \right] \\ & \cdot \exp \left[-i(|l| + 1) \tan^{-1} \left(\frac{z}{z_R} \right) \right] \exp(i\theta). \end{aligned} \quad (7)$$

As showed in Figures 3(a) and 3(c), as the multiplexed OAM beams propagate through the two DVG, they can be separated with different states in free space and recovered back to Gauss-like beam realizing OAM demultiplex. However, compared with Figures 3(b) and 3(d), for the DVG, the zero order of diffraction has a great intensity distribution after demultiplexing, and the light intensity of ± 2 order of diffraction is less than other orders of diffractions, which will cause BER imbalance of different OAM channels. But, for the EDVG, the intensity distribution of each diffraction orders is almost equal, which is beneficial to improve the error performance of OAM optical communication, making the BER equalized among the OAM channels.

Figure 4 is the normalized diffraction spectrum of DVG and EDVG. As shown in Figure 4, the EDVG shows the benefit of realizing the multiplication of diffraction angle and achieving greater space separation. The period of grating is 1.05142, corresponding to the minimum resolution of 0.10051. Given the common resolution of SLM is 1920×1080 , we designed the cycle number with 160. When the size reduced proportionately until being consistent with the common SLM (15.36×8.64 mm), the cycle size is 0.096 mm. As the light beam, with the wavelength of $\lambda = 1550$ nm, passes through the DVG the angle between the adjacent two diffractions is $\beta = \arcsin(\lambda/T) = \arcsin(1.550/96) = 0.9251^\circ$ but 1.8502° for the EDVG.

3. The Atmospheric Turbulence for Vortex Beam Propagation

A major factor for inducing the distortion of vortex beam is atmospheric turbulence. The presence of atmospheric molecules, aerosols, and water mist particle will cause variety of atmospheric attenuation effects, including absorption and scattering [21, 22]. And the nonuniform temperature and air pressure in the atmosphere will cause refractive index change in the transmission path, resulting in the distortion of wavefront phase. The distortion on phase wavefront is extremely harmful for OAM communication, because the OAM demultiplexing is based on the spiral phase distribution [23]. Some previous works have suggested that the refractive index inhomogeneity will result in channel crosstalk among different OAM channels.

Theory and experiment confirmed that the random phase screen can be used to establish the model of atmospheric turbulence for simulation [24]. The modified Hill spectral model is used and can effectively avoid the insufficiency of sampling frequency. Its expression can be written as [25–27]

$$\Phi_n(k_x, k_y) = 0.033C_n^2 \left(1 + 1.802 \sqrt{\frac{k_x^2 + k_y^2}{k_l^2}} \right)$$

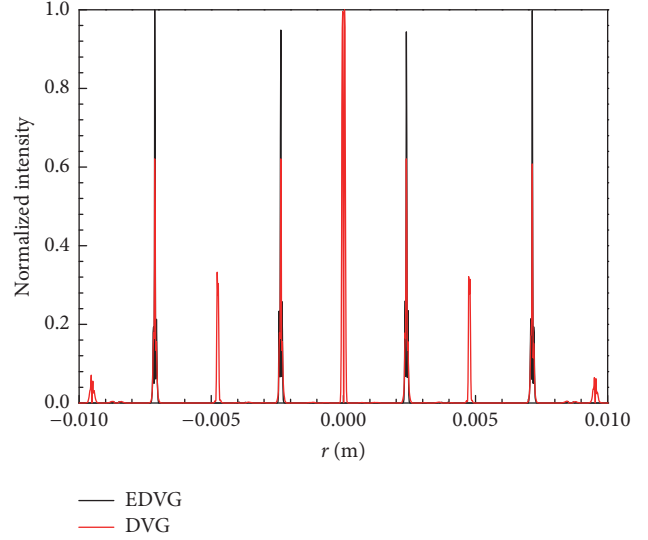


FIGURE 4: The normalized diffraction spectrum of DVG and EDVG.

$$\begin{aligned} & -0.254 \left(\frac{k_x^2 + k_y^2}{k_l^2} \right)^{-7/12} \exp \left[\frac{k_x^2 + k_y^2}{k_l^2} \right] \\ & \cdot \left(k_x^2 + k_y^2 + \frac{1}{L_0^2} \right)^{-11/6}, \end{aligned} \quad (8)$$

where C_n^2 is the atmospheric refraction constant, L_0 is the turbulent outer scale, l_0 is the turbulent interscale, $k_l = 3.3/l_0$, and k_x, k_y are the coordinates of power spectrum phase screen, respectively. The relationship between refractive index spectrum and phase spectrum can be present as (Z is the transmission distance)

$$\Phi(k_x, k_y) = 2\pi k_0^2 \Delta Z \Phi_n(k_x, k_y). \quad (9)$$

The random phase screen spectrum variance can be expressed as

$$\sigma^2(k_x, k_y) = \frac{2\pi}{N\Delta x} \Phi(k_x, k_y). \quad (10)$$

Then Fourier transform for the random phase screen spectrum variance can get the random phase screen:

$$\varphi(x, y) = \text{FFT}(\sigma(k_x, k_y)). \quad (11)$$

And if the input field is E_0 , the output optical field distribution can be expressed as

$$\begin{aligned} E(x, y) & \\ & = \text{FFT}^{-1} \left[\text{FFT} [E_0 \cdot \exp(i\varphi(x, y))] \cdot E_{\text{prop}}(k_x, k_y) \right]. \end{aligned} \quad (12)$$

Among them, $\text{FFT}[\cdot]$ and $\text{FFT}^{-1}[\cdot]$ are referred to Fourier transform and inverse Fourier transform, and $E_{\text{prop}}(k_x, k_y)$ is the transfer function of the Fresnel diffraction. In the next section, it will be used to simulate the transmission of optical vortex in atmospheric turbulence. In simulation, the atmospheric refractive index constant of $C_n^2 = 10^{-14}$ is used.

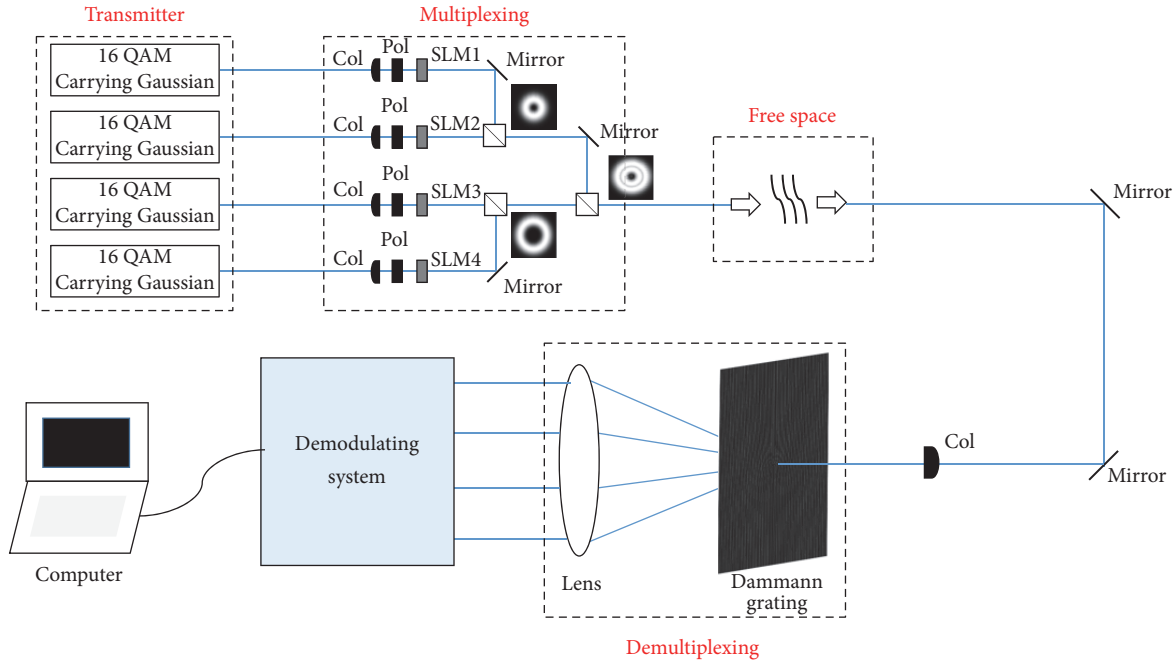


FIGURE 5: The OAM optical communication system.

4. The OAM Optical Communication System Design and Simulation

As shown in Figure 5, the OAM optical communication systems based on EDVG demultiplexer are designed. The communication system mainly consists of four parts, including the transmitter, multiplexer, free space transport channel, and the demultiplexer. In the sending side, the IQ modulator is used to load 16-QAM signals to Gaussian light. Then, four signal light beams are converted into optical vortex by liquid crystal spatial light modulator (SLM). Finally, it coupled into a bunch of coaxial vortex transmitted lights by three beam splitters. After a distance transmission in free space, the EDVG can be used to demultiplex and demodulate the signals at the receiving side.

4.1. The Equalizing of Diffraction Efficiency. The optical vortices with corresponding topological charges are generated by SLM. After being transmitted over free space, it is demultiplexed by using EDVG, and the results of calculated diffraction efficiency of diffracted orders are showed in Figure 6. By using the EDVG, after the coaxial propagation of 1 m in the free space the diffraction efficiencies are 19.45% and 21.55% with the topological charges of ± 3 and ± 1 and the total diffraction efficiency is 82%. However, when using the DVG, the diffraction efficiencies ± 3 , ± 2 , and ± 1 are 12.06%, 5.06%, and 12.06%, and the total diffraction efficiency is 53.22%. By comparison, these two Damann vortex gratings can be used to realize optical vortices demultiplex, and the total diffraction efficiency of DVG is lower than the EDVG due to a significant portion of light energy focused on the zero-order diffraction level. This energy is useless or even harmful to OAM communication, because it cannot

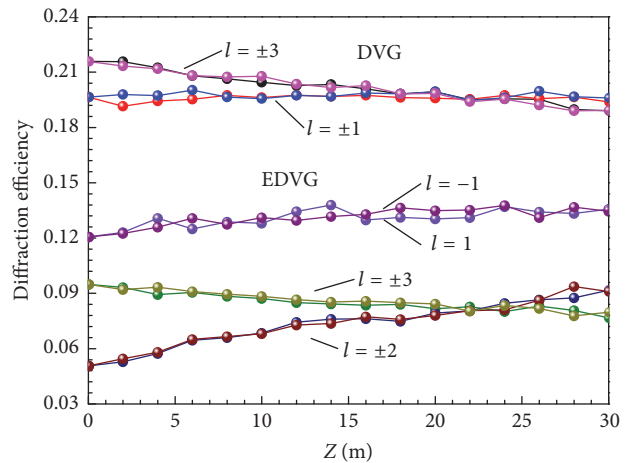


FIGURE 6: The diffraction efficiency of every diffraction order.

implement effective demultiplexing and take up the light energy of other orders of diffraction, which caused the loss of light energy. From Figure 6, it can be seen obviously that the balance of diffraction efficiency is achieved. The EDVG can realize the uniform distribution of light intensity, and the diffraction efficiency had significant doubled increase for the topological charges of ± 3 and ± 1 . In general, the EDVG can be used to improve diffraction efficiency and make the diffracted light intensity distribution even to each order of diffraction.

4.2. The BER Performance of OAM Optical Communication by Using Damann Vortex Gratings as Demultiplexer. In this section, the BER performance of OAM optical communication system by using two Damann vortex gratings as

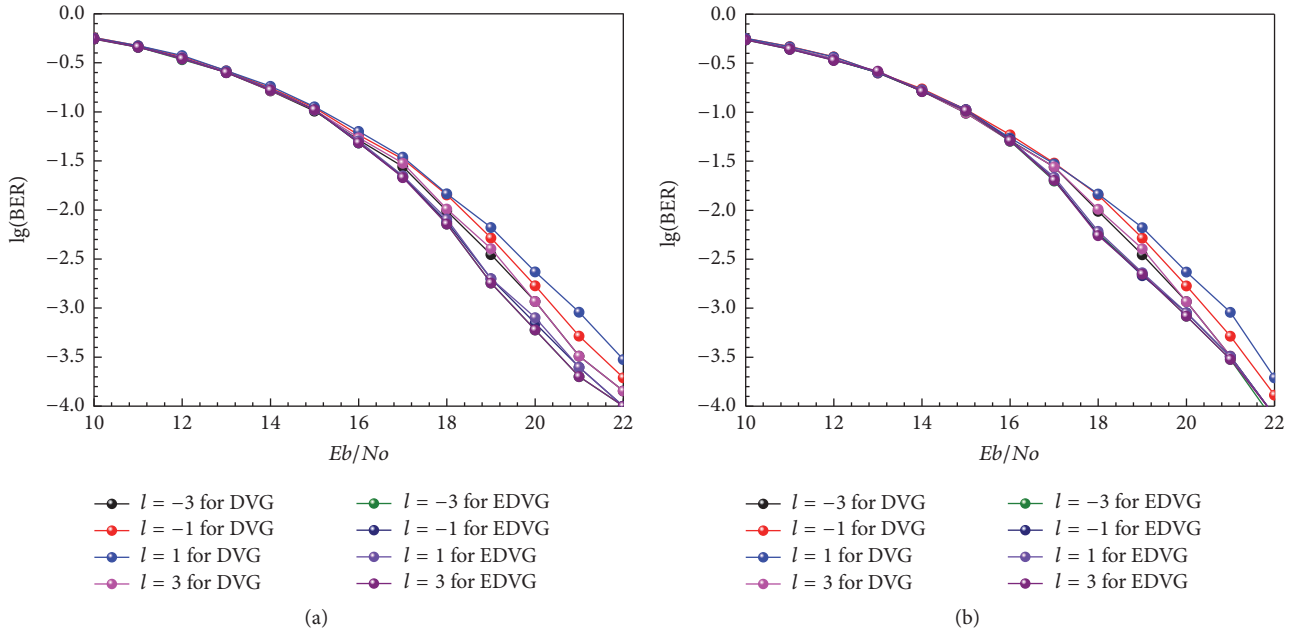


FIGURE 7: The error curves graph of the OAM optical communication system. (a) The error curves by using DVG and EDVG for demultiplexing, respectively. (b) The error curves by using DVG and EDVG for demultiplexing in the absence of channel crosstalk.

demultiplexer will be discussed. As shown in Figure 5, 16-QAM signals can be modulated to 4 Gaussian lights by using IQ modulator in the sending side. Then, the light sources carried signals are converted into optical vortex through SLM and coupled by 3 beam splitters. After transmitting 1 m in free space, the two Dammann vortex gratings are used to demultiplex and demodulate OAM signals at the receiving side. Figure 7 is the error curves graph of the OAM optical communication system. Figure 7(a) is corresponding to the error curves by using DVG and EDVG demultiplexer. As shown in Figure 7(a), with the increase of SNR, the BER of channels are decreased, and the BER of 4 OAM channels are unequal. The BER in the channels with topological charges of ± 1 are higher than the other two channels. When the SNR is 22 dB, the BER for topological charges $l = +1, -1, +3$, and -3 are 2.3×10^{-4} , 2×10^{-4} , 1.5×10^{-4} , and 1.5×10^{-4} , respectively. However, by using the EDVG to demultiplex, it can be seen from the graph that, with the increase of the SNR, the BER of all channels are gradually reduced almost equally. When the SNR is 22 dB, the error rates for the channels of topological charges $l = +1, -1, +3$, and -3 are 1.1×10^{-4} , 1.1×10^{-4} , 1.0×10^{-4} , and 1.0×10^{-4} , respectively. At the same time, it also can be found that the BER differences among different channels are growing with the SNR increase. This is because the low SNR and the intersymbol noise will play a major role. With the enhancing of SNR, intersymbol noise decreased, and the channel noise became the main factor which leads to BER difference among different OAM increases. There are two factors that lead to channel noise: one is the channel crosstalk between different OAM states due to the effect of atmospheric turbulence in the process of beam transmission; the other one is that the light intensity distribution of different diffraction order is uneven when

DVG is used for demultiplexing. The detected intensity is weak which will cause error rate rise. In simulation, the same OAM beams are used, and the OAM channel crosstalk of two kinds of demultiplex way is consistent. Therefore, the distribution difference of BER using the EDVG can achieve diffracted light intensity equilibrium distribution.

To further study the effect of channel crosstalk, only one OAM light beam carried signals, the BER changes of each OAM with SNR increasing in the absence of channel crosstalk are measured, and the results are showed in Figure 7(b). From Figure 7(b), when the SNR is 22 dB, the BER of OAM channels are 8×10^{-5} , 8×10^{-5} , 8×10^{-5} , and 7×10^{-5} , respectively, by using the improved demultiplex. However, the BER increased to 2×10^{-4} , 1.3×10^{-4} , 8×10^{-5} , and 8×10^{-5} , if the original grating is used with similar SNR. Compared with Figures 7(a) and 7(b), it is easy to find that the BER within each OAM channel is lower in the same SNR when not considering the channel crosstalk, but the error rate change is very small. Therefore, the main reason causing that the BER is uneven within each OAM channel is the unevenness of light intensity after using DVG demultiplexer.

5. Conclusion

Optical vortex is a kind of structured light beam which can carry OAM. In theory, every single wavelength light can carry infinite vortex state, and they are orthogonal to each other. By using OAM as a new multiplexing dimension, it can greatly improve the capacity density of communication. However, the efficient multiplexing method, with channel equalization, is one of the most important issues that need to be resolved. Dammann vortex grating is a kind of component to achieve efficient separation of vortex state and realize the

light intensity distribution uniformly. However, we found that the common Damman vortex grating can be used to demultiplex the multiplexed OAM beams and the light intensity after demultiplexing can focus on the necessary order of diffraction. But its zero order has a large amount of light intensity and the diffracted light intensity is unevenly distributed, which will result in the BER imbalance between OAM channels. Here, we improved the Damman vortex gratings by inhibiting the even and zero order of diffraction and realized the uniform regulation of the diffracted light intensity. The research results show that this improved Damman vortex grating can make the diffraction angle of grating multiplied and achieve greater separation of the diffracted order. The diffraction angle of grating is 1.8502° , and the total diffraction efficiency is 82%. The distribution balance of light intensity is also achieved by reducing the number of diffraction orders. Employing this Damman vortex grating as demultiplexer for OAM communication system, the BER within each order of diffraction are relatively uniform, and the channel BER equilibrium distribution is efficiently realized. When SNR is 22 dB, the BER of topological charge $l = +1, -1, +3$, and -3 are 1.1×10^{-4} , 1.1×10^{-4} , 1.0×10^{-4} , 1.0×10^{-4} respectively. Our results indicate that the improved vortex grating has exhibited the wide prospective in OAM multiplexing and channel equalization for optical communication.

Conflicts of Interest

The authors declare that they have no conflicts of interest.

Authors' Contributions

Mingyang Su and Junmin Liu contributed equally to this paper.

Acknowledgments

This work is partially supported by the program of Fundamental Research of Shenzhen Science and Technology Plan (Grant nos. JCYJ20150324141711651, JCYJ20160422152152634, and JCYJ2016032814464), the National Science Foundation of China (Grant nos. 61575127, 61505122), the Project Supported by Guangdong Natural Science Foundation (Grant nos. 2016A030310065, 2014A030310279), the Natural Science Foundation of SZU (Grant nos. 000059 and 2016031), Science and Technology Planning Project of Guangdong Province (2016B050501005), and the Natural Science Foundation Guangdong Education Department (Grant nos. 2015KTSCX124 and 2015KQNCX146).

References

- [1] L. Allen, M. W. Beijersbergen, R. J. C. Spreeuw, and J. P. Woerdman, "Orbital angular momentum of light and the transformation of Laguerre-Gaussian laser modes," *Physical Review A*, vol. 45, no. 11, pp. 8185–8189, 1992.
- [2] A. Beržanskis, A. Matijošius, A. Piskarskas, V. Smilgevičius, and A. Stabinis, "Conversion of topological charge of optical vortices in a parametric frequency converter," *Optics Communications*, vol. 140, no. 4–6, pp. 273–276, 1997.
- [3] J. Leach, M. J. Padgett, S. M. Barnett, S. Franke-Arnold, and J. Courtial, "Measuring the Orbital Angular Momentum of a Single Photon," *Physical Review Letters*, vol. 88, no. 25, 2002.
- [4] F. Wen, Z. Li, Y. Zhang et al., "Triple-mode squeezing with dressed six-wave mixing," *Scientific Reports*, vol. 6, Article ID 25554, 2016.
- [5] F. Wen, I. Ali, A. Hasan et al., "Ultrafast optical transistor and router of multi-order fluorescence and spontaneous parametric four-wave mixing in Pr³⁺:YSO," *Optics Letters*, vol. 40, no. 20, pp. 4599–4602, 2015.
- [6] G. Gibson, J. Courtial, M. J. Padgett et al., "Free-space information transfer using light beams carrying orbital angular momentum," *Optics Express*, vol. 12, no. 22, pp. 5448–5456, 2004.
- [7] A. E. Willner, J. Wang, and H. Huang, "Applied physics. A different angle on light communications," *Science*, vol. 337, no. 6095, pp. 655–656, 2012.
- [8] M. Malik, M. O'Sullivan, B. Rodenburg et al., "Influence of atmospheric turbulence on optical communications using orbital angular momentum for encoding," *Optics Express*, vol. 20, no. 12, pp. 13195–13200, 2012.
- [9] D. Zhang, X. Feng, and Y. Huang, "Encoding and decoding of orbital angular momentum for wireless optical interconnects on chip," *Optics Express*, vol. 20, no. 24, pp. 26986–26995, 2012.
- [10] J. H. Shapiro, S. Guha, and B. I. Erkmen, "Ultimate channel capacity of free-space optical communications," *Journal of Optical Networking*, vol. 4, no. 8, pp. 501–516, 2005.
- [11] Y. Awaji, N. Wada, and Y. Toda, "Demonstration of spatial mode division multiplexing using Laguerre-Gaussian mode beam in telecom-wavelength," in *Proceedings of the 23rd Annual Meeting of the IEEE Photonics Society, PHOTONICS 2010*, pp. 551–552, November 2010.
- [12] J. Wang, J.-Y. Yang, I. M. Fazal et al., "Terabit free-space data transmission employing orbital angular momentum multiplexing," *Nature Photonics*, vol. 6, no. 7, pp. 488–496, 2012.
- [13] H. Huang, G. Xie, Y. Yan et al., "100 Tbit/s free-space data link enabled by three-dimensional multiplexing of orbital angular momentum, polarization, and wavelength," *Optics Letters*, vol. 39, no. 2, pp. 197–200, 2014.
- [14] G. C. G. Berkhout, M. P. J. Lavery, J. Courtial, M. W. Beijersbergen, and M. J. Padgett, "Efficient sorting of orbital angular momentum states of light," *Physical Review Letters*, vol. 105, no. 15, Article ID 153601, 4 pages, 2010.
- [15] V. V. Kotlyar, S. N. Khonina, and V. A. Soifer, "Light field decomposition in angular harmonics by means of diffractive optics," *Journal of Modern Optics*, vol. 45, no. 7, pp. 1495–1506, 1998.
- [16] S. N. Khonina, V. V. Kotlyar, V. A. Soifer, P. Pääkkönen, J. Simonen, and J. Turunen, "An analysis of the angular momentum of a light field in terms of angular harmonics," *Journal of Modern Optics*, vol. 48, no. 10, pp. 1543–1557, 2001.
- [17] S. N. Khonina, V. V. Kotlyar, V. A. Soifer, P. Paakkonen, and J. Turunen, "Measuring the light field orbital angular momentum using DOE," *Optical Memory and Neural Networks*, vol. 10, pp. 241–255, 2001.
- [18] N. Zhang, J. A. Davis, I. Moreno, D. M. Cottrell, and X.-C. Yuan, "Analysis of multilevel spiral phase plates using a Damman vortex sensing grating," *Optics Express*, vol. 18, no. 25, pp. 25987–25992, 2010.

- [19] C. Zhou and L. Liu, "Numerical study of Dammann array illuminators," *Applied Optics*, vol. 34, no. 26, pp. 5961–5969, 1995.
- [20] J. Yu, C. Zhou, W. Jia et al., "Three-dimensional Dammann vortex array with tunable topological charge," *Applied Optics*, vol. 51, no. 13, pp. 2485–2490, 2012.
- [21] J. W. Strohbehn, "Laser beams propagation in the atmosphere," *Springer-Verlag*, vol. 27, no. 2, p. 259, 1978.
- [22] L. C. Andrews and R. L. Phillips, "Laser beam propagation through random media," *SPIE Press*, 1998.
- [23] J. A. Anguita, M. A. Neifeld, and B. V. Vasic, "Turbulence-induced channel crosstalk in an orbital angular momentum-multiplexed free-space optical link," *Applied Optics*, vol. 47, no. 13, pp. 2414–2429, 2008.
- [24] P. Polynkin, A. Peleg, L. Klein, T. Rhoadarmer, and J. Moloney, "Optimized multiemitter beams for free-space optical communications through turbulent atmosphere," *Optics Letters*, vol. 32, no. 8, pp. 885–887, 2007.
- [25] J. W. Strohbehn, "Modern theories in the propagation of optical waves in a turbulent medium," *Topics in Applied Physics*, vol. 25, pp. 45–106, 1978.
- [26] R. Frehlich, "Simulation of laser propagation in a turbulent atmosphere," *Applied Optics*, vol. 39, no. 3, pp. 393–397, 2000.
- [27] J. D. Strasburg and W. W. Harper, "Impact of atmospheric turbulence on beam propagation," in *Laser Systems Technology II*, Proceedings of SPIE, pp. 93–102, Orlando, Fla, USA, April 2004.